Green synthesis of iron silicide nanoparticles for photothermal cancer therapy

By **Xutao Guo**

A thesis submitted to

The University of Birmingham

for the degree of

DOCTOR OF PHILOSOPHY

Nanoscale Physics Research Laboratory

School of Physics and Astronomy

University of Birmingham

Birmingham B15 2TT, UK.

Declaration

I hereby declare that the thesis is my original work and it has been written by me in its entirety. I have duly acknowledged all the sources of information which have been used in the thesis.

This thesis has also not been submitted for any degree in any university previously.

[redacted]

Xutao Guo

February, 2023

Acknowledgements

As a student of the Joint PhD Training Program offered by the University of Birmingham (UoB) and Southern University of Science and Technology (SUSTech), I would like to express my heartfelt gratitude to my supervisors, Leigh Canham, Wolfgang Theis in UoB and Zhenghe Xu, Zhouguang Lu in SUSTech, for their supervision as well as to UoB and SUSTech for their support for my studies in both universities.

I would like to thank my PhD supervisor in SUSTech, Dr. Zhenghe Xu, for giving me such a good opportunity to work on the project at the beginning and always being patient and enthusiastic with this project. He is always energetic and active in thinking for the project. As a Dean of college of Engineering, he has a wide view of the project and gives me many resources so that I can complete and improve my project, discuss and cooperate with researchers of different background. He gives me much support and guidance. I learn a lot from him. My second supervisor Dr. Zhouguang Lu gives me much help in my university life and flexible guidance in my research.

I appreciate all the group members (Dr. Wenbin Zhang, Dr. Xin Wang, Dr. Fan Yang, Dr. Feng Jiang, Dr. Shubin Wang, Dr. Chao Peng, Dr. Hao Wang, Dr. Shijiao Zhao, Dr. Xinyang Wang, Dr. Wen Tan, Jiming Lu, Qiurong Long, Kun Li, Tingting Yi, Huimin Yuan, Lingfei Liu, Peiyuan Ye, Junjie Zhang, Yi Liu, Binda Lu, Wanran Lin, Wang Lu, Xueyan Kang, Boyan Chen, Yuhan Liu) and other friends in SUSTech for making my PhD experience great. They spend much time with me, including the periods when we worked, studied, had recreation, and food. Thanks to them all for helping me and providing a good office and lab atmosphere.

I would like to thank my PhD supervisor in UoB, Dr. Leigh T. Canham, for his scientific guidance, frequent meetings and many encouragements. The successful completion of this thesis is supported by his continuous suggestions and encouragement. He gives me much confidence about the project and life. My second supervisor Wolfgang Theis helps me a lot for the group contact and my monthly report. Catherine J. Storey, senior laboratory technician, helped me a lot with using the equipment in the Silicon Lab. I would like to thank Dr. Ziyou Li, she helped me a lot for my entrance to UoB and cared much about me when I studied in UoB. She passed away sadly when I was on my second-year study. May she rest in peace.

I appreciate my schoolmates in UoB, Yu Xia, Cheng Li, Zheng Du. We discuss the project and have much good time.

I appreciate my cooperative partners from Department of Biomedical Engineering in SUSTech, Dr. Kai Li, Shuxian Wang and Dr. Jun Wang for their animal testing, discussion and help.

Finally, I would like to thank my family members, my grandma, dad, mum, brother and my wife Xiaoxue Zhang, for all their understanding, support, concern and encouragement.

Thanks to all the people who helped me. Without their help, I could not finish the project and thesis.

Abstract

Over the last few decades, the interest in photothermal therapy increased dramatically. A wide variety of photothermal agents have been reported since 2003. Improved photothermal agents with good efficacy, safety and scalable synthesis are required. This thesis focuses on the fabrication, characterization, photothermal performance, photothermal therapy *in vivo* and biodegradability test of a novel photothermal agent.

The thesis is arranged in the manner as follows. The motivation and the background topics (chapter 1) were firstly introduced. Then the synthesis of materials and basic characterization (chapter 2), *in-vitro* photothermal performance (chapters 3), photothermal therapy *in vivo* (chapter 4) and then *in-vitro* biodegradability (chapter 5).

Mesoporous iron silicide nanoparticles (FeSi NPs) were synthesized by a simple green method of magnesiothermic co-reduction. Starting from biogenic mesoporous silica ("tabasheer") extracted from bamboo and Fe_2O_3, the resultant FeSi NPs of a small band gap showed a good optical absorption with a high photothermal conversion efficiency of 76.2%, indicating a good photothermal performance. The weight extinction coefficient of the FeSi NPs was 13.3 L g^{-1} cm^{-1} at 1064 nm (second near-infrared window, NIR-II), which surpassed the performance of other competitive Si-based and Fe-based photothermal agents.

In vivo results on mice showed clearly an efficient suppression of tumour growth by photothermal treatment with the synthesized FeSi NPs. Biodegradability test shows that fabricated FeSi NPs are slowly biodegradable. The results from our thesis indicate that FeSi NPs are a new class of promising photothermal agents (PTAs) for photothermal therapy of cancer.

List of Figures

Figure 1 Schematic representation of pore types. C, B, T and I show closed pore, blind pore, through pore, interconnected pore; R shows roughness. Adapted from (Rouquerol, 1990) 37

Figure 2 Schematic representation of magnetization characteristics of magnetic materials (a) and threshold diameters for superparamagnetism (d_{SP}) and maximum monodomain critical diameters (d_{cr}) for spherical nanoparticles (b). Adapted from (Mohammed 2017; Majetich 2013)... 39

Figure 3 Schematic representation of contact angle. (Adapted from Liber-Kne´c 2021). 41

Figure 4 Optical photo of contact angle meter (a) and schematic representation for Washburn capillary rise (b). In figure b, the enlarged right sketches are the scenarios when the tube touches the liquid using (A) a hydrophilic tube (<90°)-liquid climbs up the outside of the tube wall or (B) a hydrophobic tube (>90°)-liquid is compressed at the tube/liquid/air interface. Adapted from (https://www.biolinchina.com/attension; Alghunaim 2016). 42

Figure 5 Routes to porous silicon via solid silicon and using chemical conversion. Adapted from (Canham 2014)........ 44

Figure 6 Schematic representation of oxygen-potential diagram. Adapted from (Li 2005). 44

Figure 7 Schematic representation of binary phase diagram of Si-Fe (a) and Si-Ni (b). Adapted from (Von Goldbeck 1982; Okamoto 2000). 48

Figure 8 Schematic illustration showing the fabrication of pSi NPs and corresponding optical images of the product in each stage. 54

Figure 9 XRD pattern of tabasheer precursor and fabricated biogenic silicon. 55

Figure 10 SEM images of the tabasheer (a)-(c) and the biogenic silicon (d)-(f). 56

Figure 11 N_2 adsorption-desorption isotherm and the corresponding pore size distribution curve of the tabasheer precursor (a) and biogenic silicon (b). 57

Figure 12 XRD pattern of fabricated iron (Fe) and commercial iron (Fe) nanoparticles. 58

Figure 13 SEM images of the fabricated Fe NPs. 58

Figure 14 Magnetization curves of fabricated iron (F-Fe) nanoparticles. 59

Figure 15 Schematic illustration showing the fabrication of porous FeSi nanoparticles (FeSi NPs) for photothermal therapy and photos of corresponding products collected in each stage. 60

Figure 16 XRD patterns of the biogenic feedstock and fabricated materials. 61

Figure 17 SEM image of F-FeSi NPs (a); HRTEM images of F-FeSi NPs (b). 62

Figure 18 EDX spectrum of the F-FeSi samples, with inset table presenting elemental ratios (atom percentages) calculated using EDX software. 63

Figure 19 Particle diameter distribution of F-FeSi measured with the DLS with the NPs being dispersed in deionized H_2O prior to the measurement. 64

Figure 20 N_2 adsorption-desorption isotherm of the fabricated FeSi NPs. 65

Figure 21 Magnetization curves of fabricated FeSi nanoparticles. 65

Figure 22 Schematic illustration showing the fabrication of Fe/Si-based nanoparticles. 66

Figure 23 XRD spectrums of the materials fabricated by HCl washing and NH_4Cl washing. A-D refer to varying feedstock compositions, as described in the text. 67

Figure 24 Magnetization curves of fabricated materials. A-D refer to varying feedstock compositions, as described in the text. 69

Figure 25 Corresponding saturation magnetizations of fabricated NPs from different precursors at room temperature under 2.5T. A-D refer to varying feedstock compositions, as described in the text........................69

Figure 26 Contact angle measurement of F-FeSi tablet created via cold pressing. 70

Figure 27 Schematic diagram of light passing through the substance. I_0 is the incident optical intensity, I_r is the reflected optical intensity and I is the transmitted optical intensity. 73

Figure 28 Schematic description of electronic cloud displacements in nanoparticles under effect of an electromagnetic wave. (Moores 2006). 75

Figure 29 Schematic diagram of photothermal conversion mechanism for semiconductors. 76

Figure 30 Experimental and theoretical values of melting-point temperature of Au (a) and Si (b). Adapted from (Buffat 1976; Talyzin 2019)...............77

Figure 31 Data of thermal conductivity, heat capacity of materials. Adapted from (Canham 2014). 80

Figure 32 Schematic diagram of setup for characterizing photothermal performance of solutions containing materials. Adapted from (Regli 2012; Chen 2010). 81

Figure 33 Optical image of setup used for photothermal performance of materials (a) and photothermal therapy of mouse (b) in Department of Biomedical Engineering, Southern University of Science and Technology (SUSTech). 81

Figure 34 Dependence of output power of 1064nm laser with applied current. 83

Figure 35 Schematic diagram of broad and narrow photothermal conversion efficiency. 85

Figure 36 UV-vis-NIR absorbance spectra of F-FeSi NPs aqueous suspensions of different particle concentrations, with the inset showing a linear relationship between the absorbance of FeSi NP suspensions at 1064 nm and particle concentration. 89

Figure 37 Narrow FTIR spectrum from 2.5 μm to 17.5 μm and the corresponding absorption threshold of fabricated FeSi NPs. 91

Figure 38 Temperature variation of aqueous suspensions (200 uL) containing different materials at the same concentration of 0.5 mg/mL under irradiation of a 1064 nm laser at 1 W cm^{-2} for 10 min. 93

Figure 39 Photothermal performance of the Fe/Si-based nanocomposites after HCl and NH_4Cl washing. A-D refer to varying feedstock compositions, as described in the text of chapter 2 and properties illustrated in figures 23-25. 94

Figure 40 a) Temperature change of FeSi NPs aqueous suspension with particle concentration under 1064 nm laser irradiation at 1 W cm^{-2} for 10 min, with the inset showing a linear relationship between plateau temperature and particle concentration; b) Temperature change of 0.5 mg/mL FeSi NPs aqueous suspension under irradiation of 1064 nm laser at different power densities for 10 min, the inset showing a linear relationship between plateau temperature and laser power density. All the measurement used 200 uL of FeSi NPs aqueous suspensions. 96

Figure 41 (a) Temperature profile of 0.5 mg/mL FeSi NPs aqueous suspension (200 uL) irradiated by a 1064 nm laser at 1 W cm^{-2}, followed by natural cooling with the laser off, and (b) the time constant for heat transfer calculated using a linear regression of the cooling profile. 97

Figure 42 Temperature variation of 0.1 mg/mL FeSi NPs aqueous suspensions (200 uL) over 5 cycles of heating at 1 W cm^{-2} and natural cooling........ 99

Figure 43 Basis of the photothermal therapy. Adapted from (Estelrich 2018). 102

Figure 44 Optical windows in biological tissues. Adapted from (Smith 2009). 104

Figure 45 Schematic diagram of (a) intravenous injection and (b) intratumoral injection of materials. Adapted from (Lin 2017).......................................106

Figure 46 Elements are in red and black boxes on the periodic table that contribute to photothermal agents. Adapted from (https://zh.wikibooks.org/wiki/%E5%85%83%E7%B4%A0%E5%91%A8%E6%9C%9F%E8%A1%A8)..107

Figure 47 Common PTAs reported during the past 20 years.........................108

Figure 48 Sizes of the Au NPs in PTT affect their biological behaviours. Adapted from (Ali 2019)...110

Figure 49 Summary of current research developments for biomedical applications. Adapted from (Lin 2018)..117

Figure 50 3-month and 12-month follow-up biopsy results from the targeted ablation zone. Adapted from (Rastinehad 2019).....................................118

Figure 51 a) Photothermal images of mice i.t. injected with FeSi NPs and PBS under a 1064 nm laser irradiation at 1 W cm^{-2} for 15 min; b) Temperature change curves of 4T1 tumors upon laser irradiation...............................121

Figure 52 a) Variation of mice tumor after being i.t. injected with PBS and FeSi NPs with and without laser irradiation after 0, 7 and 14 days; b) Representative photographs of tumors obtained from mice at day 14 after different treatments..122

Figure 53 a) Growth curves of mice tumour size under different treatments; b) Variation of the mouse weights with time after different treatments. 123

Figure 54 a) H&E staining of tumor slices in mice of each group after treatment; b) Histological sections of major organs. P values: ***p < 0.001........124

Figure 55 Illustration of degradation mechanisms of Fe–Mn alloys: (a) Initial degradation reaction; (b) Formation of hydroxide layer. Adapted from (Zhen 2013).........130

Figure 56 Degradation of bulk tabasheer in SBF solution after different days. 137

Figure 57 Degradation of F-FeSi with three concentrations in SBF solution after different days........138

Figure 58 Degradation of F-FeSi and C-FeSi NPs in SBF solution after different days........139

Figure 59 N_2 adsorption-desorption isotherm of F-FeSi and C-FeSi particles. 140

List of Tables

Table 1 Comparisons of ferromagnetism, paramagnetism and superparamagnetism. 39

Table 2 Relationship between contact angle and wettability. 41

Table 3 Comparisons of the techniques used for different characterisations. 54

Table 4 Detailed introduction of the techniques used for different characterisations. 88

Table 5 Comparisons of PTAs for photothermal therapy. 114

Table 6 Experimental details of some photothermal agents with high photothermal conversion efficiency. 116

Table 7 Biodegradable materials of different classes and their medical uses. 128

Table 8 Comparisons of concentrations of ions in three simulated body fluids used for testing purposes. 133

Table 9 Information on the techniques used for characterisation 133

Table 10 Weight change of bulk tabasheer after increasing days of incubation in SBF. 137

Table 11 BET results of F-FeSi and C-FeSi particles……………………………………140

List of Abbreviations

A Absorbance

AAS atomic absorption spectrometer

BBB blood brain barrier

BET Brunauer–Emmett–Teller

CT computed tomography

CVD chemical vapor deposition

DLS dynamic light scattering

DMEM dulbecco's modified eagle medium

DSC Differential scanning calorimetry

EDS Energy-Dispersive X-Ray Spectroscopy

EPR enhanced permeability and retention

FTIR Fourier transform infrared spectroscopy

HCA $Ca_5(PO_4)_{3-x}(CO_3)_xOH$

H&E hematoxylin and eosin

ICP-MS Inductively Coupled Plasma Mass Spectrometry

IR infrared

LSP local surface plasmon

LSPR Local surface plasmon resonance

MHT magnetic hyperthermia therapy

MPMS Magnetic Property Measurement System

MRI magnetic resonance imaging

NIR near infrared

NPs nanoparticles

NZVI Nanoscale zero-valent iron particles

PA photoacoustic

PBS phosphate buffered saline

PDT photodynamic therapy

PEI percutaneous ethanol injection

PPMS physical property measurement system

pSi porous silicon

PTAs photothermal agents

PTT photothermal therapy

SBF simulated body fluid

SDs standard deviations

SDT sonodynamic therapy

SEM Scanning Electron Microscopy

SP Surface plasmon

SQUID Superconducting quantum interference device

TEM Transmission Electron Microscope

UV ultraviolet

Vis visible

VSM vibrating sample magnetometer

XRD X-ray Powder Diffraction

2D two-dimensional

Table of Contents

Declaration 4

Acknowledgements 5

Abstract 8

List of Figures 10

List of Tables 18

List of Abbreviations 20

Chapter 1. Introduction and Background 29

1.1 Background to scope of thesis 29

1.2 Aims and objectives 32

1.3 Layout of the thesis 34

1.4 List of publications 35

Chapter 2. Green synthesis of porous Si, porous zero valent Fe and porous FeSi by magnesiothermic reduction 36

2.1 Introduction 36

2.1.1 Definition of pore, pore parameters and characterization technique 36

2.1.2 Definition of magnetism and characterization technique 37

2.1.3 Introduction of wettability of powders and the measurement of contact angle 40

2.1.4 Introduction, properties, applications and synthesis of porous Si42

2.1.5 Introduction, properties, applications and synthesis of zero valent Fe 46

2.1.6 Introduction, properties, applications and synthesis of transition metal silicide 47

2.1.7 Introduction, property, application and synthesis of FeSi 49

2.2 Experimental 49

2.2.1 Materials 50

2.2.2 Synthesis of materials 50

2.2.3 Characterization 52

2.3 Results and discussion 54

2.3.1 Fabrication of porous silicon (pSi) from tabasheer via magnesiothermic reduction 54

2.3.2 Fabrication of Fe from $Fe(NO_3)_3$•$9H_2O$ via magnesiothermic reduction 57

2.3.3 Fabrication of FeSi from tabasheer and $Fe(NO_3)_3 \cdot 9H_2O$ via magnesiothermic reduction.........59

2.3.4 Controllable fabrication of Fe/Si-based nanoparticles from tabasheer and $Fe(NO_3)_3 \cdot 9H_2O$ via magnesiothermic reduction. 66

2.3.5 Wettability of fabricated FeSi NPs.........70

2.4 Conclusions.........70

Chapter 3. Photothermal properties of FeSi and Fe/Si-based nanocomposites.72

3.1 Introduction.........72

3.1.1 Interaction of light with particles.........72

3.1.2 Photothermal conversion mechanism.........74

3.1.3 Thermal properties.........76

3.1.4 Photothermal performance.........80

3.1.5 Photothermal conversion efficiency (η) and calculation.........83

3.1.6 Photothermal stability.........86

3.2 Experimental.........86

3.2.1 Materials.........87

3.2.2 Characterization techniques.........87

3.3 Results and discussion.........88

3.3.1 Optical properties of materials 88

3.3.2 Photothermal conversion effect 89

3.3.3 Photothermal performance 91

3.3.4 Photothermal conversion efficiency (*η*) 96

3.3.5 Photothermal stability 98

3.4 Conclusions 99

Chapter 4. *In vivo* photothermal therapy of FeSi nanoparticles 101

4.1 Introduction 101

4.1.1 Advantage/disadvantage and positioning of PTT 102

4.1.2 Choice of light wavelength in PTT 104

4.1.3 Introduction of injection pattern for PTT 105

4.1.4 Photothermal materials 106

4.1.5 Comparisons of PTAs 113

4.1.6 Clinical progress of PTT 116

4.2 Experimental 118

4.2.1 Materials 118

4.2.2 *In vivo* PTT 119

4.2.3 *In vivo* biocompatibility of FeSi NPs 120

4.3 Results and discussion 120

4.3.1 Temperature change of tumour after injection and laser irradiation 120

4.3.2 Volume change of tumour after injection and laser irradiation .121

4.3.3 H&E staining of tumor slices (photothermally induced necrosis) and major organs (*in-vivo* biocompatibility data) 123

4.4 Conclusions 124

Chapter 5. Biodegradability investigations of FeSi 126

5.1 Introduction 126

5.1.1 Definition of biodegradability 126

5.1.2 Biodegradable materials and applications 127

5.1.3 Biodegradability in photothermal therapy 130

5.1.4 Strategy for controlling degradation rate 131

5.1.5 Characterization of biodegradability 131

5.2 Experimental and methods 133

5.2.1 Materials and characterization 134

5.2.2 Preparation of SBF solution 134

5.2.3 Immersion test......135

5.3 Results and Discussion 136

5.3.1 Biodegradability test of bulk tabasheer......136

5.2.3 Biodegradability test of fabricated FeSi NPs......137

5.3 Conclusions......141

Chapter 6. Overall conclusions and potential future work......142

6.1 Overall conclusions......142

6.2 Future work......143

7. References......145

Chapter 1. Introduction and Background

1.1 Background to scope of thesis

The overall aim of the research in this thesis was to develop, via **"green" synthesis,** a medically biodegradable novel **nanomaterial** for **photothermal therapy (PTT)** of primary tumours arising from **cancer**. **Silicon** and **iron** were chosen constituents due to their environmental abundance, their ability to degrade via hydrolysis, and a known potential "green" synthesis route from their oxides. We therefore first provide a very basic introduction to some of these above terms, before giving in more detail specific objectives and the layout of the thesis. Papers submitted for publication from the research of this thesis are also provided in this chapter. More detailed background information to appropriately selected topics occurs in later chapters of the thesis.

Nanomaterials [1] are the materials with the nanoscale (1-100nm) at least one dimension of the three-dimensional spatial scale. Due to their small size, they have specific surface effect, tunnel effect and small size effect. Therefore, they show different chemical, mechanical, magnetic, electrical, thermal and optical properties to their bulk counterparts. Nanomaterials can be used for lots of applications, such as biomedical applications, energy field, environmental protection field, aerospace and military industry, catalysis, information field and so on. Nanomaterials can be fabricated via two ways, top-down and bottom-up.

Most top-down methods are physical methods, including high-energy ball milling, laser ablation and plasma sputtering method. While bottom-up methods are mainly chemical methods, including sol-gel method, coprecipitation method, vapor deposition method, hydrothermal/solvothermal method and solution synthesis method.

In recent years, **green synthesis** [2] is a new trend for fabrication of all materials, not just nanomaterials. Green synthesis of materials is an eco-friendly method with less or no negative effect on the environment [3]. There are several requirements and advantages of green synthesis, which can be seen below.

1. No toxic chemicals used, no hazardous waste, and society acceptable
2. Cost effective, locally available, less energy consumed
3. Easily synthesized, no need of high temperature and pressure
4. Good biocompatibility, nontoxic to living organisms
5. Easy to be mass fabrication of nanoparticles (NPs)

Cancer is a complex disease where some cells grow quickly and uncontrollably and spread to other parts of the body. As we know, cancer cause much pain to patients. There are many methods for cancer treatment. The three most popular treatments used for cancer treatment are surgery, chemotherapy and radiotherapy.

Photothermal therapy [4] has gained a considerable attention in cancer therapy due to its nature of physical treatment for many types of cancers with less side effects. Over the past 20 years, some photothermal agents have been developed for photothermal cancer treatment. However, the photothermal agents reported up to date suffer from several limitations, such as low efficiency in delivery to the targeted site with the help of only enhanced permeability and retention (EPR) effect, poor photothermal performance, nonbiodegradable nature and/or unclear long-term biological side effects, which limit their clinical use. Among the photothermal agents, semiconductors [5] have attracted a considerable attention due to relatively low-cost, good photothermal performance and biocompatibility, and many choices of materials.

Silicon (Si)-based materials have been investigated for biomedical applications such as biosensing, drug delivery, and photoluminescence due to their good biocompatibility and biodegradability, rich abundance, unique electronic and optical properties. Therefore, several silicon-based nanoparticles, such as porous silicon (pSi) [6–11], black silicon [12], silicon oxide [13], silicon quantum dots [14], silicon nanosheets [15] and silicene [16], have been investigated for photothermal therapy. Porous silicon nanoparticles could be readily degraded into water-soluble orthosilicic acid ($Si(OH)_4$) and eliminated from the body [17].

Iron (Fe)-based materials have also been investigated for biomedical applications, such as MRI imaging, magnetic hyperthermia and magnetic targeting, due to their special magnetic properties, rich abundance and benign nature. Many Fe-based photothermal agents, such as iron oxide [18–21], iron sulfide [22–27], $FeSe_2$ [28], Fe_5C_2 [29], Fe^{3+} [30] have also been reported for photothermal therapy of cancer. Iron oxide NPs have been found to release Fe ions into the blood during metabolic processes.

1.2 Aims and objectives

As stated above, the overall goal of the research is to prepare a novel iron-silicon based nanoparticles for biomedical applications, using a green synthesis method to fabricate a structure with mesoporous, magnetic and photothermal conversion properties. This requires some enhancement of known synthesis methods and an deep understanding of fabrication mechanism. It also requires investigations of the photothermal conversion, mesoporous and magnetic properties of iron-silicon based nanostructures.

In order to achieve the overall aim, specific objectives of the project are as follows:

1. To prepare a literature review of related work as background for the thesis; (including synthesis, properties and applications of Si, Fe, transition metal silicides and FeSi; magnesiothermic reduction method; porous and magnetic properties; photothermal conversion effect and performance; *in-vivo* photothermal therapy)
2. To learn the basic principles and practical details of the most appropriate characterization techniques;

3. To controllably synthesise, via green magnesiothermic reduction methods, porous Si, zero-valent Fe, FeSi and their mixture; To investigate the fabrication mechanism of Si, Fe and FeSi by magnesiothermic reduction;
4. To investigate and quantitatively compare the porous properties (specific surface area, pore volume and pore size distribution) of the materials using Brunauer–Emmett–Teller (BET) method;
5. To investigate and adjust magnetic properties of the materials via changing the phase content of materials, by using vibrating sample magnetometer (VSM);
6. To investigate the wettability of the materials using contact angle meter;
7. To investigate the photothermal performance, photothermal conversion mechanism and calculate the photothermal conversion efficiency of novel FeSi NPs;
8. To investigate the heat transfer properties of the materials such as heat capacity and thermal conductivity;
9. To reveal *in vivo* photothermal therapy of novel FeSi NPs using mouse tumour model;
10. To investigate *in-vitro* biodegradability of porous Si, Fe and FeSi with simulated body fluid (SBF) and Inductively Coupled Plasma Mass Spectrometry (ICP-MS);

1.3 Layout of the thesis

Chapter 1 introduces the background of the project, the overall aim and specific objectives of the research and an outline of the thesis structure.

Chapter 2 introduces the background of porous Si, zero valent Fe, metal silicide, FeSi nanoparticles, including their synthesis methods, properties and applications. Introduction and characterization of pore parameters, magnetic properties and wettability are included. Practical details of green synthesis of porous Si and new nanomaterials by magnesiothermic reduction and characterization methods of fabricated materials are also included in this chapter.

Chapter 3 introduces the background of optical properties, photothermal conversion and thermal properties, including the interaction of light with particles, photothermal conversion mechanism and thermal transfer from particles to surrounding solution. Introduction and characterization methods of optical and thermal properties are included. Optical and thermal properties of Si, Fe, FeSi and their composites are also presented in this chapter.

Chapter 4 introduces the background of photothermal therapy, including the treatment methods of cancer, advantage/disadvantage and positioning of PTT, Clinical progress of PTT, setup for PTT, photothermal materials and their comparisons. Photothermal performance of the novel FeSi NPs *in vitro* and *in vivo* is presented.

Chapter 5 introduces the background of biodegradability, including the definition, biodegradable materials and their applications, degradation mechanism of porous silicon and iron (Fe), biodegradability in photothermal therapy, strategy for controlling the extent of degradation, characterization of biodegradability. Biodegradability investigations of Fe and FeSi are also presented.

Chapter 6 sums up the new study results and discusses the work for future study.

1.4 List of publications

A full paper "*Green synthesis of iron silicide nanoparticles for photothermal cancer therapy*" has been accepted and published by the journal of *Journal of Materials Chemistry B*.

Chapter 2. Green synthesis of porous Si, porous zero valent Fe and porous FeSi by magnesiothermic reduction

2.1 Introduction

This chapter mainly discusses the introduction, properties, applications and synthesis of porous Si, zero valent Fe, metal silicide, FeSi nanoparticles; introduction of pore and characterization of pore parameters; introduction of magnetism and characterization techniques of magnetism and saturation magnetization; introduction of wettability of powders and the measurement of contact angle.

2.1.1 Definition of pore, pore parameters and characterization technique

The definition of pore is that concave depth is larger than concave diameter. Pore [31] can be divided into closed (C), blind (B), through (T), interconnected (I) pores in Figure 1. R in Figure 1 shows the rough surface instead of pore. Pore can also be divided into three types based on the size, which are micropore (<2nm), mesopore (2-50nm) and macropore (50-7500nm). The pore parameters include specific surface area, pore size distribution, pore volume and porosity. BET, scanning electron microscope (SEM), mercury injection apparatus, bubble pressure method and filter membrane pore size analyzer are used to characterize the pore parameters of materials.

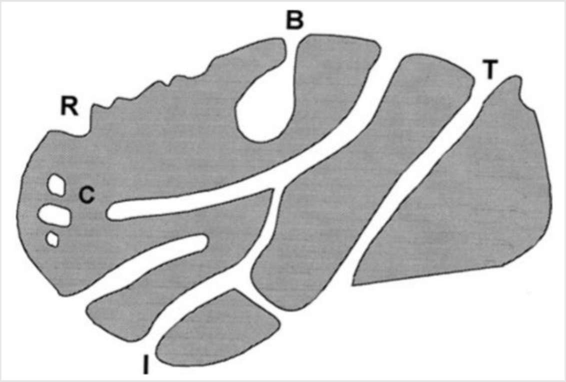

Figure 1 Schematic representation of pore types. C, B, T and I show closed pore, blind pore, through pore, interconnected pore; R shows roughness. Adapted from (Rouquerol, 1990)

2.1.2 Definition of magnetism and characterization technique

Although the magnetism is not related to the photothermal therapy, the magnetic properties can be used for drug delivery and tumour targeting of photothermal agents. Fabricated zero valent iron and iron silicide in this thesis are magnetic and characterized in magnetism, which may be used in biomedical applications in the future. Therefore, magnetism and some related contents are introduced and described here.

Three physical quantities of magnetism are firstly introduced. Saturation magnetization stands for the maximum magnetization of a magnetic material when under an external magnetic field. Remanence stands for the ability of materials to retain magnetization, which equals to the magnetization of the material after the removal of the magnetizing field. Coercivity stands for the ability of magnetic materials to resist demagnetization.

Magnetism [32] can be classified as diamagnetism, ferromagnetism, ferrimagnetism, antiferromagnetism, paramagnetism and superparamagnetism. Among these types, ferromagnetism, ferromagnetism and superparamagnetism gain much attention due to their features. Ferromagnetism has high saturation magnetization and hysteresis loop, because when a field is applied and then removed, the magnetization does not change to original value. While the magnetization of paramagnetism and superparamagnetism becomes zero when the field is removed.

The comparisons of ferromagnetism, paramagnetism and superparamagnetism can be seen in Table 1 and Figure 2a [33]. When the particle size of magnetic nanoparticles is much smaller (less than threshold diameters for superparamagnetism), they will be superparamagnetic. The values of threshold diameters of the materials are different (Figure 2b [34]).

Details	*Ferromagnetism*	*Paramagnetism*	*Superparamagnetism*
Saturation magnetization	high	low	high
Remanence	yes	no	no
Coercivity	nonzero	zero	zero

Table 1 Comparisons of ferromagnetism, paramagnetism and superparamagnetism.

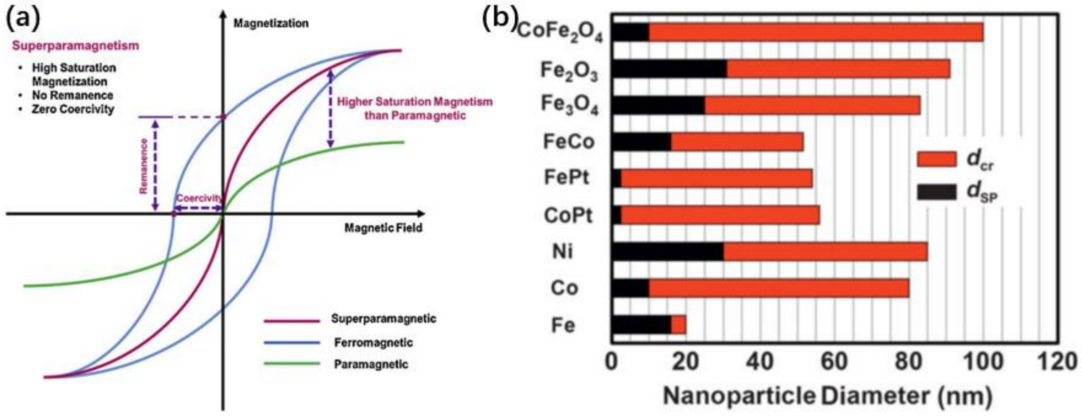

Figure 2 Schematic representation of magnetization characteristics of magnetic materials (a) and threshold diameters for superparamagnetism (d_{SP}) and maximum monodomain critical diameters (d_{cr}) for spherical nanoparticles (b). Adapted from (Mohammed 2017; Majetich 2013).

The Curie temperature (Tc) [35] is the temperature above which the spontaneous magnetization in magnetic materials falls to zero, and it is the critical point at which ferromagnetic or ferrimagnetic materials change into paramagnetic materials. The material becomes a ferromagnet when the temperature is below Curie point, while when the temperature is above Curie point, the material becomes paramagnetic.

Superconducting quantum interference devices (SQUID), physical property measurement system (PPMS) and vibrating sample magnetometer (VSM) are used to characterize the magnetism and saturation magnetization of materials.

2.1.3 Introduction of wettability of powders and the measurement of contact angle

Wettability [36] involves the phase interfaces among gas, liquid and solid. Based on the wettability, waterproof materials, self-cleaning materials and lubricant materials are fabricated for oil industry, printing/dyeing, mineral flotation, construction (coating), agriculture (pesticide spray), biomedical applications.

Contact angle [36] is usually used to measure the wettability of a solid surface. The angle between the solid-liquid interface and the gas-liquid interface through the liquid interior is called the contact angle, which is represented by θ [37] (Figure 3). It is usually calculated by the Young equation below, which is the basis for the study of wetting. γ_{SV} , γ_{SL} , and γ_{LV} relate the surface tension between the three phases: solid, liquid and gas.

$$\cos\theta = \frac{\gamma_{SV} - \gamma_{SL}}{\gamma_{LV}}$$

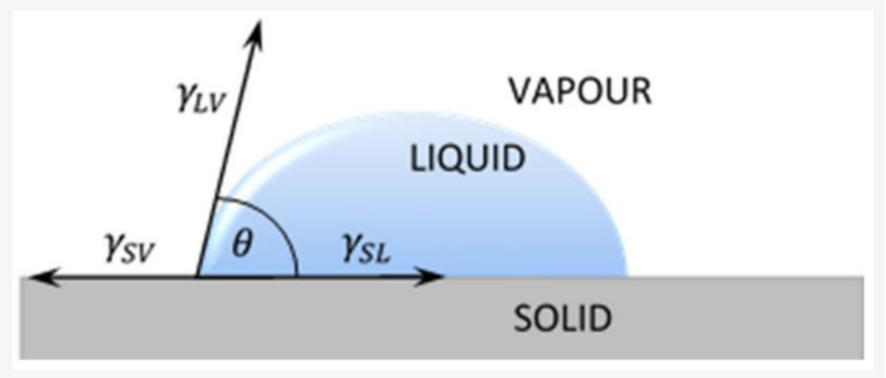

Figure 3 Schematic representation of contact angle. (Adapted from Liber-Kne´c 2021).

Minimum and maximum of contact angle are 0° and 180° respectively. The relationship between contact angle and wettability can be seen in Table 2Table 2 Relationship between contact angle and wettability.

value of θ	liquid wets the solid surface
θ=0	completely wetting
0<θ<90°	hydrophilic; partially wetting; the smaller the angle, the better the wettability
θ=90°	boundary between wetting and not wetting
90°<θ<150°	hydrophobic; liquid cannot wet the solid surface
150°<θ<180°	super-hydrophobic
θ=180°	completely not wetting; liquid tends to condense into spheroidal droplets on solid surface

Table 2 Relationship between contact angle and wettability.

Contact angle (θ) of materials can be achieved by contact angle meter [38] (contour image analysis method) or capillary rise method [39,40] (penetrant method, weighing method) for understanding the wettability of materials (in Figure 4).

For contact angle meter, powders need to be squashed into tablets for testing. The accuracy of the contact angle measurement is affected by the difference of compression degree and surface roughness. For capillary rise method, the method of packing column and degree of packing need to be the same every time for obtaining accurate results. It is suitable for the hydrophilic powders.

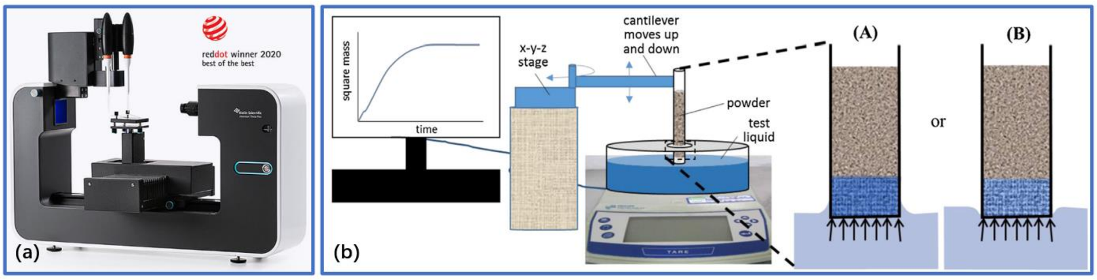

Figure 4 Optical photo of contact angle meter (a) and schematic representation for Washburn capillary rise (b). In figure b, the enlarged right sketches are the scenarios when the tube touches the liquid using (A) a hydrophilic tube (<90°)-liquid climbs up the outside of the tube wall or (B) a hydrophobic tube (>90°)-liquid is compressed at the tube/liquid/air interface. Adapted from (https://www.biolinchina.com/attension; Alghunaim 2016).

2.1.4 Introduction, properties, applications and synthesis of porous Si

There are lots of methods to fabricate porous silicon nanoparticles, which can be mainly summarize as two routes to porous silicon, via solid silicon and using chemical conversion (Figure 5). Porous silicon nanoparticles can be fabricated by anodization, HNO_3/HF vapor etching, lithographic etching, and photoetching[17]. The cost of these processes is high, so they are suitable for medical applications.

For lower value, high volume pSi products for some applications such as lithium-ion batteries, cheaper fabrication methods are needed. Chemical conversion of silica, silane and silicon tetrachloride, which are waste products or inexpensive, can meet the requirement. Among chemical conversions, thermal reduction is the interested process for synthesis of porous silicon from precursors such as silica and silicon-based molecules, including mainly carbothermic [41,42], magnesiothermic [43,44], and aluminothermic [45,46] reduction. Among these reductions, carbothermic reduction requires higher temperature such as 1700℃, aluminothermic reduction leads to incomplete reduction due to surface passivation, magnesiothermic reduction is a popular choice for preparing pSi with lower temperature around 650℃, which can be conducted in a tube furnace, autoclave or via milling. Silica is the popular precursor of porous silicon, which are usually from sand [47] and plant such as rice husk, bamboo leaves and tabasheer with low cost, and are safe for lithium-ion battery and medical applications.

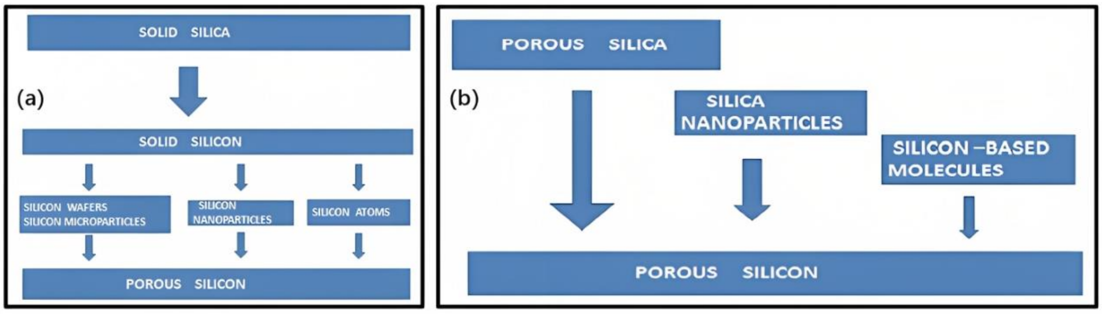

Figure 5 Routes to porous silicon via solid silicon and using chemical conversion. Adapted from (Canham 2014).

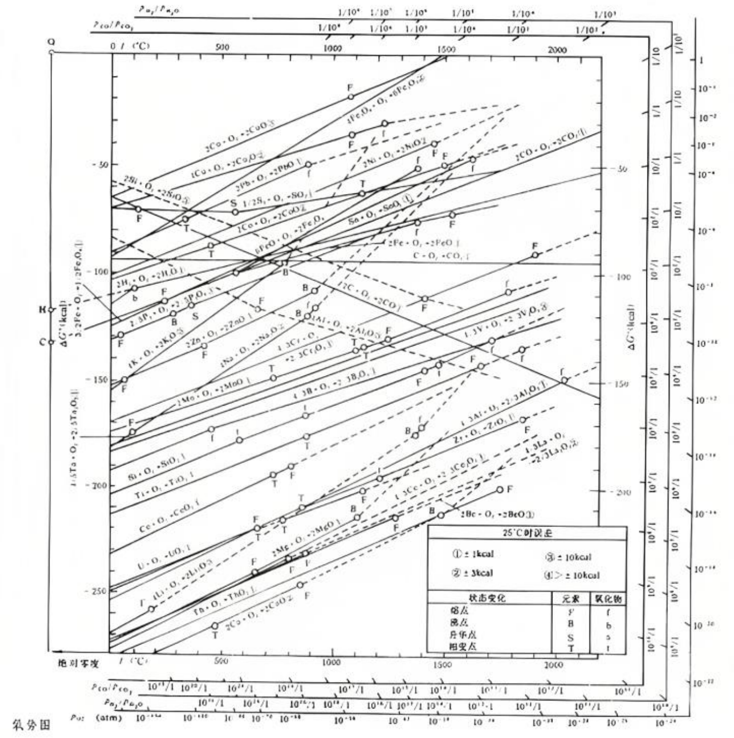

Figure 6 Schematic representation of oxygen-potential diagram. Adapted from (Li 2005).

Based on the oxygen-potential diagram [48] in Figure 6, we can see that silicon can be reduced from silica by magnesium (Mg) and aluminum (Al) due to their high reducibility. For magnesiothermic reduction, the precursors can be metal oxide + silica, metal oxide + silicon and metal + silica for preparing metal silicide.

Although silicon has higher reducibility compared to carbon, silicon can be reduced from silica by carbon at much higher temperature due to the law of low boiling point material (CO, gas) can be obtained from high boiling point material (SiO_2) at high temperature and dry state.

Si-based materials have been investigated in biomedical and energy applications. Due to some properties such as photoluminescence, adjustable porosity, pore volume and specific surface area, high reactivity, biocompatibility and biodegradability, porous silicon can be used for drug delivery.

Porous silicon is utilized as a photothermal agent with biocompatibility and biodegradability for photothermal therapy upon exposure to NIR light [49].

Photovoltaic solar cells produced in the world mainly are composed of silicon (in the type of single crystal, multicrystalline, amorphous, etc.) [17]. The conversion efficiency of monocrystalline silicon solar cell is the highest, which can be up to 25%, and the actual conversion efficiency is about 18%. For the multicrystalline solar cells, the values are 20% and 15%, while for the amorphous silicon solar cells, it is less than 10%. Porous silicon can increase the efficiency of solar cells due to the reduction of light reflection from cell surface.

Silicon is an attractive material for anode of lithium-ion batteries. But large volume changes with the formation and decomposition of Si-Li alloy during charging and discharging lead to the severe capacity fading of batteries. The nanostructure and porous structure of silicon can cope with this problem.

2.1.5 Introduction, properties, applications and synthesis of zero valent Fe

Nanoscale zero-valent iron particles (NZVI) has received much attention due to its small size, high specific surface area, high reactivity and magnetization. Due to above properties, NZVI can be used as environmental restoration agents for removal of heavy metal ions from groundwater such as Cr^{6+} [50,51] or degradation of indicator or dye such as bromothymol blue. NZVI can also be used for medical application such as drug delivery.

NZVI can be prepared by physical methods (ball milling, physical vapor deposition, sputtering, plasma) and chemical method (chemical vapor deposition, solvothermal method, electrodeposition, reduction in solid, liquid or gas phase). Reduction in solid means the reduction of iron oxide to NZVI by hydrogen or magnesium powder. Iron oxide can be purchased or prepared by the thermal decomposition of $Fe(NO_3)_3 \cdot 9H_2O$. Reduction in liquid means the reduction of iron ions in the solution to NZVI by reducing agent, which can be extracted from leaves of plant [52–54], like grape, tea and tree.

Porous NZVI gains more attention due to its porous structure and larger specific surface area with above existed properties. It can be prepared by combustion synthesis [55] and magnesiothermic reduction from iron oxide used in this thesis. From the oxygen-potential diagram, it can be known that NZVI or other zero-valent metals can be prepared by magnesiothermic reduction from their oxide.

However, there exists some problems of NZVI, such as easy to agglomerate due to high surface energy, reactivity and magnetization and easy to be oxidized. It can be solved by capping agents extracted from plants.

2.1.6 Introduction, properties, applications and synthesis of transition metal silicide

Transition metal silicides are kinds of intermetallic compounds, generated by transition metals and earth-abundant silicon. The transition metal silicides [56,57] have gained much attention due to low-cost, special physical and chemical properties. Therefore, they can be used in thermoelectrics and catalysis. They can be used in electrocatalysis and photocatalysis for fields of energy conversion and renewable energy due to competitive catalytic activity compared to those of noble metals.

There are usually several phases of transition metal silicides for specific transition metals and silicon. Two examples of phase diagrams of iron silicide [58] and nickel silicide [59] are showed in Figure 7. Therefore, the suitable ratio of transition metal to silicon and temperature are required for preparing highly pure specific phase of transition metal silicides.

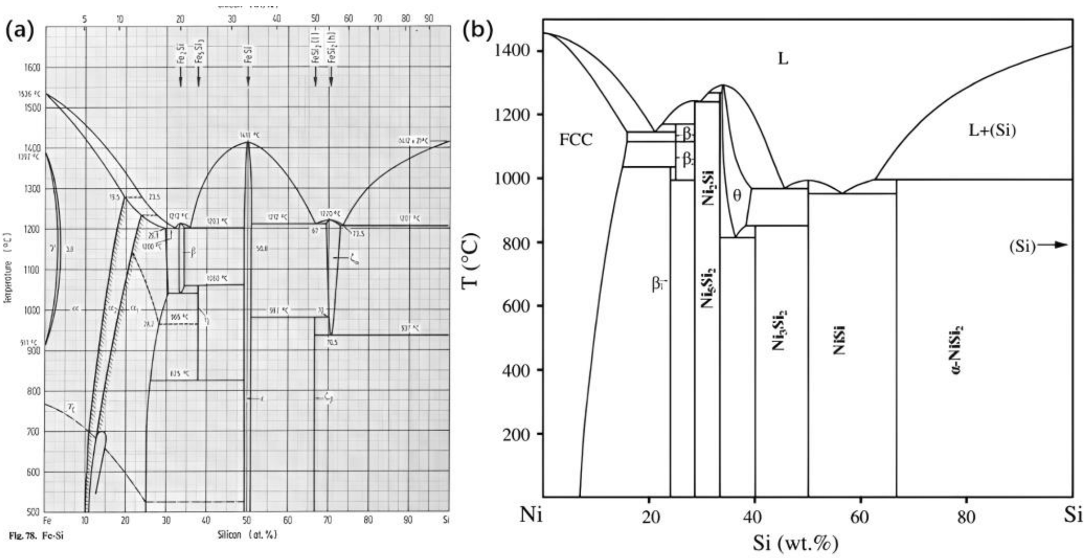

Figure 7 Schematic representation of binary phase diagram of Si-Fe (a) and Si-Ni (b). Adapted from (Von Goldbeck 1982; Okamoto 2000).

For preparing metal silicides, the precursors can be divided into single-source and dual-source. For single-source precursors, metal organic chemical vapor deposition (CVD) and pyrolysis of metal-containing polysilane are the methods to prepare metal silicides. For dual-source precursors, there are many methods for preparing metal silicides, such as arc melting, mechanical alloying, solid-state metathesis reactions, molten salt reaction technology, microwave assisted synthesis, chemical vapour deposition (CVD) and solution synthesis route.

Among them, molten salt reaction technology uses metal oxide and silica as precursors, and uses K, Na, C or Mg as reducing agent. In addition, the method may have industrial scalability in the future.

Based on the oxygen-potential diagram in above Figure 6, we can know which metal can be reduced from their oxide by magnesium and then what metal silicide can be prepared.

2.1.7 Introduction, property, application and synthesis of FeSi

Iron silicide is a kind of transition metal silicide. In the above Figure 7, there exist several phases in the Fe-Si phase diagram [60],[60] such as Fe_2Si, Fe_5Si_3, FeSi and $FeSi_2$. Among them, β-$FeSi_2$ is popularly used as thermoelectric materials. While ε-FeSi is a narrow-bandgap (0.13 eV) [61,62] semiconductor that has been classified as a hybridization-bandgap semiconductor. It has been studied many years due to its unusual magnetic and electrical properties. FeSi doesn’t have many applications, photothermal therapy may be one in the future. Until now, various methods such as chemical vapor deposition (CVD) [63,64], magnetron sputtering [65], molten-salt method [66] and magnesiothermic reduction have been developed to fabricate ε-FeSi phase.

2.2 Experimental

2.2.1 Materials

Iron nitrate nonahydrate was purchased from Aladdin (Shanghai, China); tabasheer (biogenic silica, SiO_2) was purchased from Bristol Botanicals (Bristol, UK); ethanol (C_2H_5OH) was purchased from Xilong (Shantou, China); magnesium powder (Mg) was purchased from Energy Chemical (Shanghai, China); potassium chloride (KCl) was purchased from Aladdin (Shanghai, China); hydrochloric acid was bought from Dongjiang (Dongguan, China); ammonium chloride (NH_4Cl) was bought from Macklin (Shanghai, China). 1M HCl (pH=0) was prepared by diluting the concentrated HCl. NH_4Cl (pH=5.7) solution was prepared by adding 0.5g NH_4Cl to 50mL water.

2.2.2 Synthesis of materials

The pSi nanoparticles (pSi NPs) were synthesized using green magnesiothermic reduction from tabasheer, in a similar manner as used in the previous reports [67–69]. Ball miller is used to prepare white powder from bulk of tabasheer. Tabasheer powder, magnesium powder and KCl are mixed by mortar. The mixture is put into the tube of furnace for magnesiothermic reduction under Ar atmosphere with 650℃ for 3 hours. After the HCl (1M) washing of above products, brown pSi can be fabricated. Metallic iron nanoparticles (Fe NPs) were synthesized from Fe_2O_3 using magnesiothermic reduction and NH_4Cl (pH 5.7) solution washing. Red Fe_2O_3 is firstly prepared via heating $Fe(NO_3)_3{\bullet}9H_2O$ under 400℃. After magnesiothermic reduction and NH_4Cl washing, black ZVINs can be fabricated. The synthesized pSi NPs and Fe NPs were used as comparison for evaluating photothermal performance.

The porous FeSi NPs were synthesized from tabasheer and $Fe(NO_3)_3$•$9H_2O$ using green and low-cost magnesiothermic co-reduction method with the fabrication process being shown in below Figure 15. In a typical synthesis, $Fe(NO_3)_3$•$9H_2O$ was dissolved in ethanol, tabasheer powder was then added into the resulting solution. The mixture was stirred overnight at room temperature for impregnation of $Fe(NO_3)_3$•$9H_2O$ into the pores of porous SiO_2 during the evaporation process of ethanol. The mixture was heated to 400 ℃ in an oven to obtain porous SiO_2/Fe_2O_3 mixture by removing ethanol and bound water followed by decomposition of $Fe(NO_3)_3$•$9H_2O$ to Fe_2O_3. After grinding of the solids, the resulting powders were mixed with Mg and KCl at a desired proportion, followed by magnesiothermic co-reduction in a tube furnace at 650 ℃ under an Ar atmosphere for 3 hours at a heating ramp rate of 10 °C/min. The product was washed by 1M HCl solution under magnetic stirring for 5 hours, washed again with water for three times and then dried in the oven to produce powders of FeSi NPs. After treatment of ultrasonic homogenizer (JY92- II N, Scientz), the narrowly-sized pFeSi NPs were obtained by gradient centrifugation.

2.2.3 Characterization

X-ray Powder Diffraction (XRD) was used to characterize the composition of synthesized samples and the crystal structure. Scanning Electron Microscopy (SEM) was used to investigate the morphologies of nanoparticles. Transmission Electron Microscope (TEM) was used to give more clear morphologies and images of materials compared with SEM and light microscope, which can magnify a small particle of about 2nm. Energy-Dispersive X-Ray Spectroscopy (EDS) was used to give the element composition of materials within a spot size of a few microns, which can also be used for giving the change of element composition along a line or element composition maps over a broader raster area. Brunauer-Emmett-Teller (BET) technique was used for quantitative analysis of specific surface area and porous structure such as pore size distribution and pore volume. Integrated Physical Property Measurement System (PPMS) was used to determine the magnetic characteristics of the materials.

Details	***XRD***	***SEM***	***TEM***	***EDS***	***BET***	***VSM***
Fundamental principles	Bragg's Law ($n\lambda=2d\sin\theta$)	Electron-sample interactions producing signals	Electron beam focusing on specimen to produce magnified/detailed image due to transmission,	Interaction of electron beam with sample produces x-rays	Physical adsorption of inert gas	Faraday's Law of Induction, changing magnetic field produce electric field

			scattering, diffraction			
Instrumentation	X-ray tube, sample holder, X-ray detector	Electron gun, lenses, sample stage, scanning coil, detectors for signals, vacuum/cooling system	Electron gun, image producing/ recording system	X-ray detector, liquid nitrogen for cooling, software to collect and analyze energy spectra	Main body, balance, degassing system, liquid nitrogen, gas, computer	External magnetic field, vibrating system, signal detection
Applications	Metallurgy, materials, petroleum, chemical engineering, scientific research, aerospace	Nanomaterials, rock and soil, graphite, ceramics	Materials science, biology	Macromolecule, ceramic, concrete, biology, mineral, fiber, metal, coating, jewelry	Powders, nanomaterials, porous materials, adsorption, drug delivery	Magnetic materials, superconductor
Strengths	Powerful and rapid technique for identification of an unknown mineral	Minimal sample preparation, rapid data acquisition	Powerful magnification, high-quality images, vast information on materials	Quickly identify unknown phases prior to quantitative analysis, semiquantitative mode	Simultaneous acquisition of surface area and pore size data, non-destructive method	High precision measurements
Limitations	Powder with small size, detection limit is 2%	Dry solid samples, conductive	Expensive/tedious specimen preparation, sensitive to vibrations	Energy peak overlaps among different elements, cannot detect light elements	Closed pores are not accessible via the material surface	Cannot test radioactive/toxic samples

Sample collection, preparation	Grinding samples to less than 5μm	Conductive coating needed (C, Au)	Samples mounted on copper grids for viewing	Same as SEM/TEM	Powders, 0.1-0.5g	Diameter (<2-3mm), 10-30 mg
Data collection, results, presentation	Presented as peak positions at 2θ and X-ray counts (intensity)	SEM images	TEM images	Plot of x-ray counts vs energy (in keV)	Nitrogen adsorption/desorption isotherm diagram, size distribution	Hysteresis loops, magnetization curves (M-H)
Equipment used	D8 Advance ECO	TESCAN MIRA3	Talos F200X G2	Oxford EDS	ASAP 2020 Plus	MPMS 3 (Quantum Design)

Table 3 Comparisons of the techniques used for different characterisations.

2.3 Results and discussion

2.3.1 Fabrication of porous silicon (pSi) from tabasheer via magnesiothermic reduction.

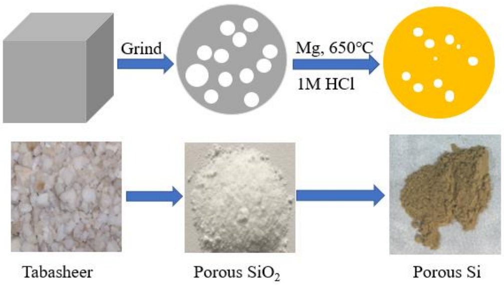

Figure 8 Schematic illustration showing the fabrication of pSi NPs and corresponding optical images of the product in each stage.

$$SiO_2 + 2Mg = Si + 2MgO \cdots\cdots\cdots\cdots (2\text{-}1)$$

In this thesis, porous silicon is fabricated by magnesiothermic reduction from tabasheer (SiO_2) with above chemical reaction (2-1). Figure 8 is the schematic illustration for fabricating of pSi NPs and corresponding optical images of the product in each stage. To observe phase composition, morphology, and pore parameters, tabasheer and fabricated silicon are characterized by XRD, SEM and BET. From the XRD result in Figure 9, we can confirm that the sample fabricated is silicon. The hump around 20° shows the uncomplete reduction of amorphous SiO_2. The brown colour of powders in Figure 8 also confirms the fabrication of silicon.

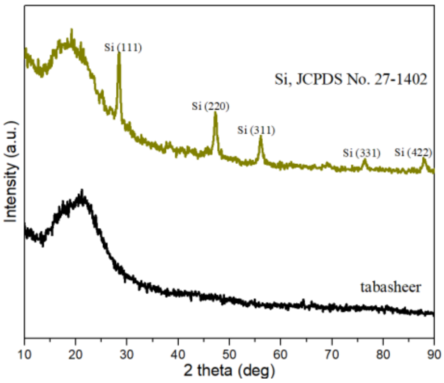

Figure 9 XRD pattern of tabasheer precursor and fabricated biogenic silicon.

From the SEM images in Figure 10, surface morphology can be seen, including the particles and the pores. The size distribution of tabasheer powder is large because the sample is prepared by grinding.

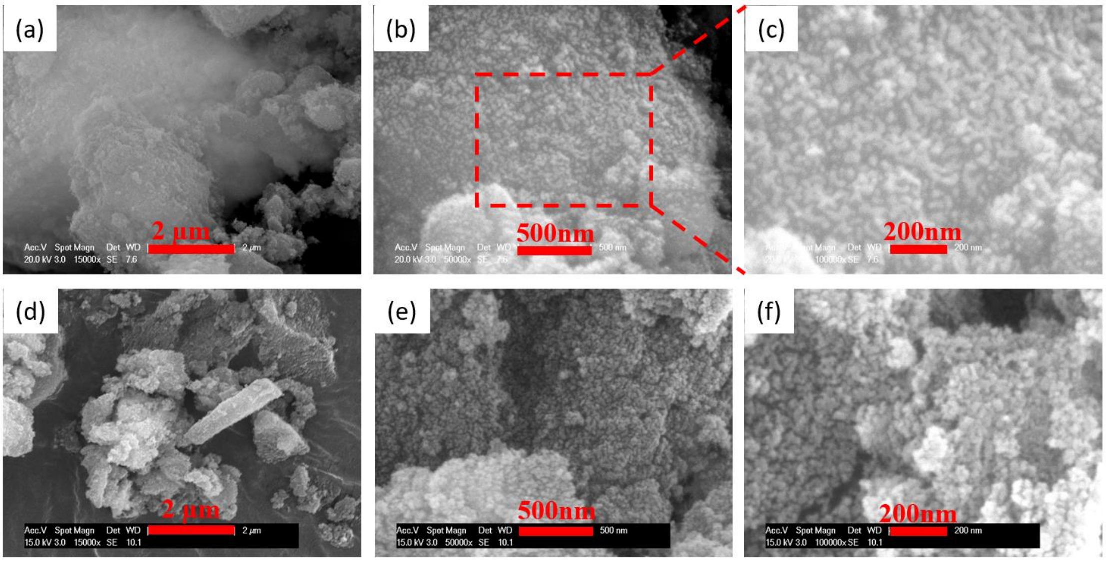

Figure 10 SEM images of the tabasheer (a)-(c) and the biogenic silicon (d)-(f).

From the Figure 11, we can know that tabasheer and silicon both show typical class IV isotherms with hysteresis loops [70], which suggest a mesoporous structure. For the tabasheer, surface area is 261 m^2/g, with BJH pore volume 0.94 cm^3/g and average pore diameter 14 nm. For the porous silicon, surface area decreases to 209 m^2/g, pore volume to 0.67 cm^3/g and average pore diameter to 13 nm (80%, 71% and 88% of tabasheer respectively). pSi has a wider pore size distribution compared with tabasheer (Figure 11b).

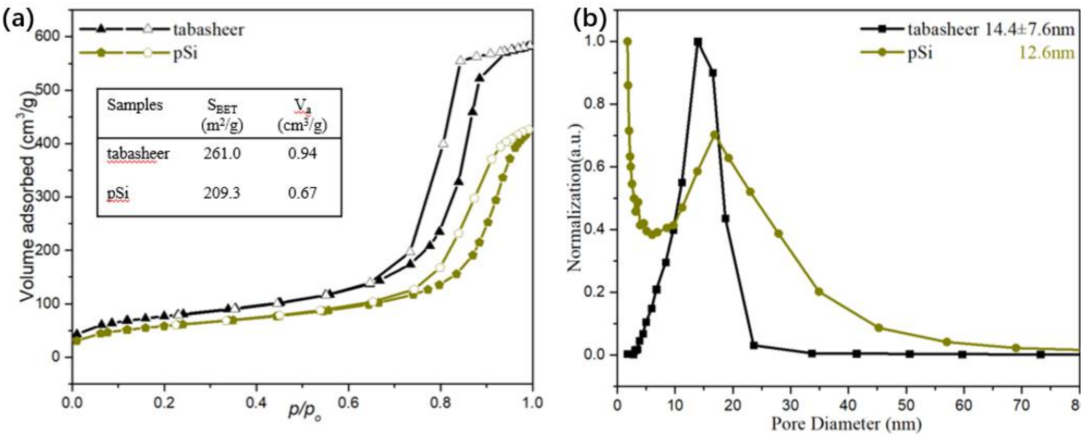

Samples	S_{BET} (m^2/g)	V_a (cm^3/g)
tabasheer	261.0	0.94
pSi	209.3	0.67

Figure 11 N_2 adsorption-desorption isotherm and the corresponding pore size distribution curve of the tabasheer precursor (a) and biogenic silicon (b).

2.3.2 Fabrication of Fe from $Fe(NO_3)_3 \bullet 9H_2O$ via magnesiothermic reduction.

In this thesis, zero-valent iron nanoparticles (ZVINs) are fabricated by magnesiothermic reduction from Fe_2O_3 and NH_4Cl washing with below chemical equation (2-2). To observe phase composition, morphology, pore parameters and magnetization, ZVINs are characterized by XRD, SEM, BET and VSM. From the XRD result in Figure 12, we can see that the sample fabricated is Fe (PDF#06-0696) with a relatively high purity, which is similar with commercial Fe nanoparticles.

$$Fe_2O_3 + 3Mg = 2Fe + 3MgO \cdots\cdots\cdots\cdots (2\text{-}2)$$

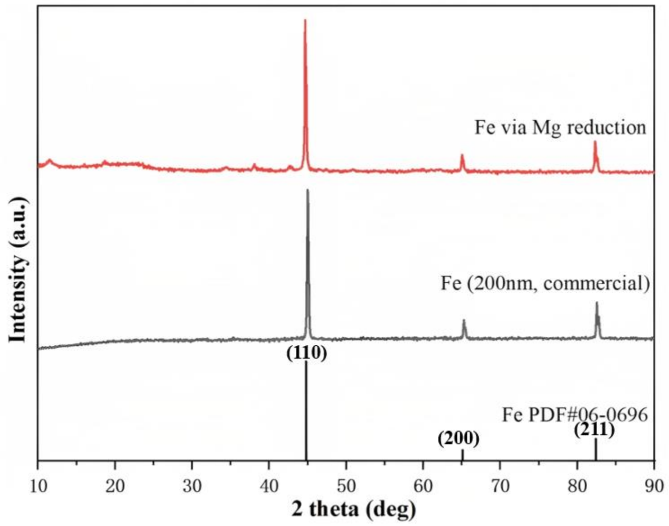

Figure 12 XRD pattern of fabricated iron (Fe) and commercial iron (Fe) nanoparticles.

From the SEM images in Figure 13, the particles show structures of flower petals with particle size of 500nm.

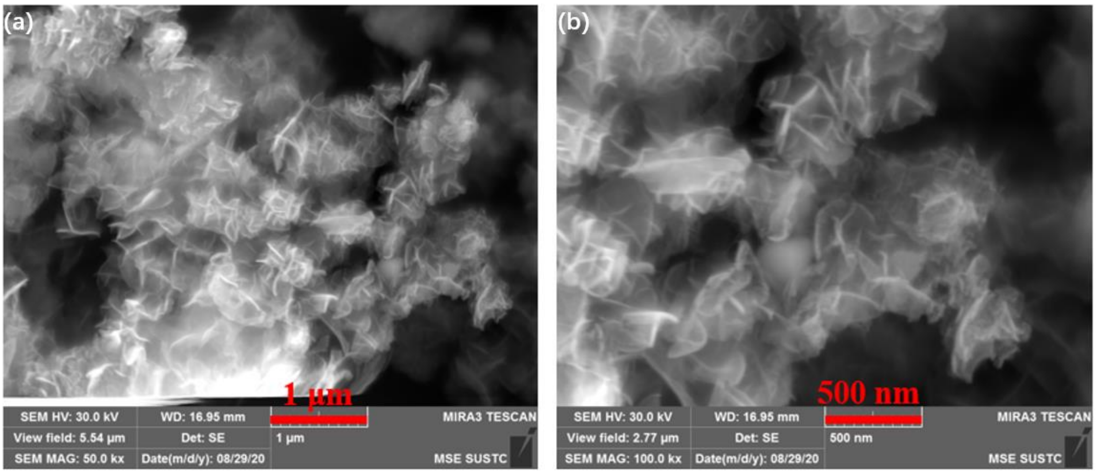

Figure 13 SEM images of the fabricated Fe NPs.

From Figure 14 below, we can see that fabricated Fe NPs show a paramagnetic property, with 83 emu/g saturation magnetization at room temperature.

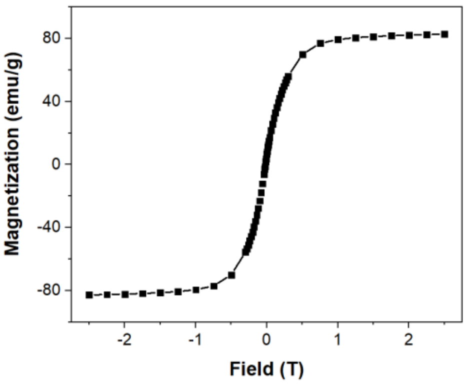

Figure 14 Magnetization curves of fabricated iron (F-Fe) nanoparticles.

2.3.3 Fabrication of FeSi from tabasheer and $Fe(NO_3)_3 \bullet 9H_2O$ via magnesiothermic reduction.

From above, we can know both Fe_2O_3 and SiO_2 can be reduced to Fe and Si respectively by Mg. The product of the reduction in the form of molten Fe and Si is anticipated to form a Fe-Si binary phase. Therefore, FeSi has been synthesized by the below chemical equation (2-3).

$$2SiO_2/Fe_2O_3 + 7Mg = 2FeSi + 7MgO \cdots\cdots\cdots\cdots (2\text{-}3)$$

Figure 15 is the schematic illustration for fabricating of FeSi NPs and corresponding optical images of the product in each stage. The bulks of tabasheer were first ground into white powders. $Fe(NO_3)_3 \bullet 9H_2O$ was dissolved in ethanol and a certain amount of tabasheer powders were added into the solution. After evaporation of ethanol and subsequent heating at 400 °C, a Fe_2O_3/SiO_2 mixture was obtained. From Figure 15, we can see that the colour of tabasheer powders changed from white to yellow when mixed with Fe_2O_3 and thermally treated at

400 °C. The magnesiothermic co-reduction and acid washing of the Fe_2O_3/SiO_2 mixture resulted in a dark powder of FeSi NPs.

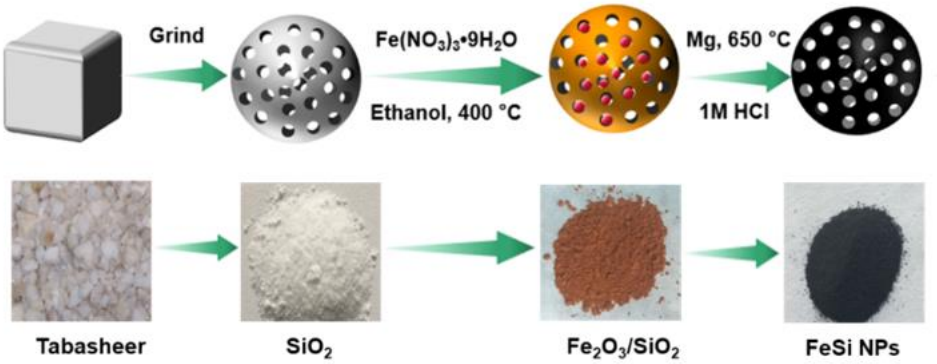

Figure 15 Schematic illustration showing the fabrication of porous FeSi nanoparticles (FeSi NPs) for photothermal therapy and photos of corresponding products collected in each stage.

The XRD patterns in Figure 16 confirmed the phases of original amorphous SiO_2, Fe_2O_3/SiO_2 mixture and final cubic FeSi (JCPDS card, no.38-1397) of the final product. Space group of FeSi was identified as $P2_13$ with a=b=c=4.488 Å. No other XRD peaks outside these phases were detected, indicating the high purity of the final product with noisy base lines indicating incomplete crystallization.

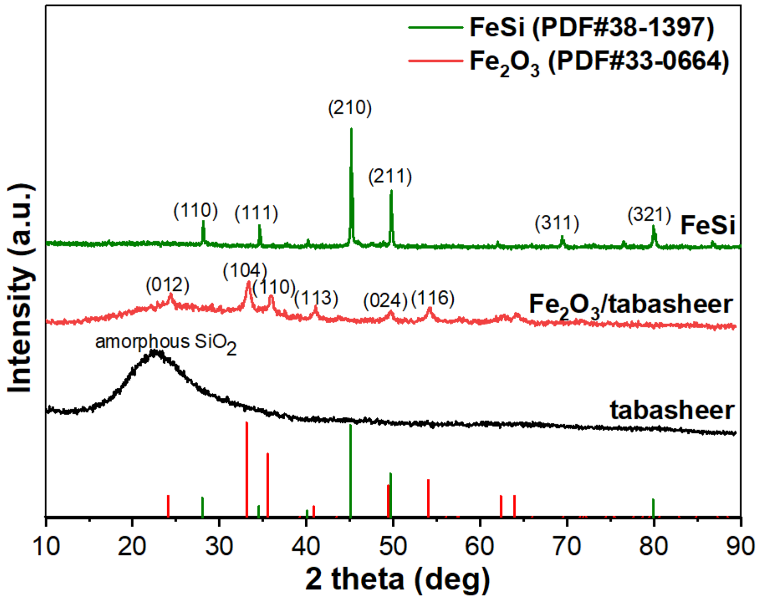

Figure 16 XRD patterns of the biogenic feedstock and fabricated materials.

The scanning electron microscopy (SEM) image in Figure 17(a) reveals the diameters of as-made FeSi NPs mostly being around 60 nm. Some larger particles may be the result of aggregation of small particles. HRTEM image in Figure 17(b) shows uniform lattice fringes across the whole particle, with the characteristic interplanar distances corresponding to cubic ε-FeSi (210).

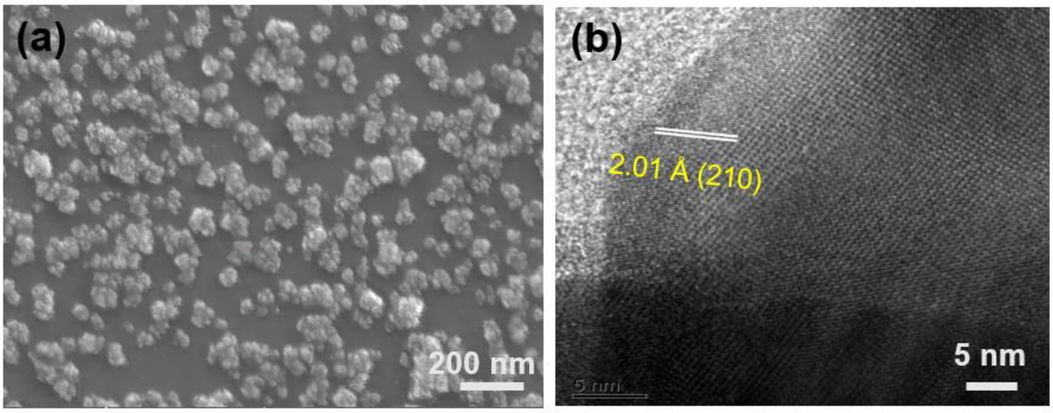

Figure 17 SEM image of F-FeSi NPs (a); HRTEM images of F-FeSi NPs (b).

The EDX spectrum in Figure 18 shows relative content of Fe and Si by the atom percentage being 44.2% and 55.8% respectively, with an atom ratio of Fe to Si close to 1 in FeSi NPs. Note that elements of C, O and Cu in the spectrum come from carbon-coated copper TEM grids.

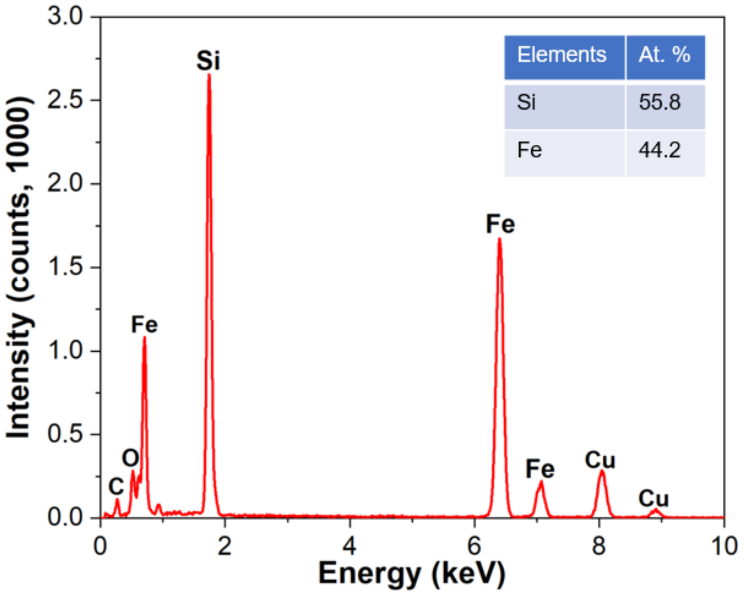

Figure 18 EDX spectrum of the F-FeSi samples, with inset table presenting elemental ratios (atom percentages) calculated using EDX software.

Figure 19 shows a narrow particle size distribution of FeSi NPs measured with dynamic light scattering in deionized H_2O. The measured average size of hydrodynamic diameter is around 115 nm, which is in the same order of magnitude of the size measured from SEM images.

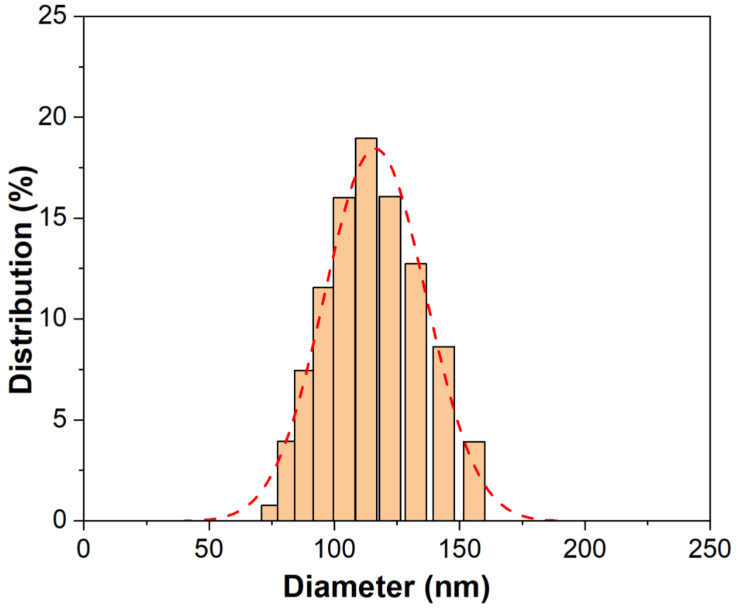

Figure 19 Particle diameter distribution of F-FeSi measured with the DLS with the NPs being dispersed in deionized H_2O prior to the measurement.

The synthesized FeSi NPs were also found to be of porous structures which arise from the porous nature of precursor tabasheer (SiO_2) and the removal of MgO as a by-product by acid washing using HCl solutions. The nitrogen adsorption/desorption isotherms of FeSi NPs in Figure 20 were of the IV isotherm type, indicating the presence of mesoporous structure in FeSi NPs. The BET surface area of FeSi NPs was determined to be 90 m^2/g and the pore volume of 0.21 cm^3/g. The average pore size was estimated to be 9.4 nm based on the Barrett-Joyner-Halenda (BJH) theory.

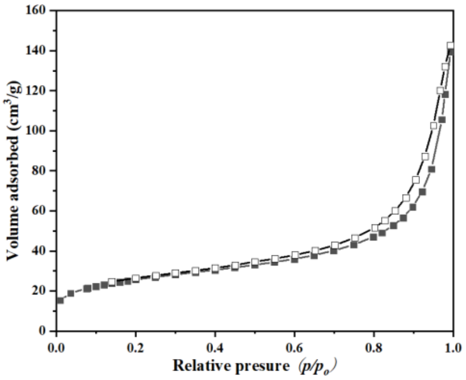

Figure 20 N_2 adsorption-desorption isotherm of the fabricated FeSi NPs.

The FeSi showed a paramagnetic nature (Figure 21) with a saturation magnetization of 4.6 emu/g at room temperature, which is much smaller compared to above fabricated ZVINs (83 emu/g).

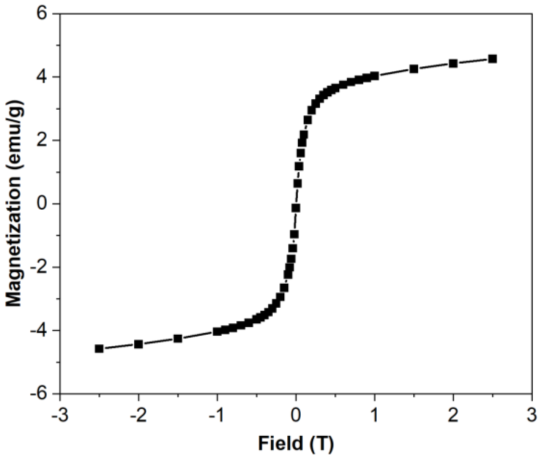

Figure 21 Magnetization curves of fabricated FeSi nanoparticles.

2.3.4 Controllable fabrication of Fe/Si-based nanoparticles from tabasheer and $Fe(NO_3)_3 \cdot 9H_2O$ via magnesiothermic reduction.

From above experiments, we know that SiO_2, Fe_2O_3 and their mixture can be reduced to Si, Fe and FeSi by Mg. NH_4Cl solution cannot wash away iron (Fe) after magnesiothermic co-reduction, while HCl solution can. Therefore, different final products can be obtained from the mixture of Fe_2O_3/SiO_2 with different content of Fe_2O_3 via magnesiothermic co-reduction and different solutions washing.

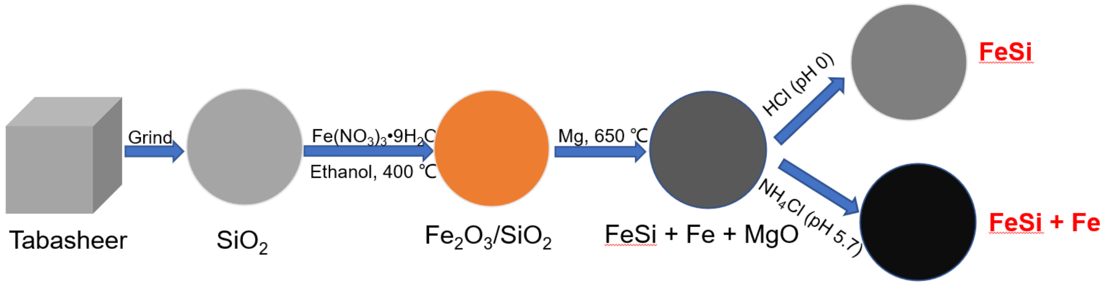

Figure 22 Schematic illustration showing the fabrication of Fe/Si-based nanoparticles.

Here four different contents of Fe_2O_3 of the mixture of Fe_2O_3/SiO_2 were designed, which are labelled as A, B, C and D (atom ratios of Fe/Si are 0.375:1, 1:1, 1.72:1 and 8:1 respectively). The products of magnesiothermic reduced A, B, C and D were washed by HCl (pH=0) and NH_4Cl (pH=5.7) separately.

From Figure 23a we can see that with the increasement of Fe_2O_3 content after HCl washing, α-$FeSi_2$ and Si in the final phases decrease, while ε-FeSi increases. In sample A, the phases are FeSi, α-$FeSi_2$ and Si. In sample B, the main phase is FeSi, there are also a little α-$FeSi_2$ and Si. In sample C, the main phase is FeSi, there are also a little α-$FeSi_2$. While In sample D, the main phase is FeSi. From Figure 23b we can see that with the increasement of Fe_2O_3 content after NH_4Cl washing, Fe in the final phase increases, while α-$FeSi_2$ and Si decrease. In sample D, the main phase is Fe.

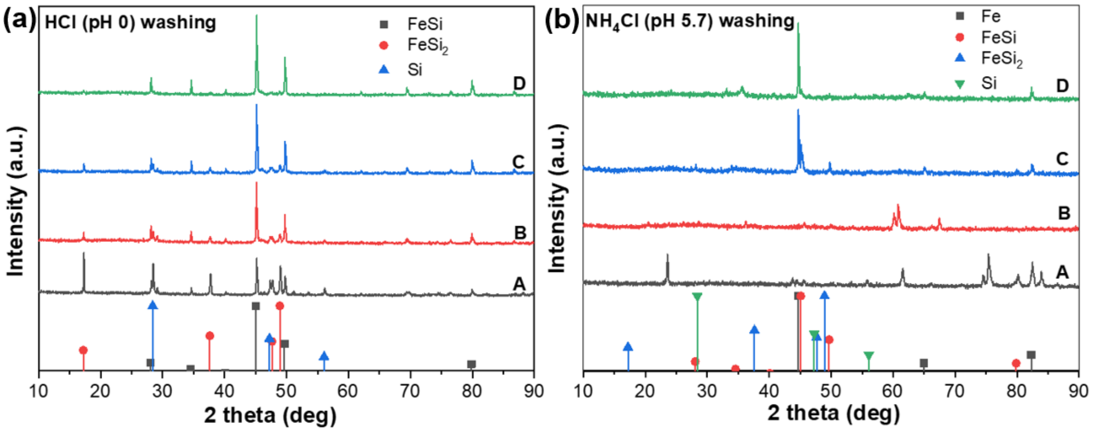

Figure 23 XRD spectrums of the materials fabricated by HCl washing and NH_4Cl washing. A-D refer to varying feedstock compositions, as described in the text.

For fabricating pure FeSi NPs, the atom ratios of Fe/Si in the precursor of Fe_2O_3/SiO_2 should be larger than 8:1. In that case, silicon from SiO_2 will combine surrounding iron to form FeSi. Other iron will exist as zero-valent Fe. HCl will wash away the redundant zero valent Fe. Therefore, the yield is low. The relationship between yield and purity should be considered.

From Figure 24a we can see that the saturation magnetization of A, B, C and D after HCl acid washing remain a much low value (2-6 emu/g), that is because α-

$FeSi_2$ and FeSi have weak magnetization and Si has diamagnetic behaviour based on the literatures. While after NH_4Cl washing, A, B, C and D all have a higher value compared to that after HCl washing. From A to D, the saturation magnetization increases from 7.4 emu/g to 47.4 emu/g, which can be seen in Figure 24b. The reason is that Fe has a much high magnetization (83 emu/g), which corresponds with the XRD results. If considering the pure Si and Fe, the magnetization curve of the materials can be seen in Figure 25.

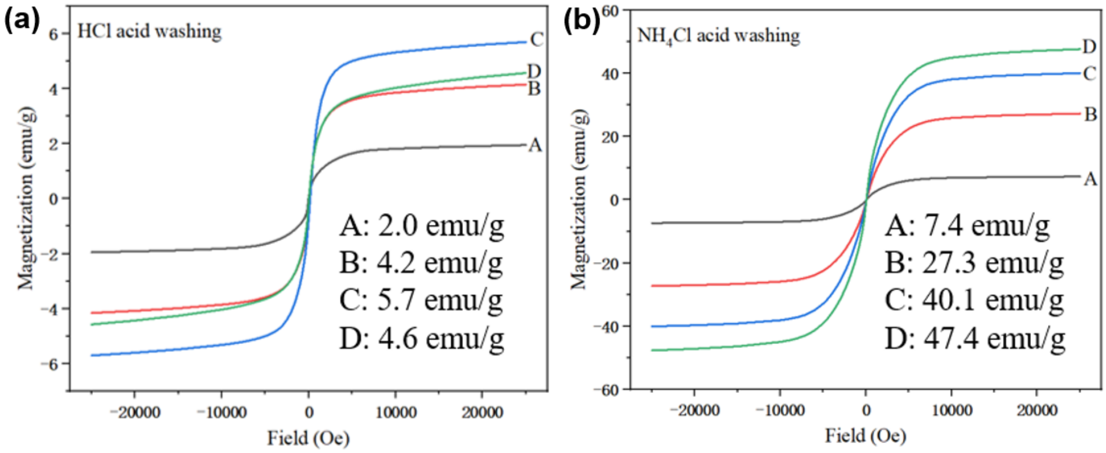

Figure 24 Magnetization curves of fabricated materials. A-D refer to varying feedstock compositions, as described in the text.

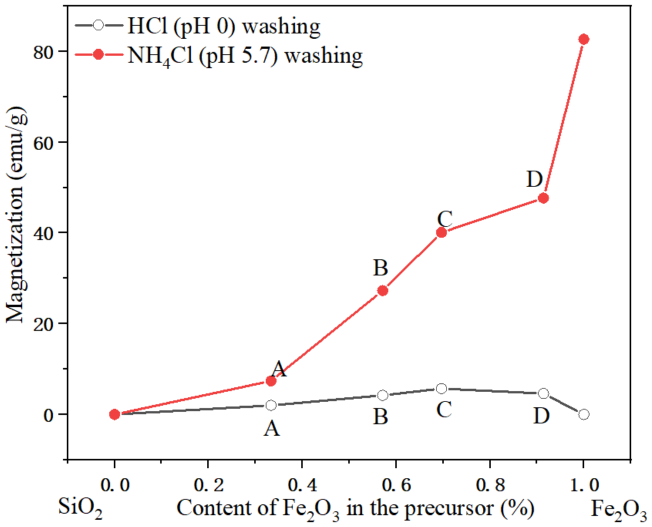

Figure 25 Corresponding saturation magnetizations of fabricated NPs from different precursors at room temperature under 2.5T. A-D refer to varying feedstock compositions, as described in the text.

Therefore, the saturation magnetization of Fe/Si-based nanocomposites could be increased by increasing the amount of zero valent iron (Fe), which can be controlled by increasing the amount of Fe_2O_3 in the precursor of Fe_2O_3/SiO_2. Suitable magnetic properties can help facilitate mobility and target application by an external magnetic field for targeted photothermal therapy and potential drug delivery.

2.3.5 Wettability of fabricated FeSi NPs

0.15g fabricated FeSi NPs was firstly pressed into a tablet by infrared tablet press under the pressure of 10MPa for 10 seconds and then it was tested by contact angle meter. Whilst a drop of water was carefully deposited on the tablet, the camera took many photos every second. The result can be seen as below Figure 26. The contact angle of 26.9° shows that the fabricated FeSi nanoparticles are hydrophilic, which is generally good for biocompatibility. The hydrophilicity of F-FeSi can give some guidance for their surface modification for good solution dispersity.

Figure 26 Contact angle measurement of F-FeSi tablet created via cold pressing.

2.4 Conclusions

Porous silicon (pSi) for comparison is fabricated from tabasheer via magnesiothermic reduction, following other's synthesis method; Fe particles is firstly fabricated from Fe_2O_3 (prepared by heating $Fe(NO_3)_3 \cdot 9H_2O$) via magnesiothermic reduction and NH_4Cl washing; FeSi is firstly fabricated from tabasheer and $Fe(NO_3)_3 \cdot 9H_2O$ via magnesiothermic co-reduction. Fe/Si-based nanoparticles (mainly FeSi and Fe) are controllably fabricated from tabasheer and $Fe(NO_3)_3 \cdot 9H_2O$ via magnesiothermic co-reduction and solution washing via changing the ratio of Fe_2O_3/SiO_2. Some characterizations of materials such as phases, morphologies, pore parameters, magnetization and wettability are investigated by XRD, SEM, TEM/EDS, BET, VSM and contact angle meter.

The fabricated pSi NPs have surface area of 209 m^2/g, pore volume 0.67 m^3/g and average pore diameter 13 nm. The fabricated Fe NPs have structures of flower petals with particle size of 500nm and 83 emu/g saturation magnetization. The fabricated FeSi NPs have sizes around 60 nm, surface area of 90 m^2/g, pore volume 0.21 cm^3/g and average pore diameter around 9.4 nm. They have a weak saturation magnetization of 4.6 emu/g. The fabricated FeSi nanoparticles are hydrophilic with a contact angle of 26.9°.

The basic characterization of the fabricated materials helps me to know the materials and set the foundation is important to understand and optimize their photothermal properties (chapter 3) and application of *in vivo* photothermal performance (chapter 4).

Chapter 3. Photothermal properties of FeSi and Fe/Si-based nanocomposites

3.1 Introduction

Photothermal properties involves interaction of light with materials, photothermal conversion and thermal transfer from particles to surrounding solution. Optical properties are mainly related to light absorption, factors affecting absorption and applications. Photothermal conversion are related to mechanism and applications. Thermal properties are related to melting point, heat conductivity and heat capacity. The above information will be introduced in this chapter. Setup for measurement and introduction of photothermal performance, photothermal conversion efficiency and photothermal stability are also introduced in this chapter.

3.1.1 Interaction of light with particles

Interactions of light with particles include absorption, scattering and transmission. Among them, optical absorption can convert the energy of light into energy of heat, while reflection and scattering can increase the optical path in the surface of porous particles with a size which is larger than the wavelength of light, which may increase the light absorption, especially for particles with superstructure or uneven surface.

Absorbance (denoted as A) is a term of physics and chemistry, which shows the quantity of light absorbed by the solution/substance. Absorbance (A) is calculated by the equation $A = log_{10}\frac{I_0}{I}$, where I_0 is the incident optical intensity, I_r is the reflected optical intensity and I is the transmitted optical intensity, which can be seen below in Figure 27.

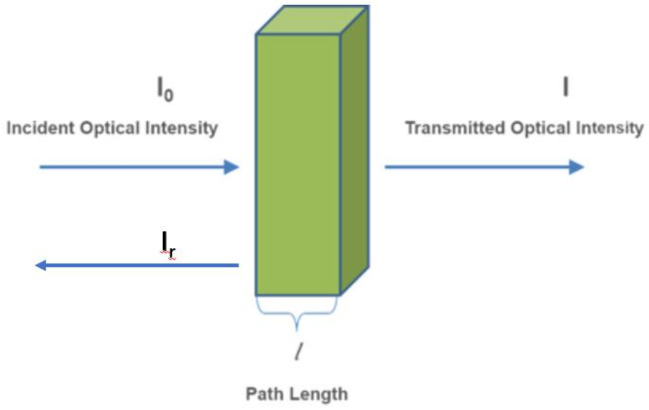

Figure 27 Schematic diagram of light passing through the substance. I_0 is the incident optical intensity, I_r is the reflected optical intensity and I is the transmitted optical intensity.

Absorbance can be measured by UV-vis-NIR spectrophotometer or Fourier transform infrared spectroscopy (FTIR). It is determined by the property of materials when the wavelength, concentration of materials in specific solution and temperature are known.

Extinction coefficient shows the light absorption and scattering ability of the materials, which can be divided into mass/molar extinction coefficient based on the units used. Beer-Lambert Law ($A = \varepsilon * c * l$) can be used for determining the extinction coefficient (ε, in M^{-1} cm^{-1} or L g^{-1} cm^{-1}) of the samples when getting the values of absorbance (A) / extinction (E), concentration (c, in mol/L or g/l) and length (l, in cm).

3.1.2 Photothermal conversion mechanism

3.1.2.1 Noble metal nanoparticles

The photothermal conversion mechanism of noble metals are local surface plasmon resonance (LSPR) [71,72]. Figure 28 is LSPR's schematic diagram [73]. After light absorption, the energy of photons converts to the kinetic energy of electrons. Then the kinetic energy of electrons changes to vibrational energy of crystal lattice by the partial scattering of electrons to crystal lattice.

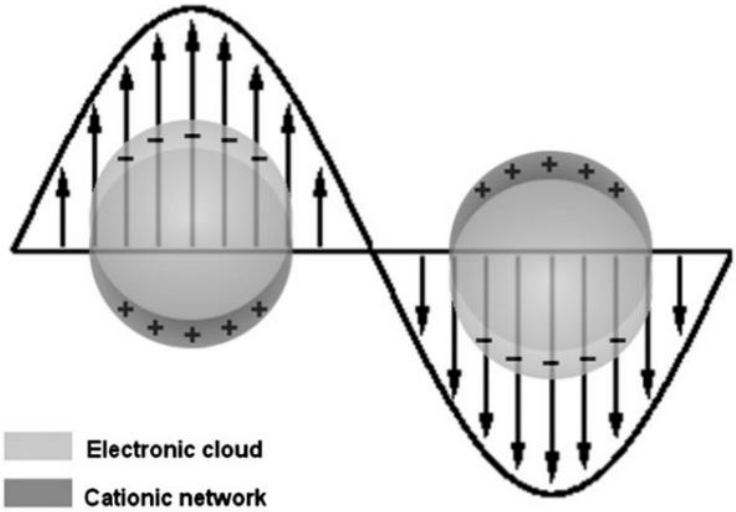

Figure 28 Schematic description of electronic cloud displacements in nanoparticles under effect of an electromagnetic wave. (Moores 2006).

3.1.2.2 Semiconductors

The photothermal conversion mechanism of semiconductors is understood as below. Electrons jump to the conduction band from the valence band after being irradiated by light [74,75]. The heat is generated during the non-radiative relaxation of free electrons and holes from deposited energy to heating of lattice, which can be seen in Figure 29. Therefore, indirect band gap structure is conducive to photothermal conversion for semiconductors compared with direct band gap structure.

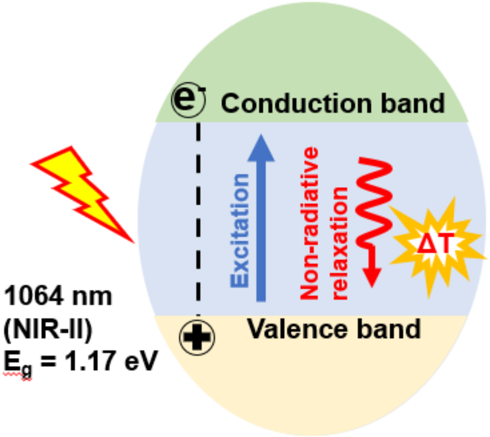

Figure 29 Schematic diagram of photothermal conversion mechanism for semiconductors.

3.1.2.3 Carbon-based materials

The photothermal conversion mechanism of carbon-based materials is conjugation or hyperconjugation effect [76,77]. Materials with π-conjugated structures have unique photothermal effects due to their reduced electronic excitation energy and redshifted absorption wavelength.

3.1.3 Thermal properties

For thermal properties, melting point, thermal conductivity and heat capacity are involved. Heat transfer involves thermal conductivity and heat capacity.

3.1.3.1 Melting point

The melting point of nanoparticles is dependent on size and it decreases with the reduction of particle size [78,79]. The Figure 30 below shows clearly that change is more obvious when the size is less than 10nm. While the melting point doesn't change too much when the size is larger than 10nm. Therefore, for the nanoparticles with more than 10nm, the melting point may be close to that of bulk materials. The melting point of bulk FeSi is 1220℃. So, the photothermal performance of the materials in water (around 80℃), even the powder (200℃), has no effect on the structure change of nanoparticles for the melting.

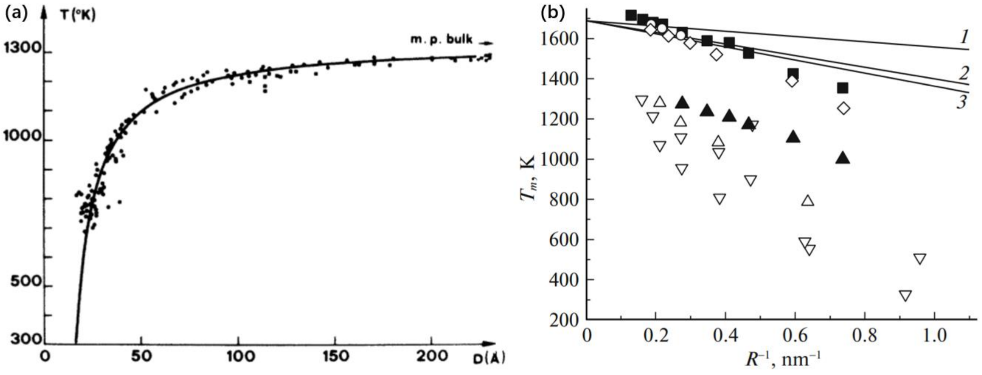

Figure 30 Experimental and theoretical values of melting-point temperature of Au (a) and Si (b). Adapted from (Buffat 1976; Talyzin 2019).

3.1.3.2 Thermal conductivity

Thermal conductivity (α) means material's ability to transfer heat through it by conduction, which is measured in W/m.K. For solids and powders, thermal conductivity is related with their structure and porosity. Thermal conductivity of nanoparticles, state of powder, is also being investigated with the help of some setups and models.

For heat transfer and photothermal performance (photothermal therapy), large value of thermal conductivity of the materials can transfer heat quickly generated by irradiated materials to the ambient aqueous solution. As a result, the temperature of solution can increase quickly for ablating tumours efficiently.

In general, the thermal conductivity of a substance can be obtained theoretically and experimentally. Due to the limited applicability and many new emerging materials, it is difficult to find sufficiently accurate and widely used theoretical equations. Therefore, experimental test methods and techniques are the main source of thermal conductivity. Heat transfer measurement system of integrated physical property measurement system (PPMS) and thermal conductance meter can be used for getting thermal conductivity of materials.

3.1.3.3 Heat capacity

The heat capacity (C) of materials means the quantity of heat needed to change its temperature by one degree, which is measured in J/K. Specific heat capacity means the heat capacity of a substance per unit mass. Specific heat capacity is a kind of specific property of matter, which only relates to states of matter and has nothing to do with the change of its mass and shape.

For heat transfer and photothermal performance (therapy), small value of heat capacity of the materials can transfer more heat generated by irradiated materials to the ambient aqueous solution. As a result, solution can have a higher temperature for ablating tumours efficiently. For other applications based on photothermal conversion, materials with small heat capacity are competitive.

Heat capacity of nanoparticles (state of powder) is also being investigated with the help of some setups and models. Differential scanning calorimetry (DSC) is used for achieving heat capacity of the materials. There are six methods measuring specific heat capacity based on heat flow curve of DSC. They are direct method, steady state ADSC method, sapphire method, stepwise-scanning method, sinusoidal temperature modulated method and multi-frequency temperature modulated method. Among them, sapphire method is a popular and relatively accurate one, which has been used for more than 40 years.

3.1.3.4 Comparisons of α and C of materials

During heat transfer, melting point, thermal conductivity and heat capacity are involved, which are discussed below separately. But few photothermal therapy research groups pay attention to these properties. Coexistence of high α and low C in materials is a very attractive feature as the photothermal agents, which should be in the top left corner in the Figure 31. From the figure we can know that noble metals and Fe have high α and C, porous silicon (PS) and oxidized porous silicon nanoparticles have low α and C and that carbon-based materials have low α and middle C. The fabricated FeSi is assumed to have higher α than porous silicon and lower C than Fe, which needs to be investigated in the future.

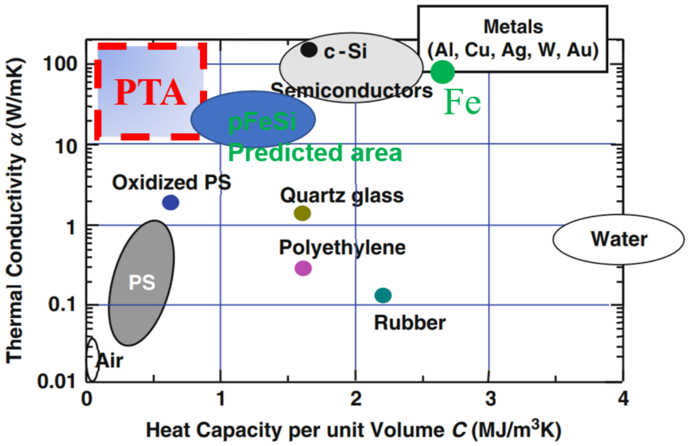

Figure 31 Data of thermal conductivity, heat capacity of materials. Adapted from (Canham 2014).

3.1.4 Photothermal performance

Photothermal performance is showed by the temperature change with time (usually 5-10mins, here 10min) of the solution containing different concentrations of nanoparticles irradiated by different power densities of laser with different wavelengths (808nm, 980nm, 1064nm, here 1064nm is used). Thermocouple or infrared thermometer is used for giving the local temperature of solution. Quartz cuvette or culture dish is used for storing certain volume of solutions (here 200μL is used). Two examples [80,81] of schematic diagram and digital photo show the setup for measurement of the photothermal performance of the materials, which can be seen in Figure 32. For the setup, quartz cuvette with 1 cm path length contains 2 mL solution, a thermocouple connected to a digital thermometer and a laser are needed. Stirring is needed for the temperature uniformity of the solution. The diagram and optical image of setup used for the project can be seen in Figure 33.

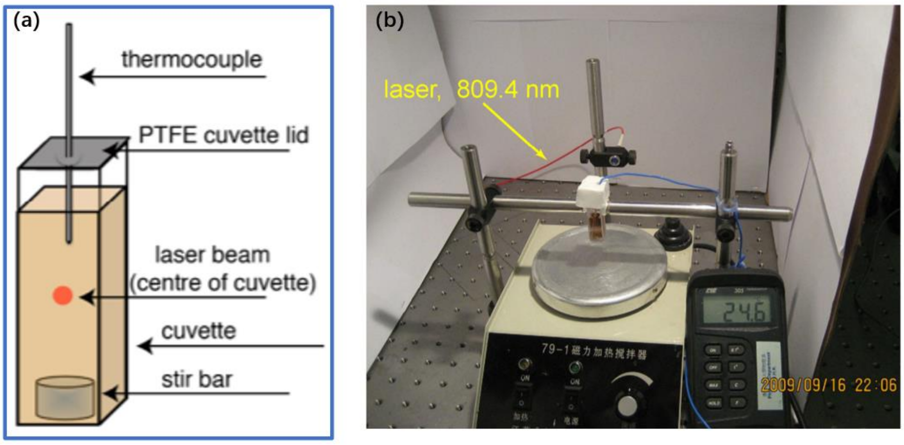

Figure 32 Schematic diagram of setup for characterizing photothermal performance of solutions containing materials. Adapted from (Regli 2012; Chen 2010).

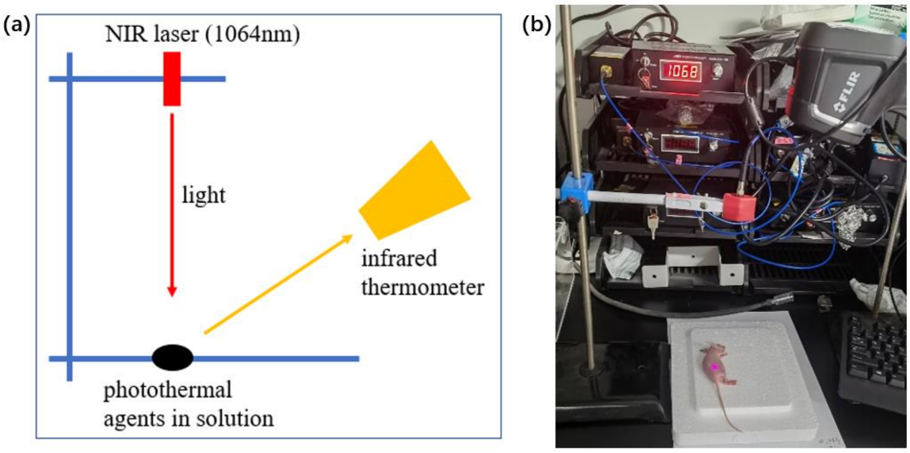

Figure 33 Optical image of setup used for photothermal performance of materials (a) and photothermal therapy of mouse (b) in Department of Biomedical Engineering, Southern University of Science and Technology (SUSTech).

Multimode optical fiber coupled laser diode (1060±5 nm, 1000 mW) is used as light source. Intensity (1 W/cm^2 is used in the thesis) of laser can be determined by the power of laser and the size of light spot. The power of laser can be determined by setting specific current, the relation between them can be seen in Figure 34. Calibration was checked by the technician of the company. The distance between laser head and sample can determine the size of light spot. The spot diameter of the collimator is 5 mm. The spot diameter increases by about 1.8 mm when the distance increased by 100mm. Therefore, the equation of size of light spot can be expressed as $y = 1.8*x/100 + 5$, where y (mm) is the size of light spot and x (mm) is the distance. Culture dish is used to storing 200 μL solutions. Temperature is measured by infrared thermometer (FLIR E6). The time set for measurement is 10 min.

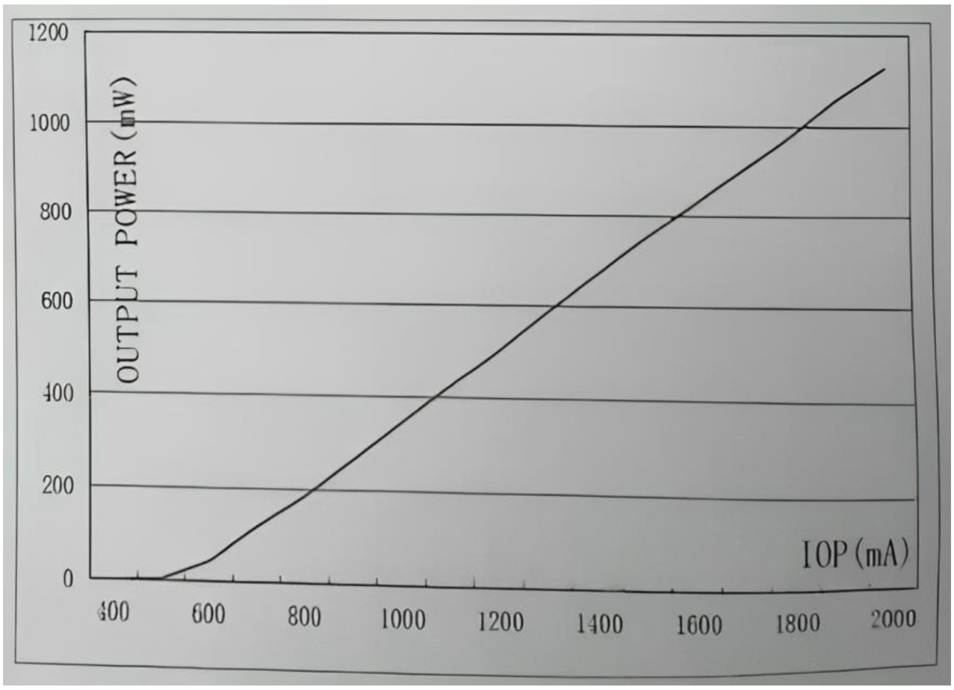

Figure 34 Dependence of output power of 1064nm laser with applied current.

3.1.5 Photothermal conversion efficiency (η) and calculation

For the measurement of photothermal performance, research groups usually choose different setups, quantities of solution, concentrations of nanoparticles, wavelength/power densities of laser, times, thermometer. Therefore, it is difficult to compare the photothermal performance of the materials of different groups. Photothermal conversion efficiency is a physical value which can be used to compare the photothermal performance of different photothermal agents. Photothermal conversion efficiency (η) shows the ability of conversion from optical energy to heat energy.

Photothermal conversion efficiency can be divided into narrow one and broad one, which can be seen in Figure 35. For strict one, it only shows the process of photothermal conversion. For broad one, it shows all processes of photothermal performance, including the optical absorption, photothermal conversion and heat transfer.

Photothermal conversion efficiency calculated by almost all the research groups using different models is the broad η, showing the whole process from the laser energy to the final temperature increase of the solution. These three stages all affect the photothermal conversion efficiency. Therefore, there are some strategies for increasing the broad η, such as adjusting the absorption peak to laser wavelength, using superstructure to improve the laser absorption, lower the band gap, reducing heat capacity and increasing thermal conductivity.

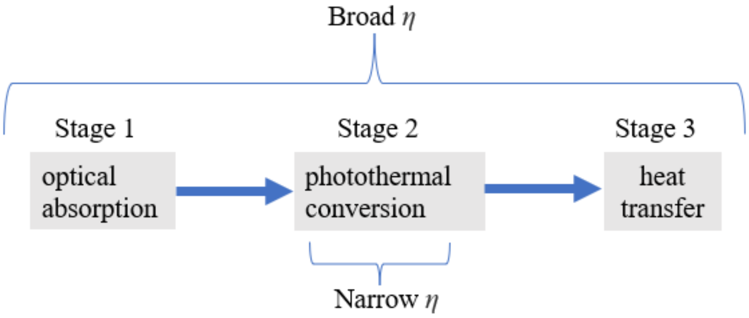

Figure 35 Schematic diagram of broad and narrow photothermal conversion efficiency.

There are two popular models for calculating η based on cooling curve. For the one of Roper [82], η can be calculated as below. Many research groups choose this model, including this thesis.

$$\eta = \frac{hs(T_{max} - T_{max,water})}{I(1 - 10^{-A_{1064}})} \quad (3\text{-}1)$$

$$hs = \frac{mC_p}{\tau_s} \quad (3\text{-}2)$$

$$\tau_s = -\frac{t}{ln\,(\theta)} \quad (3\text{-}3)$$

$$\theta = \frac{T_{amb} - T}{T_{amb} - T_{max}} \quad (3\text{-}4)$$

where h is heat transfer coefficient, s is the surface area of the container, T_{max} is the equilibrium temperature of the sample solution after laser heating, $T_{max,water}$ is the equilibrium temperature of pure water under laser heating, T_{amb} is the ambient temperature, T is the real-time temperature of solution with time, I is the laser power, A_{1064} is the absorbance of the sample at 1064 nm, m is the mass of solution, C_p is specific heat capacity of solution, θ is dimensionless driving force temperature, τ_s is sample system time constant.

For the one of Jianfang Wang [80], η can be calculated as below.

$$\eta = \frac{B(T_{end}-T_0)+C(T_{end}-T)^2-I\xi}{I(1-\xi)(1-10^{-\varepsilon}\lambda)} \quad (3\text{-}5)$$

where B and C are two coefficients, which are determined by switching off the laser when the temperature reached the plateau, T_0 is the starting solution temperature, T_{end} is the highest temperature of solution with time, T is the starting solution temperature, I is the laser power, ε_λ is the extinction value at the illumination laser wavelength, ξ was determined from the end temperature.

3.1.6 Photothermal stability

Photothermal stability of photothermal agents is an important factor for photothermal therapy, especially for some multiple photothermal therapy. It is usually characterized by the photothermal performance of materials in the solution after several cycles (laser on and off). For some materials with low melting point, the high temperature will melt. For some materials, the structure will be damaged with high temperature.

3.2 Experimental

3.2.1 Materials

In this chapter, materials of FeSi NPs, pSi NPs, Fe NPs and physical mixture of Fe NPs and pSi NPs at the atom ratio of 1:1 are used. All materials were synthesized using magnesiothermic reduction method from their respective oxides. Commercial FeSi (C-FeSi) particles were bought from Jiuding Chemical (Shanghai, China) and used as a control for comparison.

3.2.2 Characterization techniques

UV-Vis-NIR Spectroscopy (UV-Vis-NIR) was used to obtain absorption spectrum in the ultraviolet (UV), visible (Vis) and near infrared (NIR) ranges, while Fourier transform infrared spectroscopy (FTIR) was used to obtain absorption spectrum in the infrared (IR) ranges. The detailed introduction of these techniques can be seen in below Table 4.

Details	*UV-Vis-NIR*	*FTIR*
Fundamental principles	Lambert-beer law, $A=-\log(I/I_0)=\epsilon*L*c$	Fourier transform of interference pattern
Instrumentation	Radiation source, monochromator, sample container, detector	IR source, sample compartment, detector
Applications	Food, farm products, cosmetics, fodder, chemistry	Chemical/physical/ biological/pharmacal fields
Strengths	Good repeatability, concentration dependent, easy/rapid test	Frequencies measured simultaneously, more sensitive, higher signal to noise ratio

Limitations	Effect of solution absorption, spectrum range 200–3300nm	Cannot detect atoms/molecules comprised of two identical atoms/complex mixtures/water
Sample collection, preparation	Aqueous solution at certain concentration	Pure solid/liquid/gas (>98%) without water, transmittance (10%~80%)
Data collection, results, presentation	Absorbance vs wavelength at certain concentration(s)	Intensity vs frequency
Equipment used	Lambda 750s UV-vis-NIR spectrophotometer	Bruker Vertex 70v

Table 4 Detailed introduction of the techniques used for different characterisations.

3.3 Results and discussion

3.3.1 Optical properties of materials

To investigate the absorbance and mass extinction coefficient of the FeSi NPs in water, three concentrations (10, 50 and 100 ug/mL) of FeSi NPs in water were prepared, which were tested by UV-Vis-NIR Spectroscopy. As shown in Figure 36 below, the FeSi NPs exhibited a strong and broad absorption band in the visible and NIR region (400-1200 nm). The open circles indicate the large fluctuation of absorption spectrum at around 856 nm, which arises from the change of optical grating during the measurement. The results in the inset of Figure 36 also show a linear dependence of the absorption on FeSi concentration, which is corresponded with the lambert-beer law. The extinction coefficient of FeSi suspension was measured from the slope of the linear plot to be 13.3 L g^{-1} cm^{-1} at 1064 nm, which was comparable to that of FeS (15.5 L g^{-1} cm^{-1}) [23] and black phosphorus quantum dots (14.8 L g^{-1} cm^{-1}) [83] and higher than that of graphdiyne (10.1 L g^{-1} cm^{-1}) [84], graphene oxide (5.94 L g^{-1} cm^{-1}) [85], Ta_4C_3 (4.06 L g^{-1} cm^{-1}) [86] and black phosphorus (2.1 L g^{-1} cm^{-1}) [87].

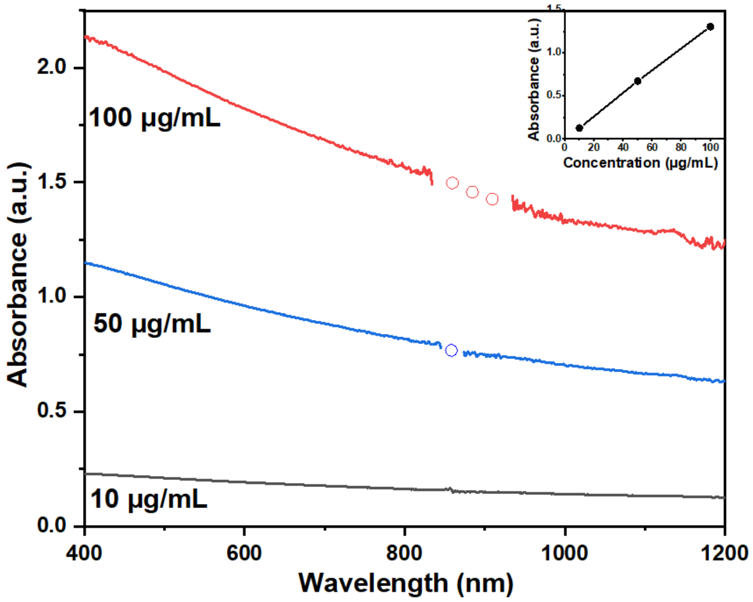

Figure 36 UV-vis-NIR absorbance spectra of F-FeSi NPs aqueous suspensions of different particle concentrations, with the inset showing a linear relationship between the absorbance of FeSi NP suspensions at 1064 nm and particle concentration.

3.3.2 Photothermal conversion effect

Photothermal conversion mechanism of semiconductors can be understood as below. Electron jumps to conduction band from valence band after being irradiated by laser. The heat is generated during the non-radiative relaxation of free electrons and holes. For laser with NIR-II wavelength (1064 nm), the ideal band gap of the materials to best absorb the light and convert its optical energy to the heat should be below 1.17 eV as calculated. In order to investigate the band gap of FeSi NPs, UV-Vis-NIR Spectroscopy and FTIR spectra were used for finding the absorption peak. There is no obvious absorption peak in the visible and NIR region (400-1200 nm) of UV-Vis-NIR Spectroscopy in above Figure 36. The Fourier transform infrared reflectance spectra in Figure 37 shows an absorption threshold of 9.68 μm for our FeSi NPs, which corresponds to a band gap of 0.128 eV as calculated using E_g (eV) = hν. Similar value of 0.13 eV was reported in literature [61,62]. The results suggest that the laser of 1064 nm wavelength can be effectively absorbed by the FeSi NPs.

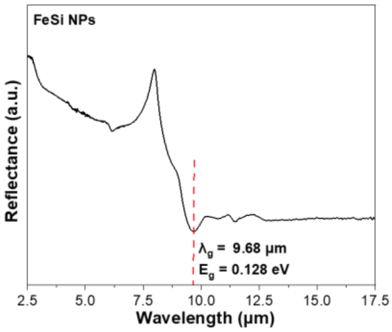

Figure 37 Narrow FTIR spectrum from 2.5 μm to 17.5 μm and the corresponding absorption threshold of fabricated FeSi NPs.

3.3.3 Photothermal performance

Photothermal performance is characterized by the temperature variation of aqueous suspensions containing different materials at some concentrations under irradiation of a 1064 nm laser at different laser power densities for 10 min.

3.3.3.1 Photothermal heating of colloidal FeSi NPs dispersions and the comparison of it with other materials

The local temperature was around 26 ℃. The aqueous suspension (200 uL) containing 0.5 mg/mL fabricated FeSi NPs under irradiation by a 1064 nm laser at 1 W cm^{-2} can be heated to 80 ℃ within 10 min. At the given solid concentration of 0.5 mg/mL, the FeSi NPs showed a much better photothermal performance than porous pSi and Fe NPs both synthesized using magnesiothermic reduction method from their respective oxides as shown in Figure 38. It also shows a much better photothermal performance of FeSi than that of the physical mixture of Fe NPs and pSi NPs at the same Si/Fe ratio as in FeSi NPs. From Figure 38b, we can see that fabricated FeSi has a better photothermal performance than commercial FeSi. As anticipated, the FeSi NPs synthesized in this study had desirable photothermal properties under 1064 nm NIR laser irradiation. The superior photothermal performance of the FeSi NPs synthesized in this study is attributed to their much narrower band gap, low density and large specific surface area of mesoporous structure.

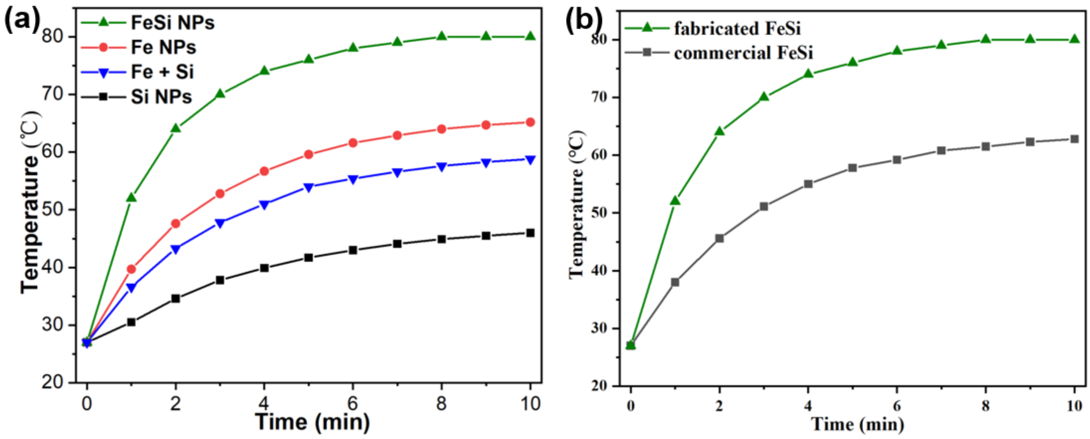

Figure 38 Temperature variation of aqueous suspensions (200 uL) containing different materials at the same concentration of 0.5 mg/mL under irradiation of a 1064 nm laser at 1 W cm^{-2} for 10 min.

3.3.3.2 Photothermal performance of Fe/Si-based nanocomposites

For the photothermal performance of Fe/Si-based nanocomposites, fabricated from tabasheer and $Fe(NO_3)_3$•$9H_2O$ via magnesiothermic reduction, have also been investigated. For HCl washing, with the increase of the content of Fe_2O_3 in the precursor, the photothermal performance of the nanocomposites becomes better under the same testing conditions, that is because of the better photothermal performance of FeSi than that of $FeSi_2$ and Si. When precursor is only Fe_2O_3, no product will be achieved after HCl washing. While for NH_4Cl washing, with the increase of the content of Fe_2O_3 in the precursor, the photothermal performance of the nanocomposites firstly becomes better and then decreases under the same testing conditions, that is due to the better photothermal performance of FeSi than that of Fe. And probably the phase of FeSi firstly increase of the final composites and then Fe content increase. When precursor is only Fe_2O_3, the final product is Fe after NH_4Cl washing. Therefore, the phase of Fe can help increase the saturation magnetization of the nanocomposites, but it has a bad effect on the photothermal performance.

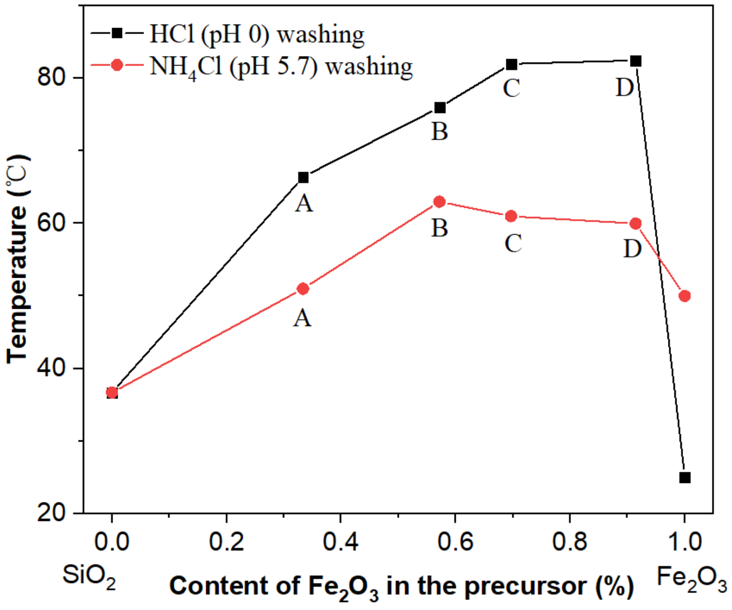

Figure 39 Photothermal performance of the Fe/Si-based nanocomposites after HCl and NH_4Cl washing. A-D refer to varying feedstock compositions, as described in the text of chapter 2 and properties illustrated in figures 23-25.

3.3.3.3 Material concentration and laser power density dependent photothermal performance

It is known that photothermal performance is affected by the concentration of materials and laser power density. In order to investigate it, the temperature changes of FeSi NPs aqueous suspension containing different amounts of NPs (10 to 500 μg mL^{-1}) under 1064 nm laser radiation of different power densities (0.4 to 1.2 W cm^{-2}, 10 min) were monitored. It is interesting to see in Figure 40 that photothermal performance become better with the increase of the concentration of FeSi NPs and laser power densities. Such findings allow us to fine-tune the heating rate and final temperature as desired by changing either FeSi NPs concentration or applying different laser powers in practical applications.

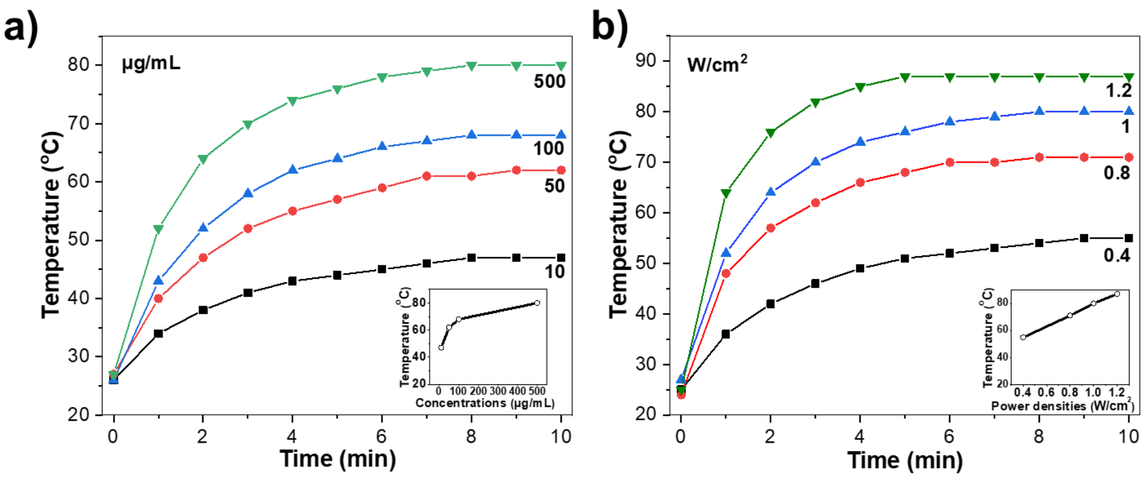

Figure 40 a) Temperature change of FeSi NPs aqueous suspension with particle concentration under 1064 nm laser irradiation at 1 W cm^{-2} *for 10 min, with the inset showing a linear relationship between plateau temperature and particle concentration; b) Temperature change of 0.5 mg/mL FeSi NPs aqueous suspension under irradiation of 1064 nm laser at different power densities for 10 min, the inset showing a linear relationship between plateau temperature and laser power density. All the measurement used 200 uL of FeSi NPs aqueous suspensions.*

3.3.4 Photothermal conversion efficiency (η)

The photothermal conversion efficiency of FeSi NPs was calculated using the data from the heating and cooling profile based on the cooling profile using the method proposed by Roper and co-workers [82]. The cooling profile of 200 uL FeSi NP aqueous suspensions (0.5 mg/mL) irradiated by a 1064 nm laser at 1 W cm^{-2} and natural cooling with laser off at 10 min is shown in Figure 41 (a). The η value of FeSi NPs was calculated using above equations (3-1, 3-2, 3-3 and 3-4) with parameters derived from the Figure 41 (b) to be approximately 76.2%. This value is much higher than the values for some current photothermal agents, such as $SiO_{0.92}$ (48.6%) [13], black phosphorus (36.8%) [87], Bi_2S_3 (28.1%) [88], black phosphorus quantum dots (24.8%) [89] and Fe/Fe_3O_4 (20.3%) [90].

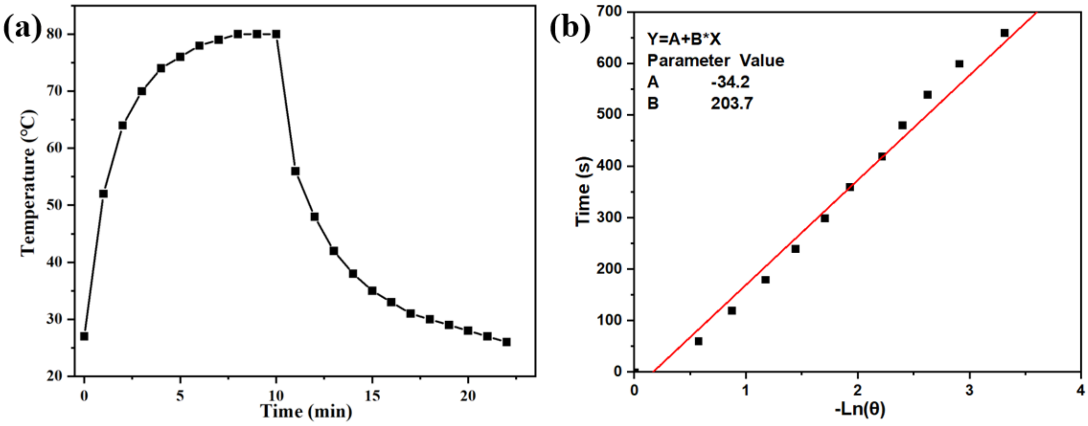

Figure 41 (a) Temperature profile of 0.5 mg/mL FeSi NPs aqueous suspension (200 uL) irradiated by a 1064 nm laser at 1 W cm^{-2}, followed by natural cooling with the laser off, and (b) the time constant for heat transfer calculated using a linear regression of the cooling profile.

The calculation process is as follows. 200 μL aqueous dispersion of materials was used in the test, so m is 0.2 g; Cp of H_2O is 4.2 J/(g·°C); τ_s is 203.7 s from Figure 41; A_{1064} is 0.9354 when the concentration is 0.5 mg/mL; laser power (I) is 320 mW for 96-well plates with surface area of 0.32 cm^2 when the laser power density is 1 W/cm^2; T_{max} is 80 ℃; $T_{max,water}$ is 27.7 ℃.

$$\eta = \frac{\hbar s(T_{max} - T_{max,water})}{I(1 - 10^{-A_{1064}})} = \frac{0.2g \bullet (4.2J/g \bullet ℃) \bullet (80\ -\ 27.7)\,℃}{203.7s \bullet 320mW(1 - 10^{-0.9354})} = 76.2\%$$

3.3.5 Photothermal stability

As an important factor for photothermal therapy, the photothermal stability of FeSi NPs suspensions was evaluated through five cycles of heating and cooling. Temperature variations of 0.1 mg/mL FeSi NP aqueous suspensions were recorded over 5 cycles of heating at 1 W cm^{-2} and natural cooling. The results in Figure 42 show a similar level of photothermal performance of FeSi NPs after five cycles of NIR laser-induced heating (1064 nm laser at 1 W cm^{-2}, 10 min laser irradiation for each cycle) and natural cooling, demonstrating the excellent photothermal stability of FeSi NPs. The small increase of the temperature with cycles is caused by the evaporation of water due to the high temperature of the solution after laser irradiation.

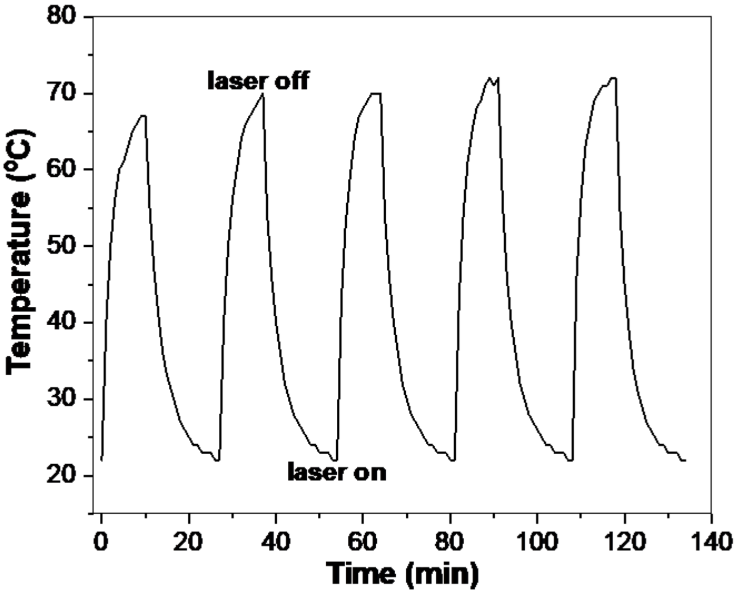

Figure 42 Temperature variation of 0.1 mg/mL FeSi NPs aqueous suspensions (200 uL) over 5 cycles of heating at 1 W cm^{-2} and natural cooling.

3.4 Conclusions

Mass extinction coefficient of FeSi suspension was 13.3 L g^{-1} cm^{-1} at 1064 nm. The narrow band gap (0.128 eV) of FeSi was confirmed by the fabricated sample. FeSi NPs have better photothermal performance compared to pSi and Fe NPs. Photothermal performance can be improved by increasing the concentration of FeSi NPs or laser power densities. The η of FeSi NPs was calculated to be approximately 76.2%, which is a high value compared many photothermal agents. The photothermal stability of FeSi NPs suspensions was confirmed good through five cycles of heating and cooling.

The good photothermal performance, high photothermal conversion efficiency and good photostability of FeSi NPs make them an encouraging photothermal agent for photothermal cancer therapy. The *in vivo* photothermal therapy of FeSi nanoparticles will be discussed in chapter 4.

Chapter 4. *In vivo* photothermal therapy of FeSi nanoparticles

4.1 Introduction

As we all know, cancer [91] cause much pain to patients. There are many methods for cancer treatment. The most three popular treatments used for cancer therapy are surgery, chemotherapy and radiotherapy. However, they all have some limitations. For example, surgery brings infection-related complications, chemotherapy brings toxicity to the body and resistance of cancer cells to particular drugs, radiotherapy brings side effects like damage to healthy cells and fatigue. With the development of the technology, some new cancer treatments emerge. They are gene therapy, immunotherapy, gas therapy, percutaneous ethanol injection (PEI), photodynamic therapy (PDT), sonodynamic therapy (SDT) and thermal therapy. For thermal therapy, there are several heat sources, which are focused ultrasound, radiofrequency, microwave, alternating magnetic field and NIR light. Among the thermal therapy, magnetic hyperthermia therapy (MHT) and photothermal therapy (PTT) with PTAs both have been extensively investigated. MHT needs engineered coils for encompassing the desired area, so there is large air volume within the applied field with poor specificity. Compared with MHT, PTT is relatively simple, which only involves NIR light and photothermal agents. The therapeutic process can be seen in Figure 43 below [21]. Photothermal agents are firstly delivered to the tumour site and then exposed to near-infrared (NIR) light. The laser energy can be converted to thermal energy with the help of the PTAs. As a result, the higher temperature (40-45℃) with around 10 minutes can kill cancer cells due to their sensitivity to heat with poor blood supply compared with normal cells [92]. For photothermal therapy with NIR light, some use photothermal agents (PTAs) and some use minimally invasive operation without PTAs.

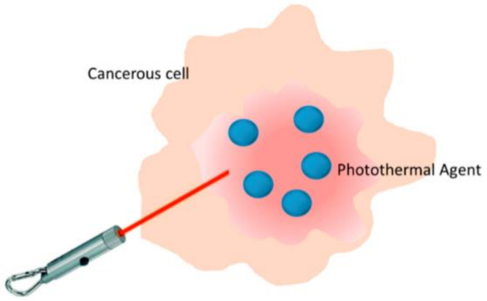

Figure 43 Basis of the photothermal therapy. Adapted from (Estelrich 2018).

The advantage/disadvantage, wavelength choice of laser used, pattern of injection, requirement/comparison of photothermal agents, clinical progress of photothermal therapy are discussed below.

4.1.1 Advantage/disadvantage and positioning of PTT

Phototherapy (PTT) has gained a considerable attention in cancer therapy due to many reasons, which are listed below.

1. It is a minimally invasive approach with only localized heating, which avoids the systematic side effects.

2. It is a kind of physical treatment, which is a “universal” treatment for many types of cancer.

However, there are also some limitations, which are listed below.

1. Photothermal therapy is suitable for the preliminary and medium-term cancers. The advanced metastatic cancers are difficult to be efficiently killed because they are difficult to be located, although targeting function can be added into the photothermal agents.

2. The deeper cancers in body are difficult to be efficiently killed due to low light-penetration depth for tissue window.

3. In order to get a good result of therapy, high dose of photothermal agents, high laser power and longer time are sometimes needed when the photothermal performance of PTAs is not good, which may damage normal tissues.

4. No clear long-term biological behaviour of PTAs in the body limits their clinical application.

In general, as a new cancer treatment, PTT is still in the pre-clinical stage. Although PTT can achieve good result of treatment, it always combines with other therapy such as magnetic hyperthermia treatment (MHT) [26,93,94], chemotherapy [95–97], photodynamics therapy (PDT) [98–100] and immunotherapy [101–103] to achieve a complete treatment. It is also used as a supplement for surgery and radiotherapy to enhance the therapeutic outcome.

4.1.2 Choice of light wavelength in PTT

For energy source, laser is usually used with several wavelengths (808nm, 980nm and 1064nm). Near-infrared light (700-2500 nm) can penetrate biological tissues such as skin and blood more efficiently compared with visible light due to less light scattered and absorbed by the tissue. It can be seen from the Figure 44 that effective attenuation coefficient of body (oxygenated whole blood, deoxygenated whole blood, skin and fat) is the lowest in both of first and second NIR window [104,105].

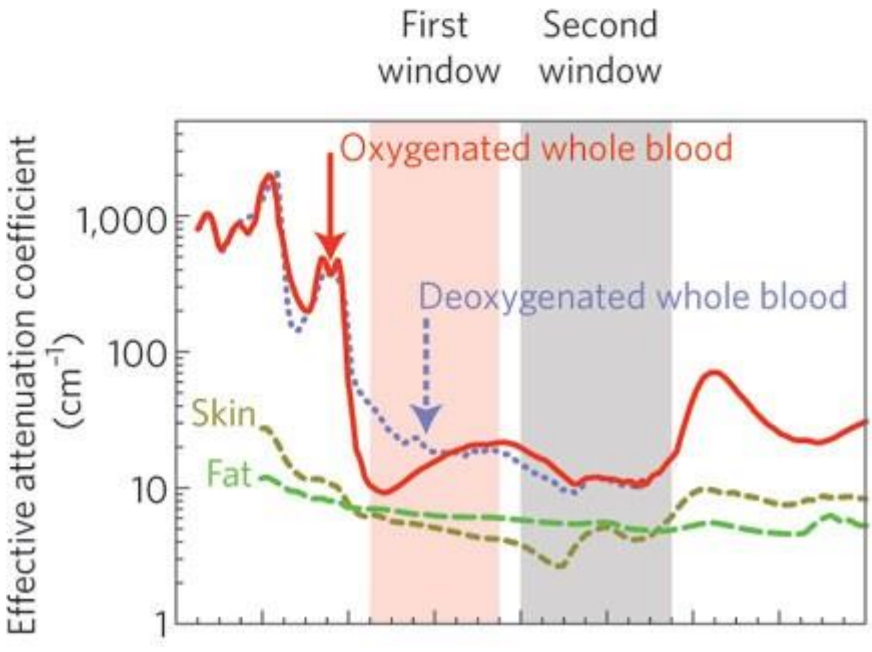

Figure 44 Optical windows in biological tissues. Adapted from (Smith 2009).

There are some differences between NIR-I and NIR-II window. For NIR-I window, the wavelength is 700-950 nm with a small light penetration depth of body, which is suitable for treatment of skin cancer. For NIR-II window, the wavelength is 1000-1350 nm, light penetration depth of body is much deeper due to less tissue absorption and scattering compared with NIR-I window, which can be used for treatment of deeper cancers of human body. Therefore, there are some advantages of working in NIR-II window. First one is that NIR-II window allows larger light penetration depth. The second is that it allows higher maximum permissible exposure to body and be less harmful to normal cells and tissues due to its larger wavelength and less energy provided. The safe limit for skin is as follows: 0.33 W/cm^2 for 808 nm laser, 0.73 W/cm^2 for 980 nm laser and 1 W/cm^2 for 1064 nm laser [106].

4.1.3 Introduction of injection pattern for PTT

There are two methods, intravenous injection and intratumoral injection, to delivery PTAs to tumours. The Figure 45 below shows clearly the patterns of injection [107]. Intravenous injection is a popular method, especially for delocalized cancers, delivering PTAs to tumours based on enhanced permeability and retention effect (EPR effect), but the delivery efficiency is not good. Average of only 0.7% of nanoparticles are delivered into tumours [108]. Therefore, large dosage is needed for desired therapy result. Some research group can increase the delivery rate to 97% with active targeting function such as magnetic and antibody conjugation. For intratumoral injection, the cancers should be localized for injection, the advantage is that the dosage of PTAs can be small. It is suitable for some PTAs with poor dispersity in solutions or PTAs in hydrogel.

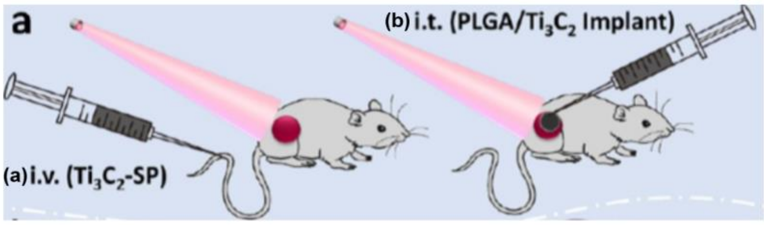

Figure 45 Schematic diagram of (a) intravenous injection and (b) intratumoral injection of materials. Adapted from (Lin 2017).

4.1.4 Photothermal materials

During the past 20 years, many photothermal agents have been developed for photothermal cancer treatment. They can be mainly divided into three kinds, noble metals, semiconductors and carbon-based PTAs. The agents are usually used in solutions, while some are also used in pattern of hydrogel [109–111]. For noble metals, Au, Ag, Pd and Pt nanoparticles are usually investigated, which can be seen in red box of Figure 46 (periodic table of the elements [112]). The mechanism of photothermal conversion for noble metals is based on the localized surface plasmon resonance effect (LSPR). For semiconductors, they are mainly the Si, P, oxide, carbide, sulfide, nitride, silicide (in black box) of transition metal (in blue box) (ME, M=metal, E=O, S, Se, Te, N, C, Si…), which is based on the electron/hole generation and recombination. For carbon-based PTAs, carbon spheres, carbon nanotubes, graphene oxides, dyes, conjugated polymer (cyanines, squarines, phtalocyanines, porphyrin derivatives have been reported. The mechanism of their photothermal conversion is based on the conjugation or hyperconjugation effect.

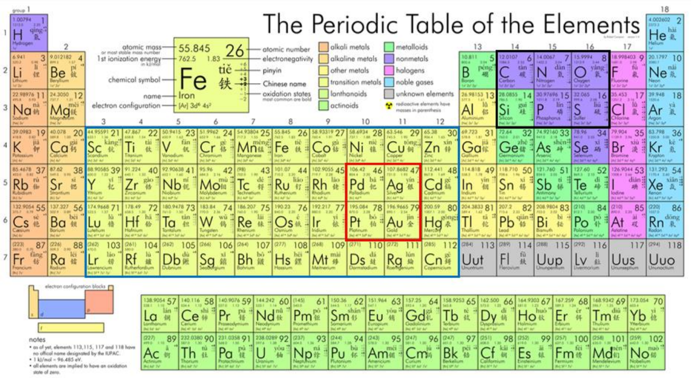

Figure 46 Elements are in red and black boxes on the periodic table that contribute to photothermal agents. Adapted from (https://zh.wikibooks.org/wiki/%E5%85%83%E7%B4%A0%E5%91%A8%E6%9C%9F%E8%A1%A8).

Photothermal agents can also be divided into organic and inorganic agents, which has been included in Figure 47. Inorganic agents include noble metal NPs, semiconductors and some carbon-based materials.

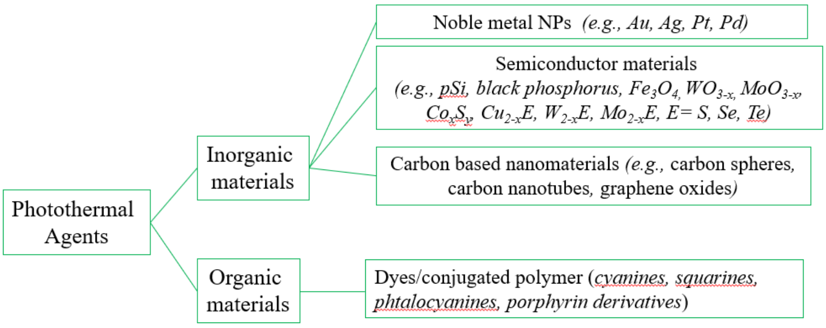

Figure 47 Common PTAs reported during the past 20 years.

Based on the classification of the structures, two-dimensional (2D) materials for PTT such as metal Pd, black phosphorus, WS_2, MoS_2, TiS_2, Bi_2Se_3, Mxene, graphene, graphdiyne have been reported. These years, PTAs in hydrogel instead of solutions have also been investigated.

The photothermal agents reported up to date suffer from several limitations, such as low efficiency in delivering due to enhanced permeability and retention effect (EPR), poor photothermal efficiency, nonbiodegradable nature and unclear long-term biological behaviour, which limit their clinical use. Therefore, there are some requirements needed to be considered for photothermal agents, which are listed below.

A. NIR-II window with large light penetration depth for deeper cancer treatment

B. good photothermal performance for effectively kill of cancer cells (large extinction coefficient, photothermal conversion efficiency, agent concentration, laser power density, thermal conductivity and small heat capacity)

C. agents easy to be accumulated in tumour (suitable particle size, magnetic or other design for targeting tumours) for desired therapy result
D. imaging of PTAs (imaging for knowing when to get highest concentration after injection) for desired therapy result
E. good photothermal stability
F. biocompatible and biodegradable
G. multifunctional agents for multifunctional therapy or combination with other therapy
H. low cost

A and B have been discussed in above chapters. C to H will be discussed below.

4.1.4.1 Particle size for PTT

Particle size is a very important factor of agent for photothermal therapy. For intravenous injection, nanoparticles with suitable size can be effectively delivered to the cancer site. Figure 48 is an example showing the importance of particle size of Au NPs for photothermal therapy (PTT) [113]. Smaller size (<5 nm) enables the Au NPs pass through blood brain barrier (BBB, 20 nm) and to be cleared from kidney. Small particles are more toxic than larger particles. Nanoparticles are accumulated in liver and spleen. For other PTAs, the similar suitable size is also needed. For larger sizes of PTAs, such as microparticles or hydrogel, intratumor injection rather than intravenous injection needs to be considered.

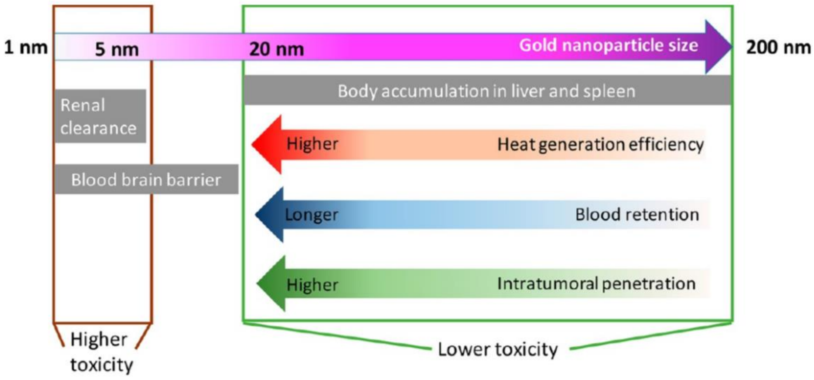

Figure 48 Sizes of the Au NPs in PTT affect their biological behaviours. Adapted from (Ali 2019).

4.1.4.2 Targeting by magnetic property or other design

As discussed above, only 0.7% of nanoparticles are delivered to tumours. In order to get a good result of therapy, targeting needs to be considered to deliver more PTAs to tumours when intravenous injection is used. As a result, for good targeting, the overall dosage of agents and laser power density can be reduced for the same result of therapy. The concentration of agents in other site will be reduced, which will cause less side effects. Lower laser power density can be much safer for patients. And note that, targeting will not be needed if intratumoral injection is used.

There are two strategies for targeting, one is magnetic targeting [114–116], another is using some materials to target specific antigen or receptor on the surface of cancer cells. Some research group can increase the delivery rate to 97% with active targeting function such as magnetic and antibody conjugation. For intratumoral injection, the cancers should be localized for injection, the advantage is that the dosage of PTAs can be small. It is suitable for some PTAs with poor dispersity in solutions or PTAs in hydrogel.

4.1.4.3 Imaging during PTT

Imaging is a very important function for photothermal therapy with intravenous injection. With the help of the imaging, it is easy to know when the concentration of agents in tumour site is the highest for irradiation of laser after intravenous injection. As a result, the suitable time can be decided for therapy. There are many kinds of imaging. They are magnetic resonance imaging (MRI), photoacoustic (PA), fluorescence, computed tomography (CT) and thermal imaging. And note that, imaging will not be needed if intratumoral injection is used.

There are many reports about imaging-guided photothermal therapy. Some choose single-imaging-guided photothermal therapy, like Fe_3O_4@hybrid@Au core/shell nanocomposite (MRI) [117], Fe_3O_4@Au core/shell nano-stars (MRI) [118], while some choose multi-imaging-guided photothermal therapy, like Au-Fe_2C NPs (MRI/photoacoustic tomography/computed tomography) [119].

4.1.4.4 Multifunctional agents for multifunctional therapy or combination with other therapy

Some agents have porous structure or large specific surface area, which can be used for drug delivery. Therefore, these agents can be used for chemo-photothermal therapy, like Au nano-sponge [120], Au hollow nanospheres [121–123], Au nanocages [124–127], Au-coated porous silicon [128] and so on. There are also many reported agents used for photodynamic-photothermal therapy, magnetic hyperthermia-photothermal therapy and immunotherapy/PTT. PTT is also used as a supplement for surgery and radiotherapy to enhance a complete therapeutic outcome.

4.1.4.5 Biocompatible and biodegradable properties

Biocompatibility is an important property of materials for biomedical application. Prior to their use in body of human, materials should undergo cell test and animal test for determining their safety issues. Surface modification is usually used for improving the biocompatibility of the nanomaterials.

Biodegradability and long-term toxicity are the main concerns which limits the clinical adoption of photothermal therapy. Biodegradable PTAs are relatively better than nonbiodegradable PTAs. Suitable biodegradable speed is very important, too quick or too slow are both not good. Good biodegradability means that the nanoparticles can degrade with a suitable speed in the body [129]. This part is mainly discussed in chapter 5.

4.1.4.6 Cost of PTAs

The cost of the PTAs is important for the final application of PTT. Although the dosage of PTAs used for PTT is small, the safety test of the PTAs may need a large amount, which can be up to kilograms. As a result, the cost of noble metals is relatively larger than the semiconductors, which consists of abundant elements in the earth’s crust, such as O (48.6%), Si (26.3%) and Fe (4.75%). The cost of precursors used and scalable fabrication process needs to be considered. However, papers reported mainly focussed on the novel PTAs or the enhancement of photothermal performance by designing and adjusting the reported PTAs.

4.1.5 Comparisons of PTAs

After discussing about the factors of the PTAs, some of the representative materials of noble metals, semiconductors, carbon-based PTAs, Si-based materials, Fe-based materials are compared here, including the extinction coefficient, photothermal conversion efficiency, wavelength of laser and so on, which can be seen in Table 5 below. There are also many other factors related to the PTAs, such as particle size, dosage used, power density used, injection pattern, thermal conductivity, heat capacity, scalable synthesis and the cost, which are not included here.

materials	Laser wavelength (nm)	ε	η (%)	ref
Pd nanosheets	1045nm	$4.1\times10^{9}\ M^{-1}\ cm^{-1}$	-	Nat. Nanotechnol. 6 (2011) 28-32.
Pd@Au	-	-	28.6%	Adv. Mater. 26 (2014) 8210-8216.
Pd@Ag	808nm	-	52%	Adv. Mater. 23 (2011) 3420-3425.
PEG-BPQDs	808nm	$14.8\ Lg^{-1}\ cm^{-1}$	28.4%	Angew. Chem. Int. Ed. 127 (2015) 11688-11692.
PEG-BP NPs	808nm	$2.1\ Lg^{-1}\ cm^{-1}$	36.8%	Biomaterials 91 (2016) 81-89
PEG-MoS_2	800nm	$28.4\ Lg^{-1}\ cm^{-1}$	-	Adv. Mater. 26 (2014) 3433-3440
MoS_2-CS [130]	808nm	-	24.37%	ACS Nano 8 (2014) 6922-6933
Ti_3C_2 [107]	808nm	$25.2\ Lg^{-1}\ cm^{-1}$	30.6%	Nano Lett. 2017, 17, 384.
Ta_4C_3 [86]	808nm	$4.06\ Lg^{-1}\ cm^{-1}$	44.7%	Adv. Mater. 2018, 30, 1703284.
Nb_2C [131]	1064nm	$37.6\ Lg^{-1}\ cm^{-1}$	45.65%	J. Am. Chem. Soc. 2017, 139, 16235.
Conjugated Polymer NPs [132]	1064nm	-	50%	ACS Appl. Mater. Interfaces 2018, 10, 7919-7926
Graphdiyne-PEG [84]	808nm	$10.1\ Lg^{-1}\ cm^{-1}$	42%	Chem. Mater. 2017, 29, 6087-6094
FeS-PEG [23]	808nm	$15.5\ Lg^{-1}\ cm^{-1}$	-	Biomaterials 38 (2015) 1-9

Table 5 Comparisons of PTAs for photothermal therapy.

There are some photothermal agents reported with high photothermal conversion efficiency. The comparisons with these agents together with the experimental details, including solution concentrations, wavelength, power density, irradiation time and so on, are shown in Table 6. More standard setups, conditions and calculations need to be unified for the photothermal performance of the photothermal agents.

materials	*solution concentrations*	*Wavelength (nm)*	*power density (W/cm^2)*	*irradiation time (min)*	*η*	*ref*
Pd NPs	50 μg/mL	808	8	30	93.4%	Nanoscale, 2014, 6, 4345
$CuFeSe_2$ NPs	50 μg/mL	808	0.75	15	82%	ACS Nano 2017, 11, 5633−5645
Au bellflowers	-	808	1	5	74%	J. Am. Chem. Soc. 2014, 136, 8307−8313.
$CuCo_2S_4$ NPs	50 μg/mL	915	0.189 W	5	73.4%	Adv. Funct.Mater.2017, 27, 1606218
cobalt sulfide	40 μg/mL	808	0.7	5	70.1%	Nanoscale, 2018, 10, 14190
Au nanocages	$1.0*10^{10}$ particles/mL	808	0.4	10	64%	Angew. Chem., Int. Ed. 2013, 52, 4169−4173.
MoO_{3-x} NPs	20 ug/ml	808	1	10	63.7%	J. Mater. Chem. B, 2019, 7, 2032--2042
Pd Nanosheets	30 μg/mL	808	1 W	10	52%	small 2014, 10, No. 15, 3139–3144
Conjugated Polymer NPs	10 μg/mL	1064	0.9	10	50%	ACS Appl. Mater. Interfaces 2018, 10, 7919-7926
$SiO_{0.92}$ NPs	36 μg/mL of Si	1064	1	25	48.6%	Biomaterials 143 (2017) 120-129
Si NPs	100 ug/ml	808	1 W	10	33.6%	ACS Appl. Mater. Interfaces 2018, 10, 23529−23538
FeSi NPs	0.5 mg/mL	1064	1	10	76.2%	this work

Table 6 Experimental details of some photothermal agents with high photothermal conversion efficiency.

4.1.6 Clinical progress of PTT

The clinical application of photothermal agents for photothermal therapy is a long journey, which may need many years, including the synthesis of the PTAs, adjusting the photothermal properties, cells test, animal test and preclinical test and so on. The Figure 49 below shows an example of clinical therapy progress for two-dimension (2D) MXenes used in nanomedicine. Like 2D MXenes, almost all the biomaterials for medical application will undergo the similar long period [133].

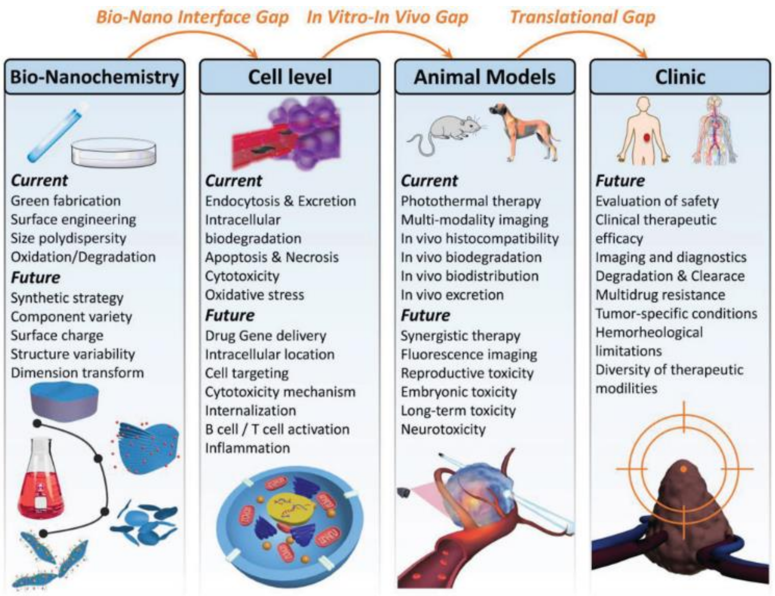

Figure 49 Summary of current research developments for biomedical applications. Adapted from (Lin 2018).

For many photothermal agents, such as Ag, PT, Pd, P, Si, $Cu_{2-x}S$, Fe_3O_4 and polydopamine, they are usually tested by the photothermal performance in aqueous suspensions, cell test (*in vitro*) and animal test (*in vivo*). While, Au-based agents have been used in clinical trial for PTT [134].

The PTA most close to clinical therapy is the SiO_2-Au@PEG nano-shells with 150nm size, reported in 2003 by Naomi J. Halas [135]. The clinical trials of prostate cancer started in 2016. The Figure 50 below shows the success in 94% (15/16) of patients by gold-silica nanoshell-mediated focal laser ablation. Therefore, the photothermal therapy seems to be efficient and safe for prostate cancer and other cancer in the future [134].

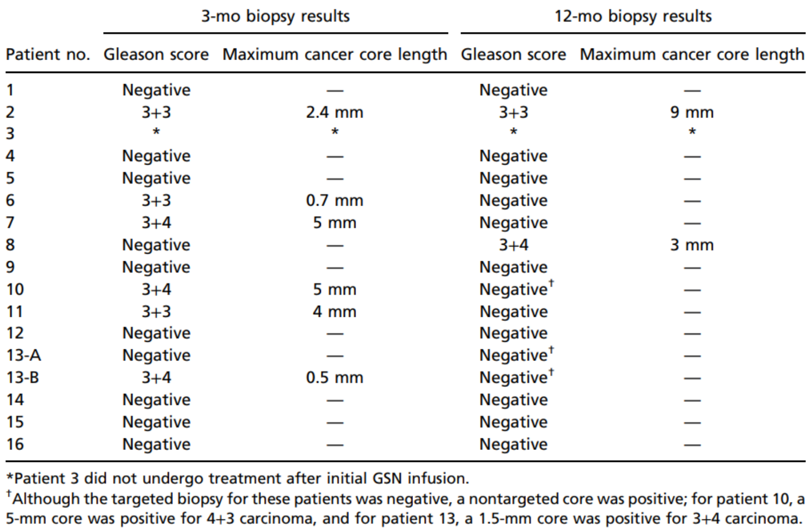

	3-mo biopsy results		12-mo biopsy results	
Patient no.	Gleason score	Maximum cancer core length	Gleason score	Maximum cancer core length
1	Negative	—	Negative	—
2	3+3	2.4 mm	3+3	9 mm
3	*	*	*	*
4	Negative	—	Negative	—
5	Negative	—	Negative	—
6	3+3	0.7 mm	Negative	—
7	3+4	5 mm	Negative	—
8	Negative	—	3+4	3 mm
9	Negative	—	Negative	—
10	3+4	5 mm	Negative[†]	—
11	3+3	4 mm	Negative	—
12	Negative	—	Negative	—
13-A	Negative	—	Negative[†]	—
13-B	3+4	0.5 mm	Negative[†]	—
14	Negative	—	Negative	—
15	Negative	—	Negative	—
16	Negative	—	Negative	—

*Patient 3 did not undergo treatment after initial GSN infusion.

[†] Although the targeted biopsy for these patients was negative, a nontargeted core was positive; for patient 10, a 5-mm core was positive for 4+3 carcinoma, and for patient 13, a 1.5-mm core was positive for 3+4 carcinoma.

Figure 50 3-month and 12-month follow-up biopsy results from the targeted ablation zone. Adapted from (Rastinehad 2019).

Although the good news of the clinical trials, the challenges for clinical use are still difficult. There is no clear long-term biological behaviour of Au due to its chemical inertness. There is no model standards of nanoparticles and treatment standardization. Small light penetration depth and poor efficiency of delivering nanoparticles to tumour site also limit their clinical application.

4.2 Experimental

4.2.1 Materials

In this chapter, materials of fabricated FeSi NPs in the PBS buffer solution and PBS buffer solution are used. Mice were bought from the Guangdong Medical Laboratory Animal Centre (China). Mouse colonic epithelial 4T1 cells were bought from Guangdong Microbial Culture Collection Centre (China).

4.2.2 *In vivo* PTT

All animal operations were performed under protocols approved by the Institutional Animal Care and Use Committee of Southern University of Science and Technology. Mouse colonic epithelial 4T1 cells (2 × 10^6 cells, total volume 0.05 mL in 1×PBS buffer) were injected into mice (Female BALB/c nude mice, 4-6 weeks) legs subcutaneously to establish tumours. Mice were randomly divided into 4 groups (4 mice per group) for photothermal therapy experiment when the volume of the tumours were about 60 mm^3 as calculated and measured by a calliper. Two groups of 4T1 (murine breast cancer cells) tumour-bearing mice were intratumorally (i.t.) injected with 20 μL of 2 mg mL^{-1} of FeSi NPs in phosphate buffer saline (PBS), equivalent to a dose of 1.78 mg kg^{-1}. Another two groups of 4T1 tumour-bearing mice were intratumorally injected with the same amount of PBS solution (20 μL) for comparison. The FeSi-treated group and PBS-treated group were exposed to the 1064 nm laser at a laser power density of 1 W cm^{-2} for 15 min. The other two were not treated by laser for comparison. An infrared (IR) thermal imaging camera (FLIR E6) was used to monitor the temperature of tumours. The size of the tumour was recorded by a calliper every other day after treatment to calculate the tumour volume based on the approximate volume equation, V = (tumour length) × $(\text{tumour width})^2/2$. For easy comparison, the relative tumour volumes were calculated as V/V_0 (V_0 was the tumour volume measured at the beginning of the treatment). Body weight of each mouse was determined and recorded every other day until the sacrifice of the mice. The sections of tumour were collected at 14th day and stained with H&E for histological analysis.

4.2.3 *In vivo* biocompatibility of FeSi NPs

4T1 tumour-bearing mice were intratumorally injected with FeSi NPs PBS suspensions and PBS only, followed with or without laser irradiation. At the 14th day after treatment, the organs (lung, liver, heart, spleen and kidney) were harvested from the sacrificed mice. Then these organs were fixed in 4% paraformaldehyde at 4 °C overnight and embedded in paraffin for preparation of 5 μm thick sections, followed by H&E study.

4.3 Results and discussion

4.3.1 Temperature change of tumour after injection and laser irradiation

From the promising photothermal efficiency and stability of FeSi NPs (chapter 3) without any anticipated biohazard, they were tested as photothermal agents for *in vivo* cancer therapy.

One group of 4T1 tumor-bearing mice were i.t. injected at a dose of 1.78 mg kg^{-1} FeSi (20 μL of 2 mg mL^{-1}). The mice were then exposed to a 1064 nm laser of 1 W cm^{-2} power density for 15 min. Tumor-bearing mice i.t. injected with the same volume of PBS without FeSi NPs were also exposed to the 1064 nm laser (1 W cm^{-2}) as a control. An infrared (IR) thermal imaging camera was chosen for monitoring temperatures of tumors under the irradiation by laser. When exposed to the laser at 1 W cm^{-2}, the temperature of the tumor surface increased for both cases as shown in Figure 51a, more so for the case with FeSi NPs. As shown in Figure 51b, the temperature of the tumor injected with FeSi increased to around 55 °C within 5 min, which is sufficiently high to kill tumor cells and inhibit their growth *in vivo*. In contrast, the tumor temperature without FeSi showed only a marginal increase in temperature under the laser irradiation of the same intensity.

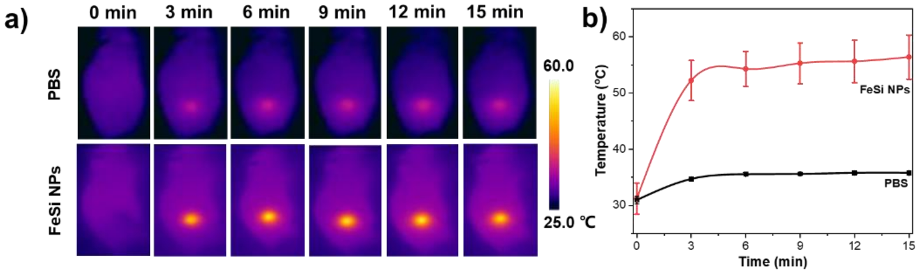

Figure 51 a) Photothermal images of mice i.t. injected with FeSi NPs and PBS under a 1064 nm laser irradiation at 1 W cm^{-2} for 15 min; b) Temperature change curves of 4T1 tumors upon laser irradiation.

4.3.2 Volume change of tumour after injection and laser irradiation

The efficiency of PTT with pFeSi NPs to kill and prohibit tumors was estimated by measuring the size of the tumor. The mice bearing 4T1 tumors with volume of around 60 mm^3 were randomly divided into four groups: (1) i.t. injection of 20 µL PBS, (2) i.t. injection of 20 µL PBS with laser irradiation, (3) i.t. injection of 20 µL FeSi NPs in PBS (dose of 1.78 mg kg^{-1}) without laser irradiation, and (4) i.t. injection of 20 µL FeSi NPs in PBS (dose of 1.78 mg kg^{-1}) with laser irradiation. The laser of 1064 nm at 1 W cm^{-2} was applied for 15 min whenever applicable. The tumors after injection of FeSi followed by laser irradiation were found to eradicate without recurrence within 14 days as shown in Figure 52a. The tumors of all other groups in comparison had less trend of growth inhibition. The changes of tumors can also be seen in Figure 52b, showing eventual disappear of the tumor after injection of FeSi NPs followed by the laser irradiation.

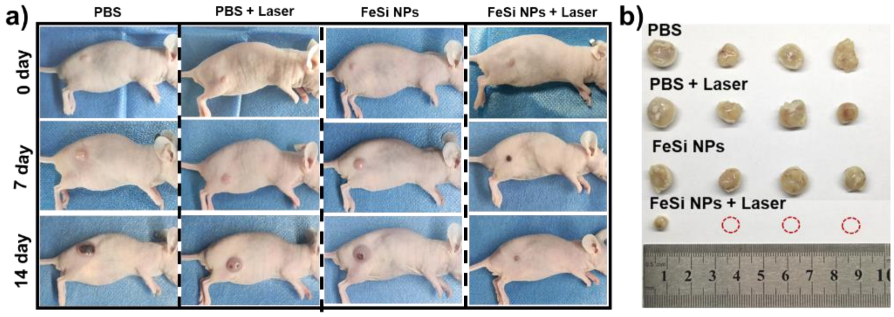

Figure 52 a) Variation of mice tumor after being i.t. injected with PBS and FeSi NPs with and without laser irradiation after 0, 7 and 14 days; b) Representative photographs of tumors obtained from mice at day 14 after different treatments.

Figure 53a shows typical tumor growth profile by recording the relative volume of tumor every two days after irradiation treatments. Superior tumor suppression two weeks after the irradiation treatment was observed in the group of FeSi NPs with laser radiation, owing to the effective photothermal effect. It is interesting to note insignificant change in the weight of mouse body during the therapeutic course for all the groups as shown in Figure 53b, suggesting a negligible toxicity and short-term side effect of the treatment.

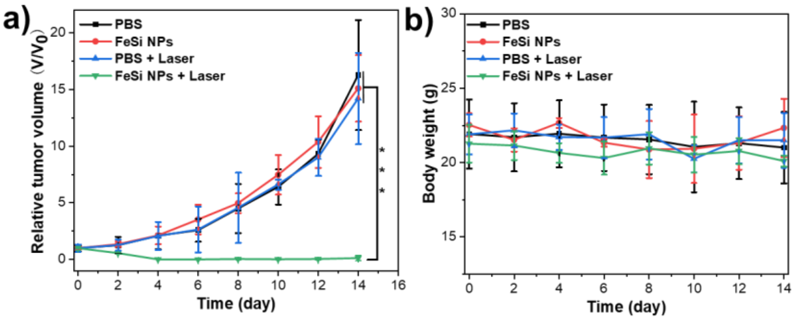

Figure 53 a) Growth curves of mice tumour size under different treatments; b) Variation of the mouse weights with time after different treatments.

4.3.3 H&E staining of tumor slices (photothermally induced necrosis) and major organs (*in-vivo* biocompatibility data)

To compare the tumor obliteration effect, tumor sections were collected and processed by hematoxylin and eosin (H&E) staining. From the H&E staining, Figure 54a shows the most severe occurrence of necrosis in the FeSi NP + laser group among all groups. To assure the low toxicity of FeSi NPs for *in vivo* application, histology and morphology of major organs on day 14, including lung, liver, heart, spleen and kidney were visually inspected. As shown in Figure 54b, there is no abnormal cell damage or tissue inflammation in the organ tissues as compared with the control group. As a result, FeSi NPs have been shown a good biocompatibility, which is safe for organisms.

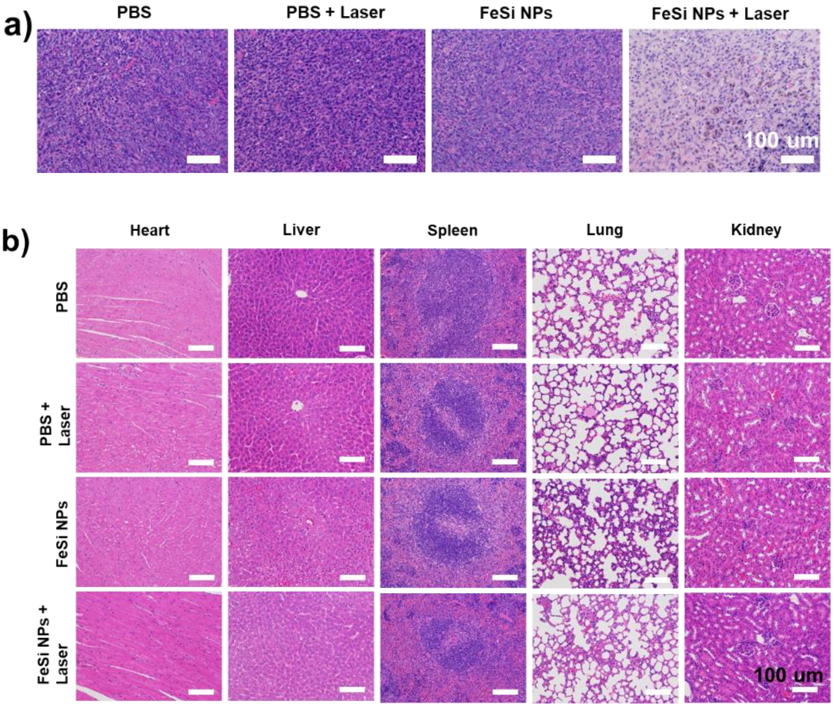

*Figure 54 a) H&E staining of tumor slices in mice of each group after treatment; b) Histological sections of major organs. P values: ***p < 0.001.*

4.4 Conclusions

For the photothermal performance of tumour, the temperature of the tumor injected with FeSi after laser irradiation can reached around 55 °C within 5 min, while the temperature of the tumor injected with only PBS solution showed only a marginal increase in temperature under the laser irradiation of same intensity. Tumors of mice almost eventually disappear without recurrence within 14 days after injection of FeSi NPs followed by the laser irradiation, characterized by the optical images of tumours, tumour volumes and hematoxylin and eosin (H&E) staining of tumor sections. The tumors of all other groups in comparison did not show any trend of growth inhibition. Insignificant change in the weight of mouse body during the therapeutic course for all the groups suggests a negligible toxicity and short-term side effect of the treatment. No abnormal cell damage and tissue inflammation in the organ tissues show that FeSi NPs have good biocompatibility and are safe for organisms. In summary, the results demonstrate a good *in-vivo* cancer therapy of the PTT mediated by FeSi NPs.

Chapter 5. Biodegradability investigations of FeSi

5.1 Introduction

Biocompatibility, biological activity, biodegradability and cytotoxicity are important properties of materials for medical applications [136]. Biological activity, also known as bioactivity, means the property of inducing biological and chemical reactions at the interface between materials and biological tissues [137]. Material's bioactivity in SBF solution is usually characterized by the formation speed and amount of $Ca_5(PO_4)_{3-x}(CO_3)_xOH$ (HCA). HCA is the main inorganic salt of human bone tissue and the key substance chemically prepared by bone repair material and host bone. Biodegradability means the material will degrade after some time in the body. Cytotoxicity is the ability of a foreign agent and its degradation product to destroy or kill cells. For desired photothermal agents used for photothermal therapy, they should have good biocompatibility, bioactivity, suitable degradation degree and less cytotoxicity. This thesis focuses on the biodegradability of photothermal agents, mainly discusses about the definition of biodegradability, biodegradable materials and applications, biodegradability in photothermal therapy, characterization of biodegradability.

5.1.1 Definition of biodegradability

Biodegradation is the breakdown of organic or inorganic material by microorganisms or solutions, such as bacteria, fungi, simulated body fluid (SBF) and body fluid. In fact, almost all compounds and materials undergo a biodegradation process. For photothermal therapy, photothermal agents should degradate within several months after laser irradiation. Long-term biological behaviour of agents, which are not biodegradable, inside the body is unclear [113]. Therefore, suitable extent of degradation of agents is required in photothermal therapy.

5.1.2 Biodegradable materials and applications

Biodegradable materials can be used in the fields of packing, tableware, agriculture and biological medicine. For biomedical field, biodegradable materials have some advantages in some applications such as tissue engineering, bone regeneration, drug delivery and photothermal therapy and then degrade to some product which can be absorbed or excreted to the outside of the body. Biodegradable materials can be divided into three kinds metal materials [138], inorganic non-metallic materials and organic materials [139], which can be seen in Table 7. This thesis focuses on the Si/Fe-based materials, so biodegradable porous silicon and metal iron (Fe) are introduced in detail.

types	*metal materials*	*inorganic non-metallic materials*	*organic materials*
materials	Magnesium, iron, zinc and (magnesium, iron, zinc,	Bioceramics, tricalcium phosphate, tetralcium phosphate, hydroxyapatite, silicon (Si), phosphorus (P)	natural materials: polysaccharide (cellulose, chitin, starch, lignin, alginate); protein (collagen, fibrinogen)

	tungsten, calcium, zinc, strontium)-based alloys		synthetic polymer: poly α-hydroxy acid, polyanhydride, poly α-amino acid, aliphatic polyester
applications	coronary stents; paediatric implants	drug delivery, tissue engineering scaffolds	grafts, sutures, implants, depots

Table 7 Biodegradable materials of different classes and their medical uses.

5.1.2.1 Biodegradable porous silicon

The degradation mechanism of silicon can be described with a two-step process as below.

$$Si + 2H_2O \rightarrow SiO_2 + 2H_2 \cdots\cdots\cdots\cdots\cdots (5\text{-}1)$$

$$SiO_2 + 2H_2O \rightarrow Si(OH)_4 \cdots\cdots\cdots\cdots\cdots (5\text{-}2)$$

The first step is the preliminary hydrolysis, from Si to oxide phase. The second step is the complete hydrolysis, from oxide phase to orthosilicic acid, which can be excreted to the outside of the body. The extent of degradation of porous silicon can be tuned by the porosity [140], surface chemistry and pH of tissue. High porosity of pSi (>80 % porosity) shows exponential release of silicic acid over time [140]. The extent of degradation of pSi can be controlled from minutes to months [141]. With a dual-PEGylation of pSi, the half-life increased from 0.8 to 3.0 days [142]. The extent of degradation of pSi also increases with improved pH [140].

5.1.2.2 Biodegradable metal iron (Fe)

Iron and iron-based alloys are biodegradable, which can be used in applications of coronary stents or paediatric implants. The advantages of iron are that the iron ion (Fe^{2+}) is an important element of the body and an important component of various enzymes, and that the mechanical properties of iron are comparable to scaffold materials.

Degradation mechanism of Fe alloys is oxidation absorption in solutions [143]. The detailed procedures of Fe in Hank's solution are as below [144].

$$Fe \rightarrow Fe^{2+} + 2e^- \cdots\cdots\cdots\cdots\cdots \text{(5-3)}$$

$$Fe^{2+} \rightarrow Fe^{3+} + e^- \cdots\cdots\cdots\cdots\cdots \text{(5-4)}$$

$$1/2O_2 + H_2O + 2e^- \rightarrow 2OH^- \cdots\cdots\cdots\cdots\cdots \text{(5-5)}$$

$$Fe^{2+} + 2OH^- \rightarrow Fe(OH)_2 \cdots\cdots\cdots\cdots\cdots \text{(5-6)}$$

$$Fe^{3+} + 3OH^- \rightarrow Fe(OH)_3 \cdots\cdots\cdots\cdots\cdots \text{(5-7)}$$

Fe is firstly oxidized to Fe^{2+}, some of Fe^{2+} is further oxidized to Fe^{3+}. $Fe(OH)_2$ and $Fe(OH)_3$ are produced under the condition of alkaline and oxygen environment. Figure 55 below shows degradation mechanism of Fe–Mn alloy in Hank's solution.

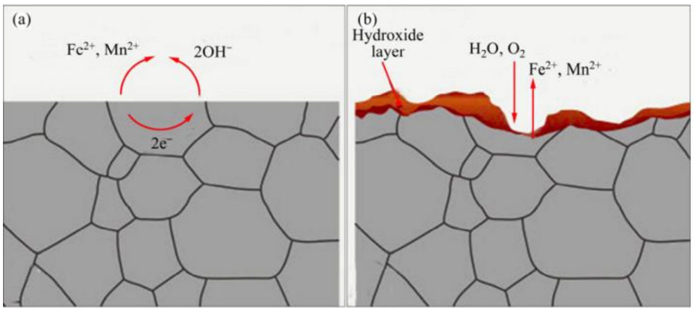

Figure 55 Illustration of degradation mechanisms of Fe–Mn alloys: (a) Initial degradation reaction; (b) Formation of hydroxide layer. Adapted from (Zhen 2013).

5.1.3 Biodegradability in photothermal therapy

For photothermal agents, noble metals and carbon-based nanoparticles are almost unbiodegradable. Many semiconductors, such as chalcogenides [145–147], oxide [148–150], Mxene materials [131,151,152], pSi [153] and phosphorus (P) [154–156], are biodegradable. Researchers proved that chalcogenides are likely to release toxic metallic ion [157] and that sulfide can induce dysfunction in organisms [158]. Therefore, the safety of degradation product is also important for PTAs, which needs to be considered.

The long-term accumulation of nanoparticles can pose some unpredictable risks, such as severe oxidative stress, phagocytic activity damage of mononuclear phagocyte and so on. If the hydrodynamic diameter of nanoparticles is less than 5.5nm, they can be excreted to the outside of the body via kidney. But almost all photothermal agents are larger than 5.5 nm, therefore, it is important to fabricate the biodegradable agents. For intravenous injection, it needs some time for the highest concentration of photothermal agents to accumulate in the tumour site. Therefore, the agents should degradate after the laser radiation. While for intratumor injection, the extent of degradation can be fast. Sometimes the therapy needs several times of laser radiation for multiple photothermal therapy. There is not much research about the degradation rate of the PTAs, which needs to be paid more attention before their final clinical treatment.

5.1.4 Strategy for controlling degradation rate

The degradation rate can be controlled through material design and external stimulus. Material design includes composition control and structure design. The addition of elements, porous structure, porosity and surface modification can tune the degradation rate. Biodegradable materials can be biodegraded by hydrogen evolution reaction, hydrolyzation, oxidization and structural damage via immersing in solution and various irritants such as shake, enzyme, pH and near-infrared lasers. Suitable material/solution ratio is needed to be considered because degradation product has saturation solubility in the solution.

5.1.5 Characterization of biodegradability

There are several ways to characterize the biodegradability of materials. Some research groups investigate the biodegradation behaviour of photothermal agents in water, observing the colour change of the solution containing the PTAs, absorbance intensity of the materials in solution, morphology change by SEM, change of photothermal heating curves after storing for some time. Some research groups investigate the biodegradation behaviour of photothermal agents in solution systems by the methods of mass loss, ion release concentration, electrochemical test and hydrogen evolution (Mg alloys in simulated body fluid).

For biodegradable testing of particles, ion release concentration, which can be achieved via ICP-MS or AAS, is a suitable choice. This thesis chooses this method for investigating the biodegradation behaviour of FeSi nanoparticles.

Several solutions were used in the past twenty years to mimic the real body fluid. They are 0.9% NaCl aqueous solution, SBF, Hank’s, PBS, dulbecco's modified eagle medium (DMEM) and so on. SBF containing similar components to human blood plasma [159] is usually applied as electrolyte solution for testing the biodegradability of the materials. The components of concentrations (mM) of ions in three fluids can be seen in Table 8 [160].

Formulation	***Na^+***	***K^+***	***Mg^{2+}***	***Ca^{2+}***	***Cl***	***HC^{-3}***	***$HPO2^{-4}$***	***$SO2^{-4}$***	***Buffer***
Blood plasma [161]	142.0	5.0	1.5	2.5	103.0	27.0	1.0	0.5	-
Original SBF [162]	142.0	5.0	1.5	2.5	147.8	4.2	1.0	0.5	Tris
Modified SBF [163]	142.0	5.0	1.5	2.5	103.0	10.0	1.0	0.5	HEPES

Table 8 Comparisons of concentrations of ions in three simulated body fluids used for testing purposes.

ICP-MS and AAS are needed for determining concentrations of the ions for calculating the degradation rate of the materials. The specific information of the ICP-MS and AAS can be seen in Table 9.

Details	*ICP-MS*	*AAS*
Fundamental principles	Ionization, mass/ charge ratio separation	Lambert-beer law
Instrumentation	inductively coupled plasma, connector, mass spectrometer	light source, sample atomizer, monochromator, data processing system
Applications	Environment, semiconductors, biology, materials	theoretical research, elemental analysis
Strengths	Fast testing speed, low detection limit (<1 ppt)	Simple operation, good reproducibility
Limitations	Not suitable for high concentration; interference problem, such as mass spectrum or acid	Cannot analyse solid sample
Sample collection, preparation	sample should be fully digested/diluted without particle	sample should be fully digested/diluted without particle
Equipment used	Agilent ICP-MS 7700X	AA-7000 SHIMADZU

Table 9 Information on the techniques used for characterisation.

5.2 Experimental and methods

5.2.1 Materials and characterization

For materials, SBF is chosen for the biodegradable research of the materials, which was prepared in the lab of UoB and SUSTech; bulk of tabasheer was purchased from Bristol Botanicals (Bristol, UK); F-FeSi and F-Fe were fabricated; C-FeSi and C-Fe were purchased from Jiu Ding (Beijing, China) and Flance (Beijing, China); Si wafer was purchased from Jingze Electron (Dongguan, China).

For characterization, ICP-MS (Agilent 7700X) and AAS (Shimadzu AA-7000) were used to give the concentration of ions in the solution.

5.2.2 Preparation of SBF solution

5.2.2.1 Reagents for preparation of SBF

NaCl, $NaHCO_3$ and Na_2SO_4 were purchased from Aladdin (Shanghai, China); KCl, $MgCl_2$, $CaCl_2 \bullet 2H_2O$ and hydroxymethyl aminomethane (Tris) were purchased from Macklin (Shanghai, China); potassium dihydrogen phosphate (KH_2PO_4) was purchased from Lingfeng (Shanghai, China).

5.2.2.2 Preparation procedure and tips of SBF

For 1000 ml of SBF, 900 ml of ultra pure water and a stirring bar are put into 1500 ml plastic beaker, which is put on the hot plate with a stirring function. The temperature is set 36.5 ℃. A speed is set for the stirring bar. Reagents of 8g NaCl, 0.353g $NaHCO_3$, 0.298g KCl, 0.136g KH_2PO_4, 0.143g $MgCl_2$, 0.368g $CaCl_2 \bullet 2H_2O$, 0.071g Na_2SO_4, 39mL HCl (1M) and 6.118g Tris are dissolved into the solution one after another. Around 10mL HCl (1M) was added into the solution, waiting for room temperature and constant volume to 1000mL. At last, the pH should be around 7.4.

There are some tips for the preparation procedure. Each component is added in the same order and cannot be added randomly. Each component dissolves completely before adding the next component. If precipitates occur during the preparation procedure, the solution should be discarded and prepared again. The prepared SBF is stored in the refrigerator below 10℃ to prevent precipitation. (Preservation). It should be used within 30 days. If there are some precipitates, discard it. It is always better to prepare fresh.

5.2.3 Immersion test

For bulk tabasheer, a size around of 5mm (40-51mg) of it was put into a plastic bottle with 100mL SBF (concentration between 0.4 and 0.51mg/mL). The entire sample should be submerged in the SBF. The plastic bottles are kept in the incubater at 36.5℃. Samples are carried out in quintuplicate. There are sampling points at 1day, 2day, 3day, 7day and 21day. At each sampling point, the specimens are withdrawn and dried to weigh the bulks. Based on the initial and final weight, degradation can be determined. This result may overestimate degradation, considering the possibility of “the bulk piece” losing microparticles rather than individual silicic acid molecules.

For powders, degradation tests of them were carried out by incubating the particles in SBF at 36.5°C. 1mg, 5mg and 10mg of F-FeSi NPs are chosen for the test. Samples is carried out in sextuplicate. Adding the 20ml of SBF solution (0.05mg/mL, 0.25mg/mL and 0.5mg/mL) in 6 plastic bottles respectively, and placing the specimens in the SBF solutions. The entire sample should be submerged in the SBF. The plastic bottles are kept in the incubater at 36.5℃. There are sampling points at 1day, 2day, 3day, 7day, 14day and 21day. At each sampling point, the specimens are withdrawn and centrifuged to separate the NPs. 5ml of supernatant is analyzed with the ICP-MS to determine the concentration of the dissolved Si and Fe. 10mg of C-FeSi NPs (0.5mg/mL) are also tested as comparison under the same conditions.

5.3 Results and Discussion

5.3.1 Biodegradability test of bulk tabasheer

The degradation is calculated as the ratio of weight loss (initial weight subtract final weight) to initial weight. From the Table 10 we can see that bulk tabasheer is biodegradable and the loss of weight increases with days of immersion in SBF. From the Figure 56 we can see that the degradation of bulk tabasheer in SBF solution increases with increasing days of immersion but the degradation rate decreases with time. Over the first week the average degradation rate is ~2.5%/day falling to < 1%/day after two weeks. The degradation is 26.56% after 21 days. It can be assumed that there will be a higher degradation rate if the bulk is crushed into powders.

time (days)	1	2	3	7	21
initial weight (mg)	48.1	44.5	41.1	51.0	41.8
final weight (mg)	47.6	42.4	37.6	41.8	30.7
loss of weight (mg)	0.5	2.1	3.5	9.2	11.1

Table 10 Weight change of bulk tabasheer after increasing days of incubation in SBF.

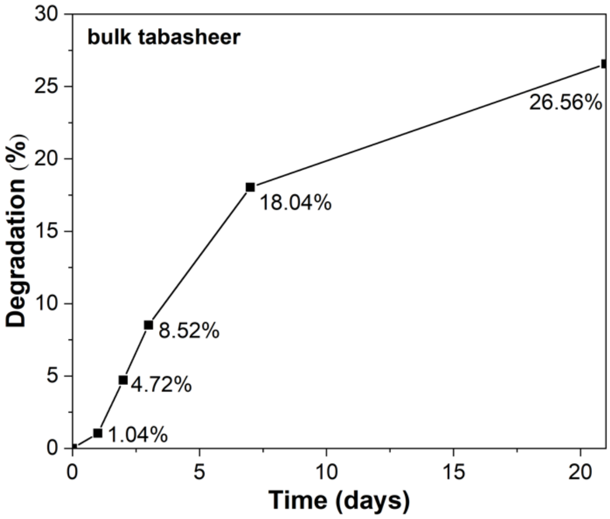

Figure 56 Degradation of bulk tabasheer in SBF solution after different days.

5.2.3 Biodegradability test of fabricated FeSi NPs

The extent of degradation of F-FeSi NPs is calculated as the ratio of final concentration of Si ion in the solution to initial concentration of element Si. From Figure 57 we can see that the F-FeSi NPs are biodegradable, which is good for photothermal therapy. The degree of degradation is dependent on the concentration of F-FeSi NPs. With the increase of the initial concentration, the extent of degradation decreases. It is because that the Si ion and degradation product $Si(OH)_4$ has saturation solubility in the solution. The extent of degradation of 0.05mg/mL and 0.25mg/mL of F-FeSi is around 35% and 25% after a week, while the value of 0.5mg/mL of F-FeSi is around 12% after a week and 15% after three weeks.

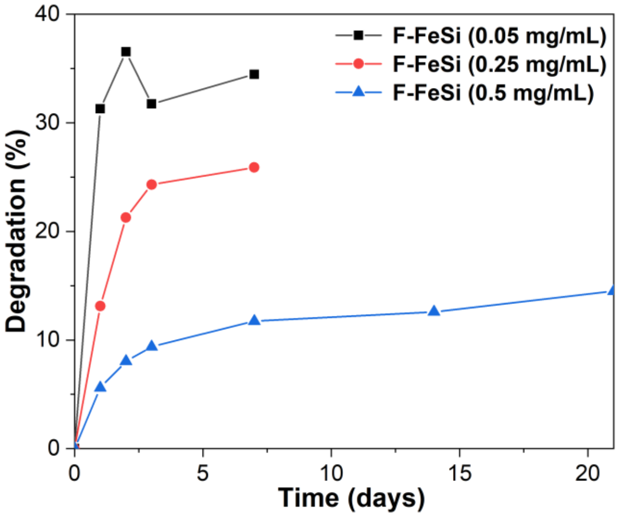

Figure 57 Degradation of F-FeSi with three concentrations in SBF solution after different days.

From Figure 58 we can see that C-FeSi NPs are also biodegradable. However, the extent of degradation is much low, only 2% after three weeks. The reason may be that the mesoporous structure and higher surface area of F-FeSi NPs can help accelerate the degradation of FeSi NPs. From Table 11 and Figure 59 we can see that F-FeSi NPs have a much higher specific surface area and pore volume compared to C-FeSi NPs.

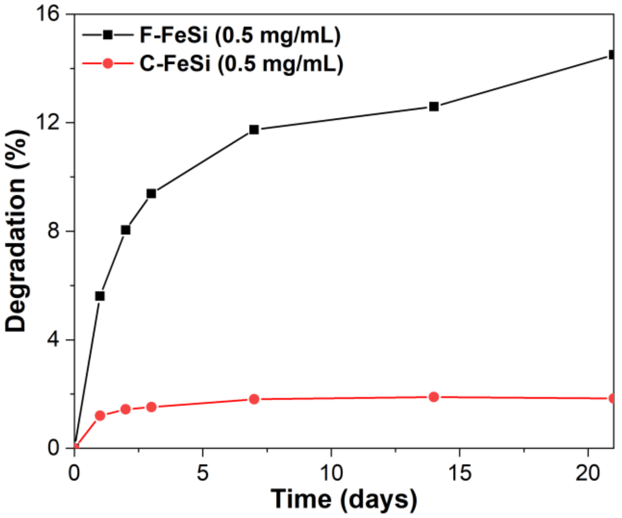

Figure 58 Degradation of F-FeSi and C-FeSi NPs in SBF solution after different days.

Samples	**S_{BET} (m^2/g)**	**V_a (cm^3/g)**	**P_D (nm)**
F-FeSi	90	0.21	9
C-FeSi	7.5	0.03	-

Table 11 BET results of F-FeSi and C-FeSi particles.

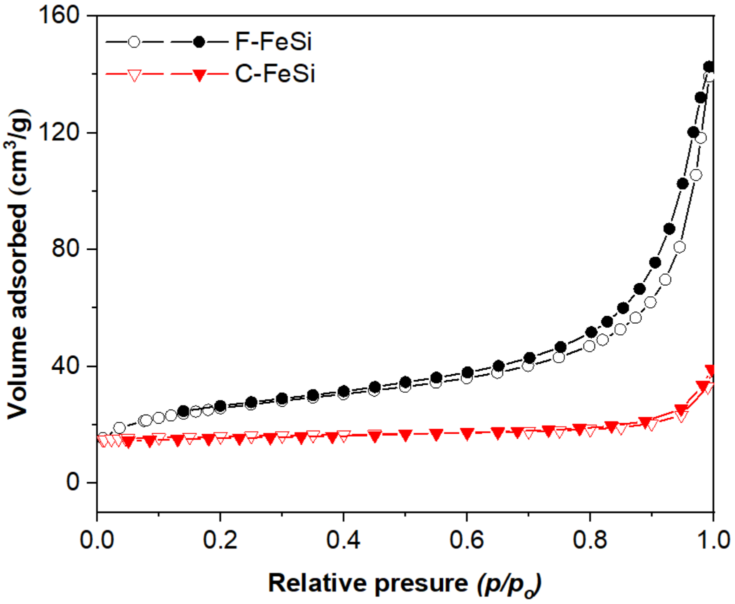

Figure 59 N_2 adsorption-desorption isotherm of F-FeSi and C-FeSi particles.

Please note that the effect of plastic container vessel on the Si concentration in SBF is not considered, because many plastic bottles are made using silicone-based processing aids. The inner walls of the container can release low levels of silicon containing molecules (ppb) over long incubation times. As a result, although the standard solution contains both Fe and Si, the correlation coefficient (R) of Si is 0.88, while Fe is 0.9999. Therefore, the result of degradation degree is for silicon is qualitative, not quantitative.

The extent of degradation of F-FeSi NPs is not calculated as the ratio of final concentration of Fe ion in the solution to initial concentration of element Fe. The reason is that Fe ion and degradation product $Fe(OH)_2$, $Fe(OH)_3$ and FeO(OH) have much low saturation solubility in the solution.

5.3 Conclusions

SBF solutions were prepared in both UoB and SUSTech. The precursor of bulk tabasheer, used for fabricating FeSi NPs, is biodegradable with degradation of 26.56% after 21 days. Fabricated and commercial FeSi NPs are both biodegradable. Fabricated FeSi NPs have a much higher degradation (15%) compared with commercial FeSi NPs (2%) after three weeks due to their mesoporous structure and high surface area. With lower initial concentration of nanoparticles, the extent of degradation can be higher due to the saturation solubility of the degradation product.

Chapter 6. Overall conclusions and potential future work

6.1 Overall conclusions

In this work, a novel kind of FeSi NPs, as a new class of transition-metal silicide photothermal agents, were fabricated using green chemistry method of magnesiothermic co-reduction from biogenic tabasheer for photothermal therapy. The low band gap of 0.128 eV of the synthesized FeSi NPs helped enhance the optical absorption and photothermal conversion efficiency. The materials showed a good optical absorption with a mass extinction coefficient of 13.3 L g^{-1} cm^{-1} at 1064 nm, which compared favourably with many other Si-based and Fe-based photothermal agents. The photothermal conversion efficiency was 76.2%, which is higher than the values of many existing photothermal agents. *In vivo* tests showed that photothermal treatment is effective to prohibit the tumour growth and even kill the tumour cells. The precursor of bulk tabasheer and fabricated FeSi NPs are both biodegradable. Our work suggests that FeSi NPs are likely to be a new class of photothermal agents for the NIR-II tissue window, and thereby highly promising in cancer therapy. The mesoporous structure can help achieve drug delivery and chemotherapy. The findings described provide new insights towards understanding the role of transition-metal silicides based on the photothermal conversion in photothermal therapy and other potential applications such as multifunctional therapy, desalination, photothermal catalysis, photothermal membranes and so on.

6.2 Future work

For the synthesis, controllable size distribution needs to be obtained; Increasing repetition rate and purity of fabrication; Achieving quantitative production of FeSi; fabricating FeSi with Fe and Si nanoparticles for understanding the synthesis mechanism of FeSi; Other transition metal silicide and binary metal alloy can be fabricated with the magnesiothermic co-reduction method.

For the properties, the fabricated FeSi NPs have poor dispersity in water and PBS buffer solution. Therefore, successful surface modification is required for increasing the dispersity of FeSi NPs in water in the future. When the problem is solved, intravenous injection can be used for the photothermal therapy. In vitro cytotoxicity-test can also be investigated.

For the applications, porous and magnetic FeSi NPs can be used for drug delivery for chemotherapy for multifunctional therapy with photothermal therapy; Magnetic FeSi NPs may be used as MRI contrast agent for imaging, which needs to be investigated in the future; Porous FeSi NPs can be used as, photothermal agents and biological scaffold due to the specific property of Fe and Si, for photothermal therapy of bone tumour and subsequent bone regeneration; Photothermal conversion materials can be used for heat preservation for skin, photothermal healable wearable device, sterilization (streptococcus mutan for decayed tooth), deicing, defogging, thermally preserving pipeline transportation of crude oil, energy-efficient window, seawater desalination, energy conversion and storage and solar thermal power. I would be a bit more selective in potential biomedical applications, which of these only needs small quantities and is higher value. For example, pipeline transportation and seawater desalination would involve huge quantities of nanoparticles, it is difficult to carry out at very low cost.

7. References

1. Roduner, E. Size matters: Why nanomaterials are different. *Chem. Soc. Rev.* **35**, 583–592 (2006).

2. Gour, A. & Jain, N. K. Advances in green synthesis of nanoparticles. *Artif. Cells, Nanomedicine Biotechnol.* **47**, 844–851 (2019).

3. Sandhu, R. S., Singh Sandhu, R., Aharwal, R. P. & Kumar, S. Green Synthesis: a Novel Approach for Nanoparticles Synthesis. *Artic. Int. J. Pharm. Sci. Res.* **10**, 3550–3562 (2019).

4. Ali, M. R. K., Wu, Y. & El-Sayed, M. A. Gold-Nanoparticle-Assisted Plasmonic Photothermal Therapy Advances Toward Clinical Application. *J. Phys. Chem. C* **123**, 15375–15393 (2019).

5. Huang, X. *et al.* Design and Functionalization of the NIR-Responsive Photothermal Semiconductor Nanomaterials for Cancer Theranostics. *Acc. Chem. Res.* **50**, 2529–2538 (2017).

6. Lee, C., Kim, H., Cho, Y. & Lee, W. I. The properties of porous silicon as a therapeutic agent via the new photodynamic therapy. *J. Mater. Chem.* **17**, 2648–2653 (2007).

7. Oleshchenko, V. A. *et al.* Localized infrared radiation-induced hyperthermia sensitized by laser-ablated silicon nanoparticles for phototherapy applications. *Appl. Surf. Sci.* **516**, 1–7 (2020).

8. Hong, C., Lee, J., Zheng, H., Hong, S. S. & Lee, C. Porous silicon nanoparticles for cancer photothermotherapy. *Nanoscale Res. Lett.* **6**, 321, 1–8 (2011).

9. Lee, C., Hong, C., Lee, J., Son, M. & Hong, S. S. Comparison of oxidized porous silicon with bare porous silicon as a photothermal agent for cancer cell destruction based on in vitro cell test results. *Lasers Med. Sci.* **27**, 1001–1008 (2012).

10. Lee, C. *et al.* Porous silicon as an agent for cancer thermotherapy based on near-infrared light irradiation. *J. Mater. Chem.* **18**, 4790–4795 (2008).

11. Hong, C. & Lee, C. In vitro cell tests of pancreatic malignant tumor cells by photothermotherapy based on DMSO porous silicon colloids. *Lasers Med. Sci.* **29**, 221–223 (2014).

12. Xu, W. *et al.* Scalable Synthesis of Biodegradable Black Mesoporous Silicon Nanoparticles for Highly Efficient Photothermal Therapy. *ACS Appl. Mater. Interfaces* **10**, 23529–23538 (2018).

13. Yu, X., Yang, K., Chen, X. & Li, W. Black hollow silicon oxide nanoparticles as highly efficient photothermal agents in the second near-infrared window for in vivo cancer therapy. *Biomaterials* **143**, 120–129 (2017).

14. Özbilgin, I. N. G., Ghosh, B., Yamada, H. & Shirahata, N. Size-dependent photothermal performance of silicon quantum dots. *J. Phys. Chem. C* **125**, 3421–3431 (2021).

15. Miao, Z. *et al.* Tiny 2D silicon quantum sheets: a brain photonic nanoagent for orthotopic glioma theranostics. *Sci. Bull.* **66**, 147–157 (2021).

16. Ma, L., Song, X., Yu, Y. & Chen, Y. Two-Dimensional Silicene/Silicon Nanosheets: An Emerging Silicon-Composed Nanostructure in Biomedicine. *Adv. Mater.* **33**, 1–16 (2021).

17. Canham, L. *Handbook of Porous Silicon*. (Springer Reference, 2014).

18. Chu, M. *et al.* Near-infrared laser light mediated cancer therapy by photothermal effect of Fe3O4 magnetic nanoparticles. *Biomaterials* **34**, 4078–4088 (2013).

19. Espinosa, A. *et al.* Duality of Iron Oxide Nanoparticles in Cancer Therapy: Amplification of Heating Efficiency by Magnetic Hyperthermia and Photothermal Bimodal Treatment. *ACS Nano* **10**, 2436–2446 (2016).

20. Shen, S. *et al.* Magnetic nanoparticle clusters for photothermal therapy with near-infrared irradiation. *Biomaterials* **39**, 67–74 (2015).

21. Estelrich, J. & Antònia Busquets, M. Iron oxide nanoparticles in photothermal therapy. *Molecules* **23**, 1–26 (2018).

22. Jin, Q. *et al.* Albumin-Assisted Synthesis of Ultrasmall FeS2 Nanodots for Imaging-Guided Photothermal Enhanced Photodynamic Therapy. *ACS Appl. Mater. Interfaces* **10**, 332–340 (2018).

23. Yang, K. *et al.* FeS nanoplates as a multifunctional nano-theranostic for magnetic resonance imaging guided photothermal therapy. *Biomaterials* **38**, 1–9 (2015).

24. Cao, Q. *et al.* Flower-like Fe7S8/Bi2S3 superstructures with improved near-infrared absorption for efficient chemo-photothermal therapy. *Dalt. Trans.* **48**, 3360–3368 (2019).

25. Tang, Z. *et al.* Antiferromagnetic Pyrite as the Tumor Microenvironment-Mediated Nanoplatform for Self-Enhanced Tumor Imaging and Therapy. *Adv. Mater.* **29**, 1–8 (2017).

26. Liu, J. *et al.* Fe3S4 nanoparticles for arterial inflammation therapy: Integration of magnetic hyperthermia and photothermal treatment. *Appl. Mater. Today* **18**, 1–13 (2020).

27. Wu, F. *et al.* Hollow Porous Carbon Coated FeS2-Based Nanocatalysts for Multimodal Imaging-Guided Photothermal, Starvation, and Triple-

Enhanced Chemodynamic Therapy of Cancer. *ACS Appl. Mater. Interfaces* **12**, 10142–10155 (2020).

28. Fu, T. *et al.* Nanoscale Facile preparation of uniform FeSe2 nanoparticles for PA/MR dual-modal imaging and photothermal. *Nanoscale* **7**, 20757–20768 (2015).

29. Yu, J. *et al.* Multistimuli-regulated photochemothermal cancer therapy remotely controlled via Fe5C2 nanoparticles. *ACS Nano* **10**, 159–169 (2016).

30. Zeng, J. F. *et al.* pH-Responsive Fe(III)-Gallic Acid Nanoparticles for In Vivo Photoacoustic-Imaging-Guided Photothermal Therapy. *Adv. Healthc. Mater.* **5**, 772–780 (2016).

31. Rouquerol. Impact of Science on Society. **157**, 5–15 (1990).

32. Getzlaff, M. *Fundamentals of Magnetism*. (Springer, 2007).

33. Mohammed, L., Gomaa, H. G., Ragab, D. & Zhu, J. Magnetic nanoparticles for environmental and biomedical applications: A review. *Particuology* **30**, 1–14 (2017).

34. Majetich, S. A., Wen, T. & Mefford, O. T. Magnetic nanoparticles. *MRS Bull.* **38**, 899–903 (2013).

35. Velasco, S. & Román, F. L. Determining the Curie Temperature of Iron and Nickel. *Phys. Teach.* **45**, 387–389 (2007).

36. Berg, J. *Wettability*. (CRC Press, 1993).

37. URL https://www.biolinchina.com/attension.

38. Liber-Kneć, A. & Łagan, S. Surface testing of dental biomaterials—determination of contact angle and surface free energy. *Materials (Basel).* **14**, 2716 (1–15) (2021).

39. Michel, J. C., Rivière, L. M. & Bellon-Fontaine, M. N. Measurement of the wettability of organic materials in relation to water content by the capillary rise method. *Eur. J. Soil Sci.* **52**, 459–467 (2001).

40. Alghunaim, A. & Zhang Newby, B. M. Influence of tube wettability on water contact angle of powders determined by capillary rise. *Colloids Surfaces A Physicochem. Eng. Asp.* **492**, 79–87 (2016).

41. Hutchison, S. G., Richardson, L. S. & Wai, C. M. Carbothermic Reduction of Silicon Dioxide. *Metall. Trans.* **19**, 249–253 (1988).

42. Filsinger, D. H. & Bourrie, D. B. Silica to Silicon: Key Carbothermic Reactions and Kinetics. *J. Am. Ceram. Soc.* **73**, 1726–1732 (1990).

43. Liu, X. *et al.* Scalable synthesis of si nanostructures by low-temperature magnesiothermic reduction of silica for application in lithium ion batteries. *Nano Energy* **4**, 31–38 (2014).

44. Li, X. *et al.* A stable nanoporous silicon anode prepared by modified magnesiothermic reactions. *Nano Energy* **20**, 68–75 (2015).

45. Jia, H. *et al.* High performance porous Si@C anodes synthesized by low temperature aluminothermic reaction. *Electrochim. Acta* **269**, 509–516 (2018).

46. Zhou, Z. W., Liu, Y. T., Xie, X. M. & Ye, X. Y. Aluminothermic reduction enabled synthesis of silicon hollow microspheres from commercialized silica nanoparticles for superior lithium storage. *Chem. Commun.* **52**, 8401–8404 (2016).

47. Yoo, J. K. *et al.* Extremely high yield conversion from low-cost sand to high-capacity Si electrodes for Li-ion batteries. *Adv. Energy Mater.* **4**, 1–9 (2014).

48. Li, H. *Principle of metallurgy.* (Science Press, 2018).

49. Lee, C., Kim, H. & In, W. The properties of porous silicon as a therapeutic agent via the new photodynamic therapy. *J. Mater. Chem.* **17**, 2648–2653 (2007).

50. Zhu, F., Ma, S., Liu, T. & Deng, X. Green synthesis of nano zero-valent iron/Cu by green tea to remove hexavalent chromium from groundwater. *J. Clean. Prod.* **174**, 184–190 (2018).

51. Fazlzadeh, M. *et al.* A novel green synthesis of zero valent iron nanoparticles (NZVI) using three plant extracts and their efficient application for removal of Cr(VI) from aqueous solutions. *Adv. Powder Technol.* **28**, 122–130 (2017).

52. Eslami, S., Ebrahimzadeh, M. A. & Biparva, P. Green synthesis of safe zero valent iron nanoparticles by: Myrtus communis leaf extract as an effective agent for reducing excessive iron in iron-overloaded mice, a thalassemia model. *RSC Adv.* **8**, 26144–26155 (2018).

53. Ebrahiminezhad, A., Zare-Hoseinabadi, A., Berenjian, A. & Ghasemi, Y. Green synthesis and characterization of zero-valent iron nanoparticles using stinging nettle (Urtica dioica) leaf extract. *Green Process. Synth.* **6**, 469–475 (2017).

54. Somchaidee, P. & Tedsree, K. Green synthesis of high dispersion and narrow size distribution of zero-valent iron nanoparticles using guava leaf (Psidium guajava L) extract. *Adv. Nat. Sci. Nanosci. Nanotechnol.* **9**, 1–9 (2018).

55. Bryce C, T., Stephen A, S. & Luther, E. P. Nanoporous metal foams. *Angew. Chemie - Int. Ed.* **49**, 4544–4565 (2010).

56. Chen, X. & Liang, C. Transition metal silicides: fundamentals, preparation and catalytic applications. *Catal. Sci. Technol.* **9**, 4785–4820 (2019).

57. Goldfarb, I., Cesura, F. & Dascalu, M. Magnetic Binary Silicide Nanostructures. *Adv. Mater.* **30**, 1–11 (2018).

58. Goldbeck, V. *IRON—Binary Phase Diagrams.* (Springer, 1982).

59. Okamoto, H. *Desk Handbook: Phase Diagram for Binary Alloys*. (ASM International, 2000).

60. Esfahani, S. & Barati, M. Purification of metallurgical silicon using iron as an impurity getter part I: Growth and separation of Si. *Met. Mater. Int.* **17**, 823–829 (2011).

61. Potudanskii, G. P., Peshkov, Y. A. & Kurganskii, S. I. Electronic structure and K-edge X-ray absorption of iron monosilicide. *J. Phys. Conf. Ser.* **1902**, 1–6 (2021).

62. L.F. Mattheiss. Band structure and semiconducting properties of FeSi. *Phys. Rev. B* **47**, 114–119 (1993).

63. Wang, X., He, Z., Xiong, S. & Wu, X. Synthesis of crystalline pyramidal ε-fesi and morphology- and size-dependent ferromagnetism. *J. Phys. Chem. C* **118**, 2222–2228 (2014).

64. Ouyang, L., Thrall, E. S., Deshmukh, M. M. & Park, H. Vapor-phase synthesis and characterization of ε-FeSi nanowires. *Adv. Mater.* **18**, 1437–1440 (2006).

65. Yu, H., Wen, Y. & Bi, X. Magnetic and mechanical properties of the gradient FeSi alloys fabricated by magnetron sputtering. *J. Alloys Compd.* **634**, 83–86 (2015).

66. Jianhua ma, Yunle Gu, Yitai Qian. *Chinese J. Inorg. Chem.* **20**, 1009–1012 (2004).

67. Yoo, J. K. *et al.* Extremely high yield conversion from low-cost sand to high-capacity Si electrodes for Li-ion batteries. *Adv. Energy Mater.* **4**, 1–9 (2014).

68. Li, X. *et al.* A stable nanoporous silicon anode prepared by modified magnesiothermic reactions. *Nano Energy* **20**, 68–75 (2015).

69. Cook, J. B. *et al.* Tuning Porosity and Surface Area in Mesoporous Silicon for Application in Li-Ion Battery Electrodes. *ACS Appl. Mater. Interfaces* **9**, 19063–19073 (2017).

70. Françoise Rouquerol, J. R. and K. S. *Adsorption by Powders and Porous Solids: Principles, Methodology and Applications*. (Elsevier Ltd, 1998).

71. Bu, Y. *et al.* Anisotropic Truncated Octahedral Au with Pt Deposition on Arris for Localized Surface Plasmon Resonance-Enhanced Photothermal and Photodynamic Therapy of Osteosarcoma. *ACS Appl. Mater. Interfaces* **13**, 35328–35341 (2021).

72. Jain, P. K., Huang, X., El-Sayed, I. H. & El-Sayed, M. A. Noble metals on the nanoscale: Optical and photothermal properties and some applications in imaging, sensing, biology, and medicine. *Acc. Chem. Res.* **41**, 1578–1586 (2008).

73. Moores, A. & Goettmann, F. The plasmon band in noble metal nanoparticles: An introduction to theory and applications. *New J. Chem.* **30**, 1121–1132 (2006).

74. Jia, G. Z. *et al.* Excellent photothermal conversion of core/shell CdSe/Bi2Se3 quantum dots. *Nano Res.* **8**, 1443–1453 (2015).

75. Zhang, X. *et al.* Molecular engineering of narrow bandgap porphyrin derivatives for highly efficient photothermal conversion. *Dye. Pigment.* **192**, 109460, 1–7 (2021).

76. He, W. *et al.* Structure development of carbon-based solar-driven water evaporation systems. *Sci. Bull.* **66**, 1472–1483 (2021).

77. Xu, D., Li, Z., Li, L. & Wang, J. Insights into the Photothermal Conversion of 2D MXene Nanomaterials: Synthesis, Mechanism, and Applications. *Adv. Funct. Mater.* **30**, 2000712, 1–21 (2020).

78. Buffat, P. Size effect on the melting temperature of gold particles. *Phys. Rev. A* **13**, 2287–2298 (1976).

79. Talyzin, I. V., Samsonov, M. V., Samsonov, V. M., Pushkar, M. Y. & Dronnikov, V. V. Size Dependence of the Melting Point of Silicon Nanoparticles: Molecular Dynamics and Thermodynamic Simulation. *Semiconductors* **53**, 947–953 (2019).

80. Chen, H. *et al.* Understanding the photothermal conversion efficiency of gold nanocrystals. *Small* **6**, 2272–2280 (2010).

81. Regli, S., Kelly, J. A., Shukaliak, A. M. & Veinot, J. G. C. Photothermal response of photoluminescent silicon nanocrystals. *J. Phys. Chem. Lett.* **3**, 1793–1797 (2012).

82. Roper, D. K., Ahn, W. & Hoepfner, M. Microscale heat transfer transduced by surface plasmon resonant gold nanoparticles. *J. Phys. Chem. C* **111**, 3636–3641 (2007).

83. Sun, Z. *et al.* Ultrasmall Black Phosphorus Quantum Dots: Synthesis and Use as Photothermal Agents. *Angew. Chemie - Int. Ed.* **54**, 11526–11530 (2015).

84. Li, S. *et al.* Graphdiyne Materials as Nanotransducer for in Vivo Photoacoustic Imaging and Photothermal Therapy of Tumor. *Chem. Mater.* **29**, 6087–6094 (2017).

85. Yang, K. *et al.* Graphene in mice: Ultrahigh in vivo tumor uptake and efficient photothermal therapy. *Nano Lett.* **10**, 3318–3323 (2010).

86. Lin, H., Wang, Y., Gao, S., Chen, Y. & Shi, J. Theranostic 2D Tantalum Carbide (MXene). *Adv. Mater.* **30**, 1–11 (2018).

87. Sun, C. *et al.* One-pot solventless preparation of PEGylated black phosphorus nanoparticles for photoacoustic imaging and photothermal therapy of cancer. *Biomaterials* **91**, 81–89 (2016).

88. Liu, J. *et al.* Bismuth sulfide nanorods as a precision nanomedicine for in vivo multimodal imaging-guided photothermal therapy of tumor. *ACS Nano* **9**, 696–707 (2015).

89. Sun, Z. *et al.* Ultrasmall Black Phosphorus Quantum Dots: Synthesis and Use as Photothermal Agents. *Angew.Chem.Int.Ed.* **54**, 11526–11530 (2015).

90. Huang, C. C. *et al.* New insight on optical and magnetic Fe3O4 nanoclusters promising for near infrared theranostic applications. *Nanoscale* **7**, 12689–12697 (2015).

91. Cooper, G. M. *The Cancer Book: A Guide to Understanding the Causes, Prevention, and Treatment of Cancer*. (Jones and Bartlett, 1993).

92. Song, C. W. Effect of local hyperthermia on blood flow and microenvironment: A review. *Cancer Res.* **44**, 4721–4730 (1984).

93. Das, R. *et al.* Boosted Hyperthermia Therapy by Combined AC Magnetic and Photothermal Exposures in Ag/Fe3O4 Nanoflowers. *ACS Appl. Mater. Interfaces* **8**, 25162–25169 (2016).

94. Mona, L. P., Songca, S. P. & Ajibade, P. A. Synthesis and encapsulation of iron oxide nanorods for application in magnetic hyperthermia and photothermal therapy. *Nanotechnol. Rev.* **11**, 176–190 (2021).

95. Shukla, N., Singh, B., Kim, H. J., Park, M. H. & Kim, K. Combinational Chemotherapy and Photothermal Therapy Using a Gold Nanorod Platform for Cancer Treatment. *Part. Part. Syst. Charact.* **37**, 1–15 (2020).

96. Duan, L., Liu, T. & Chen, T. Near-infrared laser-triggered drug release in a tellurium nanosystem for simultaneous chemo-photothermal cancer therapy. *Biomater. Sci.* **9**, 1767–1778 (2021).

97. Huang, X., Shi, Q., Du, S., Lu, Y. & Han, N. Poly-tannic acid coated paclitaxel nanocrystals for combinational photothermal-chemotherapy. *Colloids Surfaces B Biointerfaces* **197**, 111377, 1–8 (2021).

98. Guo, W. *et al.* VB12-Sericin-PBLG-IR780 Nanomicelles for Programming Cell Pyroptosis via Photothermal (PTT)/Photodynamic (PDT) Effect-Induced Mitochondrial DNA (mitoDNA) Oxidative Damage. *ACS Appl. Mater. Interfaces* **14**, 17008–17021 (2022).

99. Yeo, E. L. L. *et al.* Exploiting the protein corona around gold nanorods for low-dose combined photothermal and photodynamic therapy. *J. Mater. Chem. B* **5**, 254–268 (2017).

100. Peng, R. *et al.* Intramolecular Charge Transfer-Based Conjugated Oligomer with Fluorescence, Efficient Photodynamics, and Photothermal Activities. *ACS Appl. Bio Mater.* **4**, 6565–6574 (2021).

101. Wang, M. *et al.* Synergistic interventional photothermal therapy and immunotherapy using an iron oxide nanoplatform for the treatment of pancreatic cancer. *Acta Biomater.* **138**, 453–462 (2022).

102. Shang, T., Yu, X., Han, S. & Yang, B. Nanomedicine-based tumor photothermal therapy synergized immunotherapy. *Biomater. Sci.* **8**, 5241–5259 (2020).

103. Li, R. *et al.* A Dual Functional Drug Delivery System that Combines Photothermal Therapy and Immunotherapy to Treat Tumors. *Mol. Pharm.* **19**, 1449–1457 (2022).

104. Smith, A. M., Mancini, M. C. & Nie, S. Bioimaging: Second window for in vivo imaging. *Nat. Nanotechnol.* **4**, 710–711 (2009).

105. Friebel, M., Helfmann, J., Netz, U. & Meinke, M. Influence of oxygen saturation on the optical scattering properties of human red blood cells in the spectral range 250 to 2000 nm. *J. Biomed. Opt.* **14**, 1–6 (2009).

106. Chen, Z., Zhang, L., Sun, Y., Hu, J. & Wang, D. 980-Nm Laser-Driven Photovoltaic Cells Based on Rare-Earth Up-Converting Phosphors for Biomedical Applications. *Adv. Funct. Mater.* **19**, 3815–3820 (2009).

107. Lin, H., Wang, X., Yu, L., Chen, Y. & Shi, J. Two-Dimensional Ultrathin MXene Ceramic Nanosheets for Photothermal Conversion. *Nano Lett.* **17**, 384–391 (2017).

108. Wilhelm, S. *et al.* Analysis of nanoparticle delivery to tumours. *Nat. Rev. Mater.* **1**, 1–12 (2016).

109. Wang, X. *et al.* A Polydopamine Nanoparticle-Knotted Poly(ethylene glycol) Hydrogel for On-Demand Drug Delivery and Chemo-photothermal Therapy. *Chem. Mater.* **29**, 1370–1376 (2017).

110. Xie, G., Zhang, L., Pan, J., Zhang, X. & Sun, S. K. Green and Kilogram-Scale Synthesis of Fe Hydrogel for Photothermal Therapy of Tumors in Vivo. *ACS Biomater. Sci. Eng.* **6**, 4276–4284 (2020).

111. Liu, B. *et al.* Injectable In Situ Induced Robust Hydrogel for Photothermal Therapy and Bone Fracture Repair. *Adv. Funct. Mater.* **31**, 1–8 (2021).

112. URL https://zh.wikibooks.org/wiki/%E5%85%83%E7%B4%A0%E5%91%A8%E6%9C%9F%E8%A1%A8.

113. Ali, M. R. K., Wu, Y. & El-Sayed, M. A. Gold-Nanoparticle-Assisted Plasmonic Photothermal Therapy Advances Toward Clinical Application. *J. Phys. Chem. C* **123**, 15375–15393 (2019).

114. Wu, H. *et al.* Fe3O4-Based Multifunctional Nanospheres for Amplified Magnetic Targeting Photothermal Therapy and Fenton Reaction. *ACS Biomater. Sci. Eng.* **5**, 1045–1056 (2019).

115. Zhou, Z. *et al.* Iron/iron oxide core/shell nanoparticles for magnetic targeting MRI and near-infrared photothermal therapy. *Biomaterials* **35**, 7470–7478 (2014).

116. Yang, Y. *et al.* Fe3O4@MnO2@PPy nanocomposites overcome hypoxia: Magnetic-targeting-assisted controlled chemotherapy and enhanced photodynamic/photothermal therapy. *J. Mater. Chem. B* **6**, 6848–6857 (2018).

117. Dong, W. *et al.* Facile synthesis of monodisperse superparamagnetic Fe3O4 Core@hybrid@Au shell nanocomposite for bimodal imaging and photothermal therapy. *Adv. Mater.* **23**, 5392–5397 (2011).

118. Li, J. *et al.* Hyaluronic acid-modified Fe3O4 at Au core/shell nanostars for multimodal imaging and photothermal therapy of tumors. *Biomaterials* **38**, 10–21 (2015).

119. Ju, Y. *et al.* Monodisperse Au-Fe2C Janus Nanoparticles: An Attractive Multifunctional Material for Triple-Modal Imaging-Guided Tumor Photothermal Therapy. *ACS Nano* **11**, 9239–9248 (2017).

120. Zheng, T. *et al.* Gold-nanosponge-based multistimuli-responsive drug vehicles for targeted chemo-photothermal therapy. *Adv. Mater.* **28**, 8218–8226 (2016).

121. You J., Zhang G., L. C. Exceptionally High Payload of. *ACS Nano* **4**, 1033–1041 (2010).

122. Melancon, M. P., Zhou, M. & Li, C. Cancer theranostics with near-infrared light-activatable multimodal nanoparticles. *Acc. Chem. Res.* **44**, 947–956 (2011).

123. An, K. & Hyeon, T. Synthesis and biomedical applications of hollow nanostructures. *Nano Today* **4**, 359–373 (2009).

124. Chen, J. *et al.* Gold nanocages as photothermal transducers for cancer treatment. *Small* **6**, 811–817 (2010).

125. Yavuz, M. S. *et al.* Gold nanocages covered by smart polymers for controlled release with near-infrared light. *Nat. Mater.* **8**, 935–939 (2009).

126. Chen, J. *et al.* Immuno gold nanocages with tailored optical properties for targeted photothermal destruction of cancer cells. *Nano Lett.* **7**, 1318–1322 (2007).

127. Xia, X., Zhang, Q., Yang, M. & Cho, E. U. N. C. Gold Nanocages: From Synthesis to Theranostic Applications. *Acc. Chem. Res.* **44**, 914–924 (2011).

128. Alhmoud, H., Cifuentes-Rius, A., Delalat, B., Lancaster, D. G. & Voelcker, N. H. Gold-decorated porous silicon nanopillars for targeted hyperthermal treatment of bacterial infections. *ACS Appl. Mater. Interfaces* **9**, 33707–33716 (2017).

129. Shao, J. *et al.* Biodegradable black phosphorus-based nanospheres for in vivo photothermal cancer therapy. *Nat. Commun.* **7**, 1–13 (2016).

130. Yin, W. *et al.* High-throughput synthesis of single-layer MoS2 nanosheets as a near-infrared photothermal-triggered drug delivery for effective cancer therapy. *ACS Nano* **8**, 6922–6933 (2014).

131. Lin, H., Gao, S., Dai, C., Chen, Y. & Shi, J. A Two-Dimensional Biodegradable Niobium Carbide (MXene) for Photothermal Tumor

Eradication in NIR-I and NIR-II Biowindows. *J. Am. Chem. Soc.* **139**, 16235–16247 (2017).

132. Sun, T. *et al.* Second Near-Infrared Conjugated Polymer Nanoparticles for Photoacoustic Imaging and Photothermal Therapy. *ACS Appl. Mater. Interfaces* **10**, 7919–7926 (2018).

133. Lin, H., Chen, Y. & Shi, J. Insights into 2D MXenes for Versatile Biomedical Applications: Current Advances and Challenges Ahead. *Adv. Sci.* **5**, 1–20 (2018).

134. Rastinehad, A. R. *et al.* Gold nanoshell-localized photothermal ablation of prostate tumors in a clinical pilot device study. *Proc. Natl. Acad. Sci. U. S. A.* **116**, 18590–18596 (2019).

135. Hirsch, L. R. *et al.* Nanoshell-mediated near-infrared thermal therapy of tumors under magnetic resonance guidance. *Proc. Natl. Acad. Sci. U. S. A.* **100**, 13549–13554 (2003).

136. Williams, D. F. On the mechanisms of biocompatibility. *Biomaterials* **29**, 2941–2953 (2008).

137. Hench, L. L., Splinter, R. J., Allen, W. C. & Greenlee, T. K. Bonding mechanisms at the interface of ceramic prosthetic materials. *J. Biomed. Mater. Res.* **5**, 117–141 (1971).

138. Hendra Hermawan. *Biodegradable Metals From Concept to Applications*. (Springer, 2012).

139. Chiellini, E. Biodegradable Polymers and Plastics. *Chem. Int. -- Newsmag. IUPAC* **26**, (2014).

140. Anderson, S. H. C., Elliott, H., Wallis, D. J., Canham, L. T. & Powell, J. J. Dissolution of different forms of partially porous silicon wafers under simulated physiological conditions. *Phys. Status Solidi Appl. Res.* **197**, 331–335 (2003).

141. Godin, B. *et al.* Tailoring the degradation kinetics of mesoporous silicon structures through PEGylation. *J. Biomed. Mater. Res. - Part A* **94**, 1236–1243 (2010).

142. Xu, W. *et al.* Scalable Synthesis of Biodegradable Black Mesoporous Silicon Nanoparticles for Highly Efficient Photothermal Therapy. *ACS Appl. Mater. Interfaces* **10**, 23529–23538 (2018).

143. Zhen, Z., Xi, T. F. & Zheng, Y. F. A review on in vitro corrosion performance test of biodegradable metallic materials. *Trans. Nonferrous Met. Soc. China* **23**, 2283–2293 (2013).

144. Moravej, M., Purnama, A., Fiset, M., Couet, J. & Mantovani, D. Electroformed pure iron as a new biomaterial for degradable stents: In

vitro degradation and preliminary cell viability studies. *Acta Biomater.* **6**, 1843–1851 (2010).

145. Zhu, H. *et al.* Sulfur Defect-Engineered Biodegradable Cobalt Sulfide Quantum Dot-Driven Photothermal and Chemodynamic Anticancer Therapy. *ACS Appl. Mater. Interfaces* **14**, 25183–25196 (2022).

146. Wang, J. *et al.* Biodegradable Ferrous Sulfide-Based Nanocomposites for Tumor Theranostics through Specific Intratumoral Acidosis-Induced Metabolic Symbiosis Disruption. *J. Am. Chem. Soc.* **144**, 19884–19895 (2022).

147. Ortiz De Solorzano, I. *et al.* Microfluidic Synthesis and Biological Evaluation of Photothermal Biodegradable Copper Sulfide Nanoparticles. *ACS Appl. Mater. Interfaces* **8**, 21545–21554 (2016).

148. Chen, H. *et al.* Highly crystallized iron oxide nanoparticles as effective and biodegradable mediators for photothermal cancer therapy. *J. Mater. Chem. B* **2**, 757–765 (2014).

149. Cheng, Y., Lu, H., Yang, F., Zhang, Y. & Dong, H. Biodegradable FeWO: Xnanoparticles for CT/MR imaging-guided synergistic photothermal, photodynamic, and chemodynamic therapy. *Nanoscale* **13**, 3049–3060 (2021).

150. Yin, W. *et al.* Biodegradable MoOx nanoparticles with efficient near-infrared photothermal and photodynamic synergetic cancer therapy at the second biological window. *Nanoscale* **10**, 1517–1531 (2018).

151. Shao, J., Zhang, J., Jiang, C., Lin, J. & Huang, P. Biodegradable titanium nitride MXene quantum dots for cancer phototheranostics in NIR-I/II biowindows. *Chem. Eng. J.* **400**, 1–12 (2020).

152. Tao, N. *et al.* Minimally Invasive Antitumor Therapy Using Biodegradable Nanocomposite Micellar Hydrogel with Functionalities of NIR-II Photothermal Ablation and Vascular Disruption. *ACS Appl. Bio Mater.* **3**, 4531–4542 (2020).

153. Park, J. H. *et al.* Biodegradable luminescent porous silicon nanoparticles for in vivo applications. *Nat. Mater.* **8**, 331–336 (2009).

154. Xu, X. *et al.* Biodegradable Black-Phosphorus-Nanosheet-Based Nanoagent for Enhanced Chemo-Photothermal Therapy. *Part. Part. Syst. Charact.* **37**, 1–6 (2020).

155. Xie, H. *et al.* Biodegradable near-infrared-photoresponsive shape memory implants based on black phosphorus nanofillers. *Biomaterials* **164**, 11–21 (2018).

156. Shao, J. *et al.* Author Correction: Biodegradable black phosphorus-based nanospheres for in vivo photothermal cancer therapy (Nature

Communications, (2016), 7, 1, (12967), 10.1038/ncomms12967). *Nat. Commun.* **12**, 20–22 (2021).

157. Rodhe, Y., Skoglund, S., Odnevall Wallinder, I., Potácová, Z. & Möller, L. Copper-based nanoparticles induce high toxicity in leukemic HL60 cells. *Toxicol. Vitr.* **29**, 1711–1719 (2015).

158. Li, T. *et al.* Energy metabolism and metabolomics response of Pacific white shrimp Litopenaeus vannamei to sulfide toxicity. *Aquat. Toxicol.* **183**, 28–37 (2017).

159. Chikara Ohtsuki, T. K. Mechanism of apatite formation on CaO-SiO2-P2O5 glasses in a simulated body fluid. *J. Non. Cryst. Solids* **143**, 84–92 (1992).

160. URL https://en.wikipedia.org/wiki/Simulated_body_fluid.

161. Bigi, A. *et al.* Nanocrystalline hydroxyapatite coatings on titanium: A new fast biomimetic method. *Biomaterials* **26**, 4085–4089 (2005).

162. Kokubo, T. & Takadama, H. How useful is SBF in predicting in vivo bone bioactivity? *Biomaterials* **27**, 2907–2915 (2006).

163. Oyane, A. *et al.* Formation and growth of clusters in conventional and new kinds of simulated body fluids. *J. Biomed. Mater. Res. - Part A* **64**, 339–348 (2003).